Mestrado Integrado em Engenharia Química

Development of Nanomaterials using the NETmix® Technology: Application to Production of MOFs

Tese de Mestrado

desenvolvida no âmbito da unidade curricular de

Dissertação

Marcelo Filipe dos Santos Costa

LSRE-FEUP

U.PORTO
FEUP FACULDADE DE ENGENHARIA UNIVERSIDADE DO PORTO

LABORATÓRIO ASSOCIADO
LSRE LABORATORY OF SEPARATION AND REACTION ENGINEERING
Laboratório Associado em Materiais icm

Departamento de Engenharia Química

Orientadores na FEUP: **Prof. José Carlos Lopes**

Profª. Madalena Dias

Julho de 2012

“Simplicity is the ultimate sophistication.”

Leonardo Da Vinci

Agradecimentos

Em primeiro lugar, gostaria de agradecer a todas as pessoas que me foram acompanhando, não só na realização da dissertação de Mestrado, mas ao longo de todo o curso e de toda a vida.

Gostaria de agradecer particularmente a algumas pessoas, que quer pelo seu apoio incondicional, quer pela sua paciência, me ajudaram e contribuíram de forma muito positiva para a minha evolução.

Em especial, gostaria de agradecer aos meus orientadores, o Professor José Carlos Lopes e a Professora Madalena Dias, pelas condições dadas para o desenvolvimento da tese, num tema tão atual e importante. Agradecer também por todo o apoio e disponibilidade demonstrada ao longo das semanas de trabalho.

Gostaria também de agradecer ao Eng. Carlos Fonte, pela incansável paciência e apoio que me deu durante o desenvolvimento do trabalho.

Ao Professor Joaquim Faria, gostaria de agradecer pela ajuda na caracterização físico-química do material.

Gostaria de agradecer a toda a equipa com quem trabalhei, pela boa disposição e bom ambiente. Em especial, ao Eng. Mumin Leblebici, colega no laboratório E404B e aos Engs. Cláudio Fonte e Marina Torres pela ajuda nas experiências de reologia.

Ao Eng. Luís Carlos pela realização dos ensaios de densidade e à Engª. Liliana Pereira pelo auxílio na realização dos ensaios de absorção atómica.

Ao Institut Lavoisier, em especial à Doutora Patricia Horcajada e Doutor Thomas Devic pelo pronto esclarecimento das dúvidas que foram surgindo ao longo do trabalho.

Para finalizar, gostaria de agradecer aos meus colegas de curso, que durante 5 anos tiveram que lidar com o meu mau feitio e embirrações. Agradecer também a todos os meus amigos, que foram muito importantes nesta caminhada que agora termina.

Não podia deixar de agradecer a toda a minha família, em especial aos meus pais e ao meu irmão, muito do que alcancei deve-se a eles.

Declaração

Declaro, sob compromisso de honra, que este trabalho é original e que todas as contribuições não originais foram devidamente referenciadas com identificação da fonte.

Marcelo Filipe dos Santos Costa

Julho de 2012

Abstract

The production of nanoparticles, particularly MOFs, has been widely studied for several applications in several areas. The production of MOFs is not trivial. Several factors need to be taken into account and many parameters need to be controlled in order to obtain a material that can be used in a certain application.

In the present work, NETmix® capabilities were tested for the production of MIL-88A, a metal-organic framework built up from iron (III) trimers linked to fumarate ligands, creating a 3-dimensional flexible network. The influence of concentration, temperature, addition of a dispersant and the maturation step on the particle size and shape were studied.

It was observed that the maturation step is important when production occurs at room-temperature, due to the formation of a possible metastable phase. When the experiment is performed at 80 ºC, although the final phase is immediately observed, the particles are larger. Significant differences between NETmix® and batch productions were not verified, except when operated at higher temperatures. NETmix® has shown capacity to produce MOFs under continuous flow production.

The material phase transition is a phenomenon that needs to be well understood in future works.

Keyword: Nanoparticle, Metal-organic framework, crystallization, particles growth, NETmix®

Resumo

A produção de nanopartículas, nomeadamente os MOFs, tem sido amplamente estudada para uso em várias aplicações em diferentes áreas. A produção de MOFs não se trata de um processo simples. São vários os fatores que têm de ser tidos em consideração e são muitos os parâmetros que necessitam de ser controlados de forma a se obter um material que possa ser usado numa determinada aplicação.

No presente trabalho, as capacidades da tecnologia NETmix® foram testadas para a produção do MIL-88A, um MOF criado através de trímeros de ferro (III) ligados a cadeias de fumarato, que formam uma rede tridimensional e flexível. A influência da concentração, temperatura, adição de um dispersante e a etapa de maturação no tamanho e forma das partículas foi estudada.

Observou-se que a maturação é particularmente importante quando a produção ocorre à temperatura ambiente, devido à inicial formação de uma possível fase metastável. Quando as experiências são realizadas a 80 ºC, apesar de se obter imediatamente a fase desejada, observa-se que as partículas são maiores. Não foram verificadas diferenças significativas entre as produções com o NETmix® e batch, exceto quando operados a temperaturas mais elevadas. O NETmix® mostrou-se capaz de produzir MOFs em modo contínuo.

A transição de fase do material deve ser alvo de maior estudo em futuros trabalhos.

Table of contents

1 Introduction 1

1.1 Motivation and Relevance 2

1.2 Thesis Objectives and Layout 2

2 State of the Art 4

2.1 Introduction 4

2.1.1 Synthesis routes 5

2.2 Potential Applications of MOFs 9

2.2.1 Hydrogen and methane storage 9

2.2.2 Gas adsorption selectivity 10

2.2.3 Catalysis in MOFs 11

2.2.4 Drug storage and delivery 11

2.2.5 Other applications 12

2.3 MIL-88A 12

2.4 NETmix® Reactor 17

3 Technical Description 20

3.1 Experimental Set-up 20

3.2 Characterization 23

3.2.1 Rheological experiments 23

3.2.2 Scanning Electron Microscopy (SEM) and Energy Dispersive Spectroscopy (EDS) 25

3.2.3 Dynamic Light Scattering (DLS) 26

3.2.4 Electrophoresis (Laser Doppler Velocimetry) 26

3.2.5 Atomic Absorption spectroscopy 27

3.2.6 X-Ray Diffraction (XRD) 27

3.2.7 Differential Scanning Calorimetry (DSC) and Thermogravimetric (TG) analysis 27

3.2.8 Nitrogen Adsorption 28

3.2.9 Helium Picnometer Method and Mercury Porosimetry 28

4 Results and Discussion 29

4.1 Zeta potential 30

4.2 Iron (III) conversion 32
4.3 Particles size distributions 34
4.4 SEM and EDS analysis 36
4.5 XRD Results 40
4.6 Specific surface area 41
4.7 Thermal analysis 42
4.8 Density 43
5 Final Remarks 45
5.1 Conclusions 45
5.2 Future Work 45
5.3 Global Appreciation 46
References 47
Appendix A Rheology experiments' results 49
Appendix B SEM images 53
Appendix C Shear rate and geometrical dimensions of the NETmix® reactor 66
Appendix D Nanoparticles mean free path 68
Appendix E Amount of dispersant 71

Notation

a	diagonal length (see Appendix D)	m
A	NETmix® channels cross section area	m^2
C	concentration	mol/L (M)
d	NETmix® channels depth	m
D	NETmix® chambers diameter	m
D_H	hydraulic diameter	m
D_{disp}	dispersant molecule diameter	m
I	edge length (see Appendix D)	m
j	diagonal length (see Appendix D)	m
L	particles length	m
m	mass	g
M	molecular weight	g/mol
n	number of moles	mol
N	number	
N_A	Avogadro number	mol^{-1}
Q	volumetric flowrate	m^3/s
Re	Reynolds number	
RI	refractive index	
S_{BET}	specific surface area by BET method	m^2/g
T	temperature	ºC
V	volume	m^3
W	particles width	m
X	chemical conversion	
y	direction's position	m

Greek letters

Δx	distance between two nanoparticles	m
$\dot{\gamma}$	shear rate	s^{-1}
ε_r	Dielectric constant	
ε_{exp}	experimental porosity	
$\varepsilon_{\text{theor}}$	theoretical porosity	
ζ_{mean}	mean zeta potential	mV
θ	diffraction angle	º
μ	viscosity	Pa·s or cP
υ	velocity	m/s
ρ	density	kg/m^3
ω	NETmix® channels width	m

Indexes

0	initial
ap	apparent
disp	dispersant
Fe	iron
max	maximum
min	minimum
np	nanoparticles
reac	reactants

sol	solution
t	time instant
x	direction

List of Acronyms

BASF	Badische Anilin und Soda Fabrik
bdt	1,4-benzeneditetrazolate
BET	Brunauer-Emmett-Teller
BTC	1,3,5-benzenetricarboxylate
CEMUP	Centro de Materiais da Universidade do Porto
DLS	Dynamic light scattering
DMF	N,N'-dimethylformamide
DSC	Differential scanning calorimetry
EDS	Energy-dispersive X-ray spectroscopy
HKUST	Hong Kong University of Science and Technology
IBU	Ibuprofen
INA	Isonicotinate
IRMOF	Isoreticular metal-organic framework
ITQMOF	Instituto de Tecnologia Quimica metal-organic framework
LCM	Laboratório de Catálise e Materiais
LDV	Laser doppler velocimetry
MIL	Matériaux de l'Institut Lavoisier
MOF	Metal-organic framework
MRI	Magnetic resonance imaging
PCN	Porous coordination network
PVP	Polyvinylpyrrolidone
SBU	Secondary building unit
SEM	Scanning electron microscopy
TG	Thermogravimetry
XRD	X-ray diffraction
ZIF	Zeolitic imidazolate framework

List of Tables

Table 1. Cell parameters of the MIL-88 type structures [28]. *13*

Table 2. Series of experiments. *23*

Table 3. Initial pH values and mean zeta potential for different dilution factors. *31*

Table 4. BET surface area of sample N01. ..... *42*

Table 5. Densities and porosities of MIL-88A. *43*

Table C-1. Geometrical dimensions of the NETmix® reactor (see Figure 15b). *66*

List of Figures

Figure 1. General building scheme for MOFs [8]. 2

Figure 2. A tentative hierarchy of coordination polymers and metal-organic frameworks; adapted [17]. 4

Figure 3. Overview of synthesis methods, possible reaction temperatures and final products [7]. 5

Figure 4. Scheme of the Ostwald ripening process. 6

Figure 5. Catenation example of MOF PCN-6: (a) – Catenated PCN-6; (b) Non-catenated PCN-6 [23]... 10

Figure 6. Hydrogen, oxygen, nitrogen and carbon monoxide adsorption isotherms of PCN-13 at 77 K [25]. 11

Figure 7. Ibuprofen delivery ((a): % IBU; (b): mg IBU/g dehydrated material versus time for MIL-100 and MIL-101 [5]. 12

Figure 8. Trimer of MIL-88. Yellow: iron atoms; Red: oxygen atoms; black: carbon atoms [8]. 13

Figure 9 – Structures of the MIL-88 based topology: (a) MIL-88A (experimental); (b) MIL-88B (simulation); (c) MIL-88C (simulation); (d) MIL-88D (simulation). Left: along the a axis; Right: along the c axis [28]. 13

Figure 10. Molecular structure of MIL-88A trimer (each iron is bonded to the oxygen atom of water). Green: iron atoms; Red: oxygen atoms; black: carbon atoms. 14

Figure 11. Experimental X-ray powder diffraction of MIL-88A, dried (423 K) as-synthesized (no post-treatment) or wetted with various solvents [30]. 15

Figure 12. Simulated crystal structures of MIL-88A in its dry (left), as-synthesized (no post-treatment - center) and open (right) forms [31]. 15

Figure 13. Particle size (curves) and yield (bars) as a function of time using different solvents [18]. . 16

Figure 14. TEM images obtained from hydrothermal microwave synthesis of MIL-88A at various temperatures and synthesis times [18]. 16

Figure 15. (a) Schematic representation of a network of chambers and channels; (b) 2D unit cell; (c) 3D unit cell [12]. 17

Figure 16. NETmix® prototypes: (a) NETmix® 3D; (b) Lab-Scale NETmix® 2D; (c) Multi-Inlet NETmix® 2D. 18

Figure 17. Tracer experiments at Re=150 [12]. 18

Figure 18. Pre-mixed injection scheme [12]. 20

Figure 19. NETmix® reactor experimental apparatus. Legend: 1-NETmix® Reactor; 2-Feeding pumps; 3-Reactants vessels; 4-Final product flask. 21

Figure 20. Batch experimental apparatus. Legend: 1-Batch reaction vessel; 2-Peristaltic pump; 3-Reactants vessel. 21

Figure 21. Schematic of the rheological experiments procedure. 24

Figure 22. Maximum viscosity of the reaction mixture as a function of the shear rate at 25 °C. 25

Figure 23. Electrical layers of the surface particles [34]. 27

Figure 24. pH variation with time in the ageing stage. 30

Figure 25. Zeta potential measurements: mean zeta potential as a function of pH. Isoelectric point is the point where the zeta potential is zero. 31

Figure 26. Zeta potential distributions for different pHs. 32

Figure 27. Iron conversion as a function of time, during the ageing stage. 33

Figure 28. Particle size distribution of sample N01 after 72 hours of maturation. 34

Figure 29. Particles size distribution of samples B02 (after 72 hours of maturation), N02 (after 72 hours of maturation) and N02 (dried, no maturation). 35

Figure 30. Particle size distribution of sample N03 after 72 hours of maturation. 35

Figure 31. Particle size distribution of samples B04 and N04, both after 72 hours of maturation. 36

Figure 32. SEM image of sample N01 (72 hours). 36

Figure 33. SEM images of samples N02 and B02: (a) N02 (0 hours); (b) N02 (72 hours); (c) B02 (0 hours); (d) B02 (72 hours). 37

Figure 34. SEM images of sample N03: (a) 0 hours; (b) 72 hours. 38

Figure 35. SEM images of samples: (a) N04 (0 hours); (b) B04 (0 hours). 38

Figure 36. SEM image of sample B05 (72 hours). 39

Figure 37. SEM images of non-mature samples after several days: (a) N02; (b) B02; (c) N03. 39

Figure 38. Sample N03 (after 72 hours of maturation) with indication of the tested region. 40

Figure 39. EDS spectrum for the region presented in Figure 38. 40

Figure 40. X-Ray diffraction spectra for N02, B02 and B05 samples. 41

Figure 41. Adsorption and desorption isotherms of nitrogen for different degassing conditions: (a)) 150 ºC for 3 hours; (b) 100 ºC for 5 hours; (c) 100 ºC for 20 hours. 41

Figure 42. DSC and TG results of sample N01. 43

Figure A-1. Reaction mixture viscosity as a function of time for different shear rates (for reactants concentration = 0.4 M). 49

Figure A-2. Reaction mixture viscosity as a function of time for different shear rates (for reactants concentration = 0.16 M). 50

Figure A-3. Reaction mixture viscosity as a function of time for different shear rates (for reactants concentration = 0.08 M). *50*

Figure A-4. Maximum viscosity as a function of: (a) reactants concentration; (b) shear rate. *51*

Figure A-5. Influence of the dispersant in the viscosity increase (shear rate = 356.5 s^{-1}). *52*

Figure B-1. SEM images of sample N01, at different scales. *53*

Figure B-2. SEM images of sample N02, no maturation, at different scales. *54*

Figure B-3. SEM images of sample N02, no maturation, after several days, at different scales. *55*

Figure B-4. SEM images of sample N02, after 72 hours of maturation, at different scales. *56*

Figure B-5. SEM images of sample B02, no maturation, at different scales. *57*

Figure B-6. SEM images of sample B02, no maturation, after several days, at different scales. *58*

Figure B-7. SEM images of sample B02, after 72 hours of maturation, at different scales. *59*

Figure B-8. SEM images of sample N03, no maturation, at different scales. *60*

Figure B-9. SEM images of sample N03, no maturation, after several days, at different scales. *61*

Figure B-10. SEM images of sample N03, after 72 hours of maturation, at different scales. *62*

Figure B-11. SEM images of sample N04, no maturation, at different scales. *63*

Figure B-12. SEM images of sample B04, no maturation, at different scales. *64*

Figure B-13. SEM images of sample B05, no maturation, at different scales. *65*

Figure C-1. Parabolic velocity profile in a NETmix® channel. *66*

Figure D-1. Nanoparticles geometry. *68*

Figure D-2. Volume of the solution with nanoparticles. *69*

Figure E-1. Number of dispersant molecules adsorbed (monolayer) in a nanoparticle. *71*

1 Introduction

Recently nanosized particles have gained attention from materials specialists due to their unique properties, which can be applied in the development of novel products to be used in numerous applications. Metal-organic frameworks are a good example of the growing interest in this type of materials.

Metal-organic frameworks, MOFs, are crystalline coordination networks consisting of metal ions or clusters linked by organic ligands to form porous or non-porous structures (Figure 1), depending on whether the networks allow access of guest molecules or not. The choice of the metal and the linker has significant effect on the final structure of the MOF, size and shape of the pores.

Since their discovery in 1989 [1], Metal-organic framework materials have attracted extensive attention due to their potential in a wide range of applications. MOFs have shown promising potential for gas adsorption and separation, hydrogen and carbon dioxide storage and catalysis [2, 3]. There are some promising results in biological imaging, luminescence sensing and drug delivery [4, 5].

Traditionally, the porous materials that have been used are either organic (e.g. activated carbon) or inorganic (e.g. zeolites). Organic materials are disordered structures. Inorganic materials require an organic or inorganic template (with strong interactions with the inorganic framework) for its synthesis, which can lead to a collapse of the material. The combination of both organic and inorganic structures in metal-organic frameworks results in stable and ordered materials, with high surface areas [6].

MOFs are usually synthesized by combining organic ligands and metal salts in solvothermal (or hydrothermal, depending whether the solvent is water or not) reactions, where the reactants are mixed in an autoclave, at temperatures up to 300 ºC [7]. The reactants are usually mixed in polar solvents such as water, ethanol, dialkylformamides, dimethyl sulfoxide or acetonitrile. The solvents not only dissolve reactants but also play a role as structure directing agents, which influence the properties of the final MOF. Alternative routes for MOFs synthesis have been developed and described in literature, including the mixture of non-miscible solvents, electrochemical route, and microwave irradiation [7].

The number of possible combinations between the metal ions and the organic ligands is extremely high, leading to a wide variety of different materials with different applications (many of them still unknown), so it is an ungrateful task any attempt to quantify them.

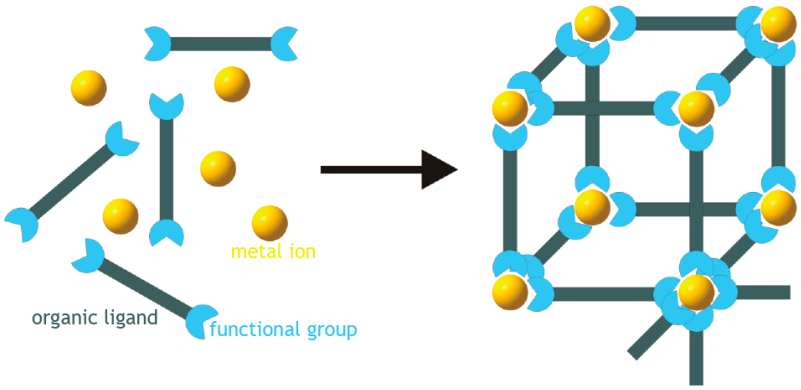

Figure 1. General building scheme for MOFs [8].

1.1 Motivation and Relevance

The production of high-value nanoparticles, such as metal-organic frameworks materials has gained particular interest over the last 2 decades, due to the possibility of obtaining a large variety of structures of interest for several fields related to porous materials.

In this work, the NETmix® static reactor has been tested to produce the metal-organic framework MIL-88A (designed by the Institut Lavoisier Versailles, Paris). MIL-88A exhibits a 3-D structure built up from trimers of iron (III) octahedral linked by fumarate chains [9].

The NETmix® reactor is a static mixer [10] that has a high degree of macro and micromixing quality control along the reactor. It is a new technology consisting of a regular network of cylindrical chambers (well mixed zones) and rectangular cross-section channels (segregation zones) [11-13]. This reactor has been successfully used to produce high purity, single-phase, nanocrystalline hydroxyapatite, with the stoichiometric amount of Ca/P ratio (important for its applications)[14, 15].

Mixing is one of the more important steps in the chemical industry. In many cases, deficient mixing conditions lead to deficient products. In nanomaterials, such as MIL-88A, the particle size is strongly dependent of the mixing conditions [16]. Therefore, it is essential to achieve good mixing (both macro and micromixing) to smooth out supersaturation peaks in local regions [16].

The motivation of this work is to revolutionize the metal-organic frameworks synthesis techniques, using lower temperatures, achieving higher productivities and a better control of its physical properties, using the NETmix® reactor.

1.2 Thesis Objectives and Layout

The main objective of this work is to study the properties of the metal-organic framework MIL-88A, synthesized using the NETmix® reactor at room temperature.

The layout of this work is as follows.

As a result of bibliographic research, Chapter 2 contains the state-of-the-art on metal-organic frameworks, particularly MIL-88A. In this chapter, some theoretical concepts about the physical process of crystallization are reviewed. Some important issues about MIL-88A are introduced, such as its main applications, synthesis routes used in previous works and its particular properties. Moreover, the NETmix® technology is introduced and its advantages are analyzed.

The technical description of the experiments will be presented in Chapter 3, such as the experimental set-up and description of the techniques used for particle characterization.

The obtained results are presented and discussed in Chapter 4, along with some of the technical difficulties faced along the project.

The mains conclusions of this work are presented in Chapter 5. Also, a full evaluation of the project, including future improvement suggestions, is given.

2 State of the Art

2.1 Introduction

Metal-organic frameworks, MOFs, are among the research areas of most interest in organic chemistry and materials engineering. MOFs are crystalline materials constituted by metallic ions connected by organic chains, called linkers (or ligands). Yet, it is extremely complicated to completely define what is and what is not a metal-organic framework [17]. Particularly, the nomenclature of these materials is still under question due to the difficulty of two different sciences (chemistry and material science) being able to produce the same kind of materials, but yet refer to them by different names. For example, coordination polymers and metal-organic frameworks are different names for the same type of materials (see Figure 2). Another question is what is a metal-organic framework? A porous material? Or simply a 3-dimensional structure made from metallic salts? In a recent classification [17] the following definition has been proposed: *a metal-organic framework is any system that forms a 2D or 3D network with carbon containing ligands bridging mononuclear, polynuclear or 1D coordination entities*.

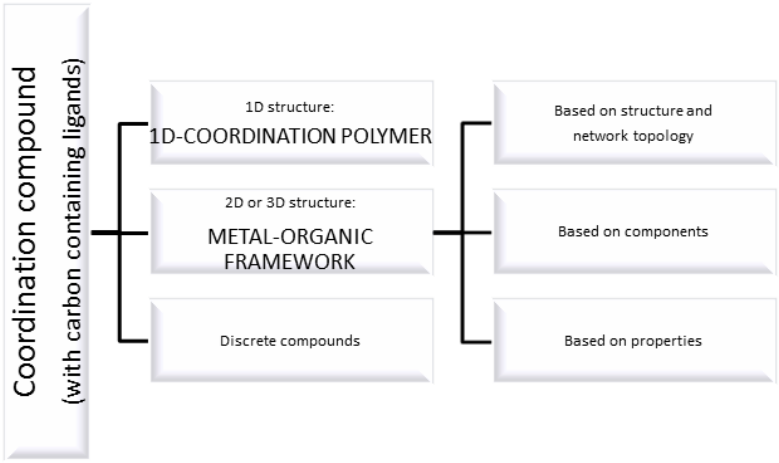

Figure 2. A tentative hierarchy of coordination polymers and metal-organic frameworks; adapted [17].

Thus, the concept of metal-organic framework will be used, in this work, because it is the most widely used nomenclature for these materials.

The synthesis of MOFs has attracted immense attention in the last couple of decades, because the combination of compounds and the number of different structures is almost infinite. Those structures have shown great potential for applications in a number of fields related to porous materials, including storage, separation and catalysis [3].

Although the number of possible structures is extremely large, the specialists give their attention to a small fraction of MOFs. To speed up the discovery of MOFs, high-throughput methods have been developed.

There are a huge number of different methods, with different operational conditions to synthesize MOFs. Figure 3 summarizes the main methods for MOFs production.

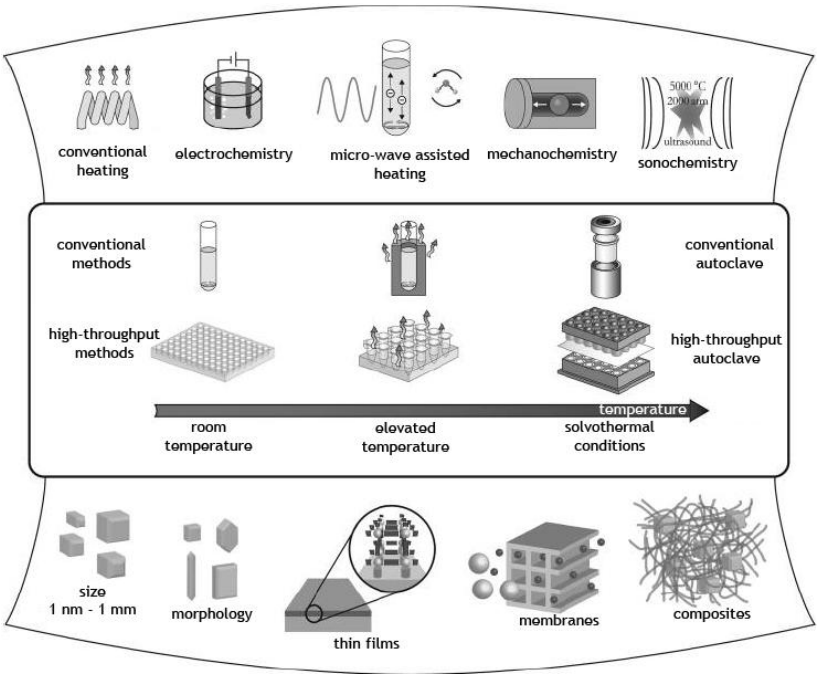

Figure 3. Overview of synthesis methods, possible reaction temperatures and final products [7].

Although different methods exist, it does not mean that a certain MOF can be produced by all of the methods described in Figure 3. Moreover, the same reaction mixtures can lead to different structures depending on the method that was used [7]. The method from which the MOF is synthesized may have a strong impact on reaction time, yields, particle size distribution and morphology. This is due to the complexity of the crystallization process, that requires appropriate kinetics to allow nucleation and growth of the desired MOF phase [7]. The implementation in large-scale processes is another complicated topic, regarding particles crystallization.

2.1.1 Synthesis routes

As mentioned before, there are a great number of different processes to create MOFs. Those processes involve different conditions and can be suitable for the production of some MOFs and not suitable for others. Reaction temperature is one of the most important parameters in MOFs synthesis [7].

Usually the process is divided into two different conditions: solvothermal and nonsolvothermal. Solvothermal reactions take place in closed vessels under autogenous pressure above the boiling point of the solvent, while nonsolvothermal reactions take place below or at the boiling point under ambient pressure [7].

The early works on this subject focused on the traditional crystallization techniques, such as precipitation. Precipitation is a widely used industrial process and is particularly important for the production of pharmaceuticals, paints and some polymers [16]. Precipitation often implies an irreversible process of crystallization. These processes are usually initiated at high supersaturation, resulting in fast nucleation and small growth rate of the crystals. Precipitation consists of three different physical stages, which are supersaturation, nucleation and growth (common to all crystallization processes), followed by two secondary steps, agglomeration and ageing. Theoretically, the mix of two reacting solutions should be enough to precipitation to occur. Nevertheless, nucleation does not necessarily initiate as soon as the reactants are mixed. It is crucial to understand all the *trade-offs* of this process. Supersaturation conditions, temperature, efficiency of mixing, intensity of agitation, presence of impurities are important factors that have to be taken into account [16].

One of the main difficulties of creating small particles is that the particles in suspension have a tendency to cluster together, in a process called agglomeration (aggregation, coagulation, flocculation are also used terms). Agglomeration occurs due to the collisions of particles, small enough for the van der Waals forces to exceed the gravitational forces.

The ageing stage is a process that covers all irreversible changes that take place in a precipitate, after its formation. One of the processes that occur in ageing step is the Ostwald ripening (proposed by Wilhelm Ostwald in 1896), which is a process where the small particles dissolve over time, and the solute redeposit onto larger particles, with the purpose to achieve a minimum total surface free energy (thermodynamically more stable) (Figure 4) [16].

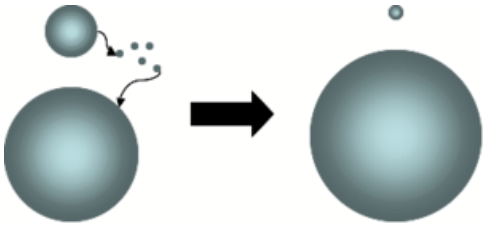

Figure 4. Scheme of the Ostwald ripening process.

In this process, the small particles disappear and the large particles continue to grow and the particles size distribution may become narrower.

Another important ageing process is the first-precipitation of a metastable phase followed by a phase transformation to the final product. This metastable phase may be an amorphous precipitate, or a polymorph of the final product.

For metal-organic frameworks production, the widely used precipitation technique is by direct mixing. A common method for producing a precipitate is to mix two reactant solutions together as quickly as possible. By definition, crystallization by precipitation involves a highly controlled supersaturated medium and it is extremely difficult to maintain uniform conditions of supersaturation throughout the reaction vessel. This means that the mixing quality is very important.

Some MOFs have been obtained from nonsolvothermal conditions (even room-temperature) by just mixing the raw materials (using a precipitation process), such as MOF-5, MOF-74, MOF-177, HKUST-1 or ZIF-8. Some of these MOFs (e.g. ZIF-8) show good thermal and chemical stabilities [7].

Chemical reactions often require some form of input of energy (either for solvothermal or nonsolvothermal conditions). This energy is generally introduced to the system by conventional electric heating, i.e., heat transferred from a hot source through convection. The different characteristics of the energy source may influence the final product and its morphology. Some alternative means of heating the reaction medium have been tested, such as electric potential, electromagnetic radiation, mechanical waves or by mechanical work [7, 18].

One of the most used processes is the energy supply by microwave irradiation, which is a well-established method in synthetic chemistry, but used mainly in organic chemistry [7]. Microwave-assisted synthesis relies on the interaction of electromagnetic waves with mobile electric charges. These charges can be polar solvent molecules/ions or electrons/ions in a solid. When the electromagnetic field is applied, and electric current is produced, the heating occurs due to the resistance of the solid (Joule effect). In solution, the polar molecules try to align in an electromagnetic field and in an oscillating field, so that the molecules constantly change their orientations, thus increasing their kinetic energy (and temperature) [7]. Microwave-assisted synthesis of MOFs has often been carried at temperatures above 100 ºC and reaction times not exceeding 1 hour. In general, irradiation of microwaves allows faster synthesis of smaller crystals, compared to conventional heating.

The electrochemical synthesis of MOFs was first reported in 2005 by researchers of BASF [7], with the purpose of excluding anions, such as nitrate, perchlorate or chloride, during the synthesis. Rather than using metal salts, the metal ions are continuously introduced through anodic dissolution to the reaction medium containing dissolved linker molecules and a conducting salt. The metal deposition on the cathode is avoided by using protic solvents,

forming H_2. The main advantage of this technique is the absence of both oxidant and reducing agents, which makes the final purification easier. Another advantage of the electrochemical route is the possibility of obtaining higher solids content, in a continuous process, compared to normal batch processes. Studies with this method have been done mainly with the mesoporous iron(III) trimesate MIL-100(Fe) and the microporous copper trimesate KHUST-1 [19]. It is a very simple method that takes place at atmospheric pressure.

The energy source can be a mechanical force that induces physical phenomena as well as chemical reactions. In simple terms, in this process, the intramolecular bonds are mechanically broken, allowing chemical transformation. This technique is well-known in synthetic chemistry, and has been employed in pharmaceutical industry, organic synthesis and polymer synthesis. Its use for synthesizing MOFs was first reported in 2006, producing the metal-organic framework $[Cu(INA)_2]$ [20]. Other structures like HKUST-1 or MOF-14 [7] have been synthesized by this technique. There are several advantages of this method. One of them is the possibility of producing solvent-free metal-organic frameworks, which is important in an environmental point of view. Short reaction times (in the range of 10-60 min) lead to reasonable yields and small particles.

Metal-organic frameworks can also be produced through sonochemical synthesis [7]. Sonochemistry is a technique that delivers ultrasound energy to the reaction medium. Ultrasound is a mechanical device that produces vibration with a frequency in the range 20 kHz and 10 MHz. The high-energy ultrasound interacts with liquids, alternating zones of high pressure with zones of low pressure – acoustic cavitation. In the low pressure regions, the pressure is lower than the vapor pressure of the solvent and the reactants, allowing small bubbles to be formed [21]. These oscillating bubbles can accumulate ultrasonic energy while growing (solute vapor diffuses into the bubbles). Under certain conditions, the bubble will grow until the critical size is achieved. In that point, the bubble collapses, releasing the stored energy, creating extreme conditions (temperatures of 5000 K and pressures of 1000 bar) that can result in chemical interactions between the reactants. It is important to state that the chemical reaction is not promoted by direct interactions of the ultrasound waves due to the fact that the wavelength is much larger than molecular dimensions. The primary goal of sonochemical synthesis in MOF chemistry was to find a fast, energy-efficient, environmentally friendly method, at room-temperature that can easily be carried out. Some studies have been done regarding the synthesis of metal-organic frameworks using ultrasound waves, producing MOFs such as IRMOF-9 and 10, MOF-5, MOF-177, MIL-53, MIL-88A and HKUST-1 [7].

The combination of different metal ions, organic ligands, solvent and synthesis method (as well as operational conditions) may result in an almost infinite number of different structures.

2.2 Potential Applications of MOFs

Metal-organic frameworks, as other porous materials (like zeolites or activated carbon), are very useful in gas storage, gas/vapor separation through adsorption phenomena, shape/size-selective catalysis, drug storage and delivery, and as templates in the preparation of low-dimensional materials. In this section, some of these applications will be discussed.

2.2.1 Hydrogen and methane storage

A tank charged with a porous adsorbent enables a gas to be stored at a much lower pressure than an identical tank without adsorbent. The fact that high pressure storage is not necessary using adsorbents provides safer (and more economical) gas storage. There are several studies of adsorbents for gas storage such as activated carbon, carbon nanotubes or zeolites. The growing interest of studies regarding the possibility of using metal-organic frameworks for gas storage it is due to its unique characteristics (tunable pore geometries and flexible frameworks) [2, 3, 22].

Hydrogen is an excellent energy carrier, due to its high combustion energy (almost 120 MJ/kg). Yet hydrogen is extremely hard to store in its gas state. Even to store hydrogen in liquid state, very low temperatures are required, as well as high pressure [3].

The current hydrogen storage techniques involve the use of high pressure tanks, cryogenic tanks, chemisorption and physiosorption. However, any of these techniques show limiting disadvantages that turn them unviable. MOF-5 was first used in 2003 for hydrogen storage [22]. Since then, almost 150 other MOFs have been tested. The storage of hydrogen in MOFs is due to van der Waals interactions between the hydrogen and the metal-organic framework (physical adsorption). The main advantage of MOFs for this purpose is the great surface area that presents (e.g. MOF-177 has a BET surface area of 4500 m^2/g). However the adsorption of hydrogen is only significant at low temperatures (77 K), which means that increasing the interactions between the MOF and hydrogen is crucial, which can be done changing the structure and geometry of the metal-organic framework. Catenation, when two or more identical frameworks interpenetrate each other could be used to generate MOFs with appropriate pore sizes, enhancing the interactions and the hydrogen adsorption capacity of the adsorbent (Figure 5) [23, 24].

Natural gas is another great energy carrier. Its main component is methane (>95%), while the rest is a mixture of ethane, other hydrocarbons, nitrogen and carbon dioxide. Its heat of

combustion is 50 MJ/kg (higher than gasoline, but lower than hydrogen). Nevertheless, its use is limited due to storage-related difficulties. Adsorption of methane is possible and several studies have been performed to analyze the use of MOFs such as MIL-53, PCN-11, PCN-14 or HKUST-1 for methane storage [7].

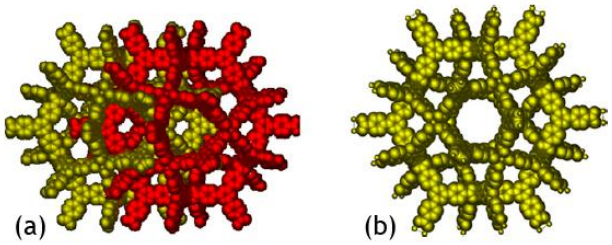

Figure 5. Catenation example of MOF PCN-6: (a) – Catenated PCN-6; (b) Non-catenated PCN-6 [23].

2.2.2 Gas adsorption selectivity

Adsorption is the main phenomenon that occurs between the surface of a solid and a fluid. Adsorption can have chemical properties, when there is bond formation between the solid and the fluid, or only physical properties, when the interactions are due to the van der Waals forces. With the ever-increasing demand for more environmentally friendly industrial applications, the use of mainly physical adsorption as a separation process of gases in chemical engineering has been higher than ever [7]. A mixture of gases can be separated by two mechanisms: different equilibrium with the adsorbent or different kinetics. Therefore, the selectivity of the adsorbent for an adsorbate is very important. The selectivity (as well as the capacity) of the adsorbent is dictated by its chemical composition and structure.

The principal mechanisms based on which selective gas adsorption is achieved in MOFs are adsorbate-adsorbent interactions (chemical or physical) and size-exclusion (molecular sieving effect). Selective gas based on sized-exclusion has been successfully shown with several MOFs, such as PCN-13 or PCN-17, for separation of O_2 and N_2 [7]. PCN-13 contains a square channel of 3.5 Å$\times$ 3.5 Å [7]. The larger the size of the N_2 molecule (kinetic diameter of 3.64 Å) as opposed to the O_2 molecule (diameter of 3.46 Å) completely prevents the nitrogen from entering the channels, while allowing oxygen to pass through the pores, meaning that the adsorbed volume of O_2 is higher than the volume of N_2 (Figure 6).

Cu(bdt) is another MOF that can separate O_2 from N_2 due to different interactions between these two components and the solid [7].

There has also been described some dynamic and flexible MOFs that allow the separation of gases via size-exclusion mechanisms or due to different interactions [7].

2.2.3 Catalysis in MOFs

As porous materials, MOFs may prove themselves useful in catalysis. Besides the high metal content of MOFs, one of their greatest advantages is that the active sites are rarely different because of the highly crystalline nature of metal-organic frameworks. The selectivity of MOFs as catalysts is achieved by the size or shape of the material that depend on the porosity and the presence of active transition-metal centers. Yet, only a few examples of MOFs have been reported for their use in catalysis [7].

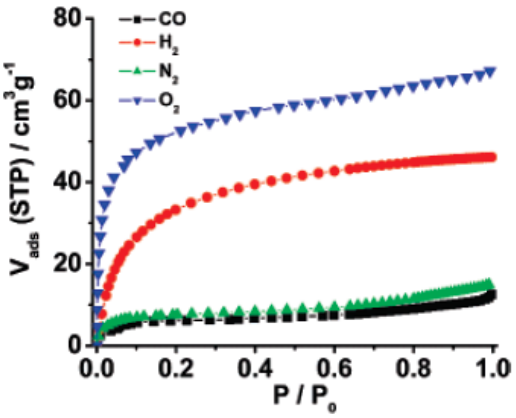

Figure 6. Hydrogen, oxygen, nitrogen and carbon monoxide adsorption isotherms of PCN-13 at 77 K [25].

2.2.4 Drug storage and delivery

Drug delivery is a method of administering a pharmaceutical compound to achieve a certain therapeutic effect. Drug delivery technologies modify the drug release profile and absorption, making it more convenient for the patient. Essentially, the developed delivery systems are classified into organic systems and inorganic systems. Organic systems have the advantage of having good biocompatibility and the ability to uptake many drugs. The inorganic delivery materials have the advantage of delivering the drugs at a controlled rate, due to their ordered porous network. Metal-organic frameworks are, as mentioned before, hybrid materials, i.e., have inorganic and organic properties, presenting themselves as optimal drug-delivery materials. However, the main problem of using MOFs for this purpose it that the small pore size (in the micro-range) limits the uptake or the number of drug molecules that can be stored within the framework. MOFs with mesopores (2 nm – 50 nm) need to be created for its use in drug delivery. MIL-100 and MIL-101 have shown to be suitable for drug delivery, due to their well-defined, ordered porosity (Figure 7) [5].

The difference observed in Figure 7 can be explained by the size of ibuprofen (6 Å× 10.3 Å) which is able to fit in both pentagonal (12 Å) and hexagonal (16 Å) windows of MIL-101, but not into pentagonal window of MIL-100 (4.8 Å) [5].

2.2.5 Other applications

Metal-organic frameworks possess other interesting properties that can be used for a wide variety of other applications, not listed above. For instance, the magnetic properties that MOFs present can be very useful. In fact, magnetic nanoparticles can be important in several applications, such as tumor targeted drug delivery, tumor ablation [26], magnetic separation, magnetic hyperthermia and MRI contrast enhancement [27]. The potential applications of MOFs depend on their behavior under the action of an external magnetic field, which depend on the intrinsic nature of the metal and the organic ligand, as well as the structure as whole. However, more studies in this area are required.

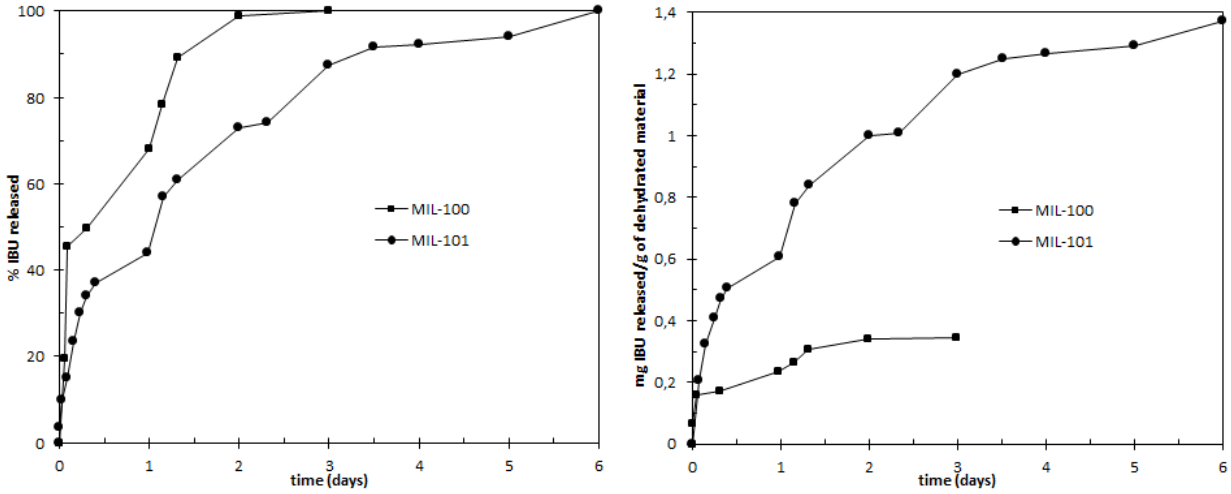

(a) (b)

Figure 7. Ibuprofen delivery ((a): % IBU; (b): mg IBU/g dehydrated material versus time for MIL-100 and MIL-101 [5].

Another potential application of MOFs is in the luminescence and sensors area. Luminescent materials can be prepared by combining the luminescent metal ions or clusters and organic ligands, as well as special guest molecules [3]. Metal-organic frameworks that possess luminescent properties together with size or shape-selective sorption can be used as sensing devices of ions (e.g. MOF-76), guest/solvent molecules (e.g. Eu(BTC)) or anisotropic photoluminescence probes (e.g. ITQMOF-1 and ITQMOF-2).

2.3 MIL-88A

The number of possible associations between inorganic moieties and organic linkers to form hybrid inorganic-organic porous materials is very large. In this work, a particular MOF was chosen, MIL-88A, a MOF developed and synthesized at *l'Institut Lavoisier*, a research institute from the *Université de Versailles* in France. MIL is the acronym used in MOFs produced at this laboratory.

MIL-88 [9] exhibits a 3D structure built up from trimers of iron (III) octahedral linked to organic anions to create a 3D framework. MIL-88 presents trimers containing 3 iron (III) atoms sharing a μ_3-O atom (the center atom in Figure 8). Each iron atom share, with other iron atom, an organic linker molecule. For MIL-88A, the organic ligand is fumarate, while for MIL-88B is terephthale, for MIL-88C is 2,6-naphthalenedicarboxylate and for MIL-88D is 4,4'-biphenyldicarboxylate. These 4 structures have in common the iron octahedral trimer shown in Figure 8. As the structure in Figure 8 links to each other, they form the so-called Secondary Building Units (SBUs).

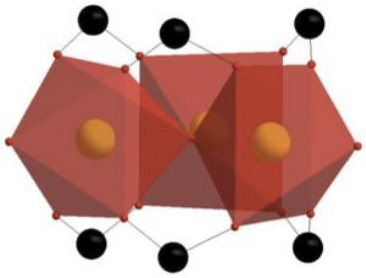

Figure 8. Trimer of MIL-88. Yellow: iron atoms; Red: oxygen atoms; black: carbon atoms [8].

Table 1 lists the cell parameters of the 4 types of MIL-88 and Figure 9 shows the predicted structures of these materials.

Table 1. Cell parameters of the MIL-88 type structures [28].

	MIL-88A	MIL-88B	MIL-88C	MIL-88D
a (Å)	11.18	11.05	10.22	12.05
c (Å)	14.68	18.99	23.60	27.50
V (Å^3)	1500	1980	2020	3500

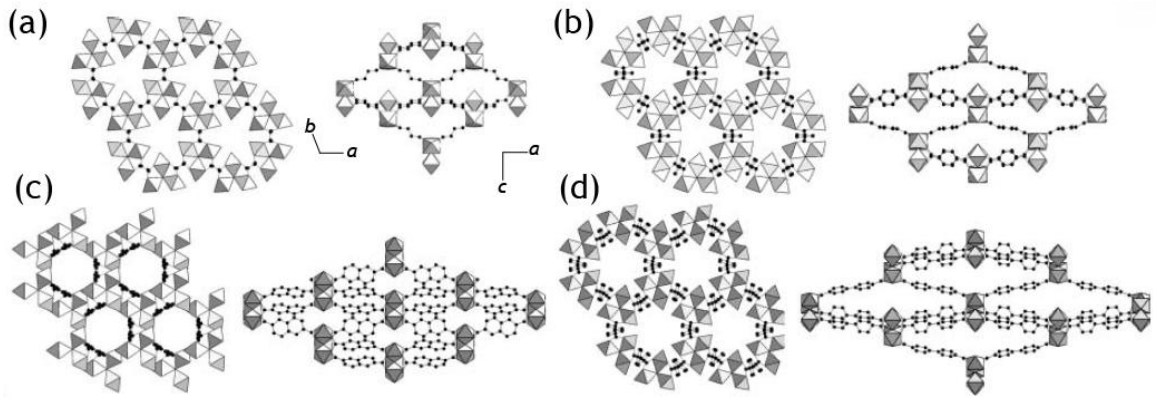

Figure 9 – Structures of the MIL-88 based topology: (a) MIL-88A (experimental); (b) MIL-88B (simulation); (c) MIL-88C (simulation); (d) MIL-88D (simulation). Left: along the a axis; Right: along the c axis [28].

The structure of MIL-88A delimits both a 1D pore-channel system along the c axis, which is filled with solvent molecules, and cages [9]. The free solvent molecules that are present within the pores interact through hydrogen bonds with oxygen atoms of the organic trimers. Also, van der Waals interactions between the solvent and the structures are predictable.

The chemical formula of MIL-88A is

$$Fe_3^{III}O^{\mu_3}(H_2O)_3\{C_4H_2O_4\}_3^+ \cdot nH_2O \cdot OH^-(\text{other anion}) \quad (2.1)$$

The 3 molecules of water present in the structure may change, depending on the used solvent, but each molecule of solvent gives one of its oxygen atoms to the trimer structure. The counter ion of MIL-88A is mainly hydroxide (from water), but may be any other anions present in solution.

The fumarate chains, represented by the black circles in Figure 10, are responsible to bond with other trimers, creating the porous framework of MIL-88A.

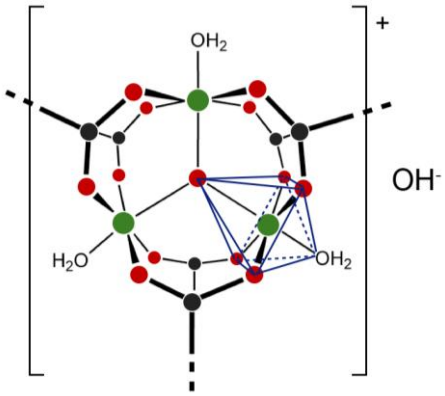

Figure 10. Molecular structure of MIL-88A trimer (each iron is bonded to the oxygen atom of water). Green: iron atoms; Red: oxygen atoms; black: carbon atoms.

MIL-88A has a density of 1.55 g/cm^3, corresponding well to the simulated density which is 1.73 g/cm^3 [9]. It usually presents a bimodal distribution of sizes [29]. The average pore size is about 6 Å [29].

The possible flexibility of MIL-88A has also been assessed [30, 31] indicating a very large swelling capacity upon post-synthesis treatments. In fact, the flexibility of metal-organic frameworks comes from their host-guest interactions. The change of the solvent, as well as the post-synthesis treatments (such as drying) also revealed differences in the crystalline structure of the network [30].

As can be observed in Figure 11, the XRD spectrums show different crystalline structures in each situation. This experimental information was useful to predict the structure, through computational simulations (Figure 12).

The synthesis methods of MIL-88A have been the subject of further development [18]. Some techniques listed above were used to produce this metal-organic framework, such as typical solvothermal (or hydrothermal) synthesis into a Teflon-lined steel autoclave, autogenous pressure synthesis, ultrasound and microwave synthesis.

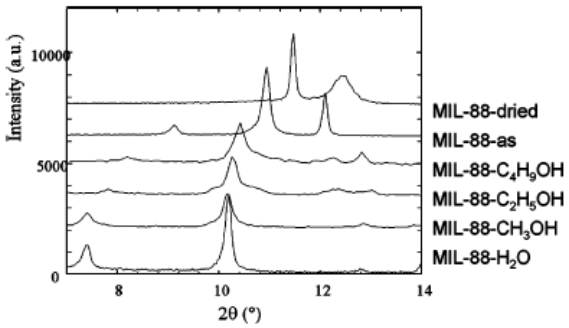

Figure 11. Experimental X-ray powder diffraction of MIL-88A, dried (423 K) as-synthesized (no post-treatment) or wetted with various solvents [30].

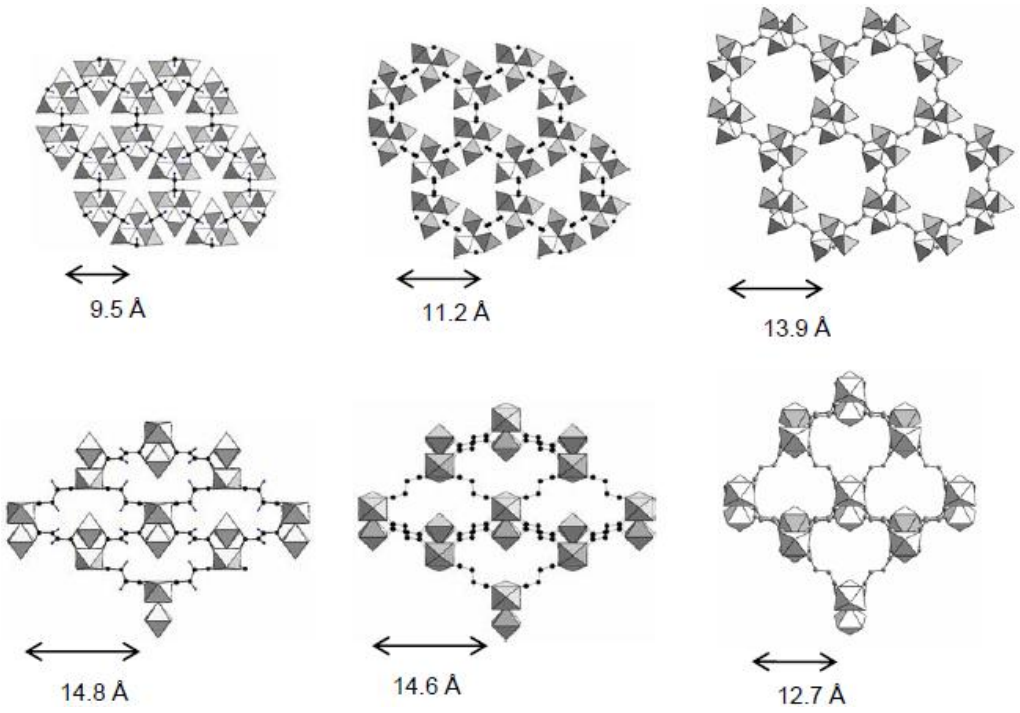

Figure 12. Simulated crystal structures of MIL-88A in its dry (left), as-synthesized (no post-treatment - center) and open (right) forms [31].

The effects of synthesis methods, solvents (dimethylformamide, ethanol, methanol or water), reaction time and temperature were studied with regard to particles size and yield [18]. The reactants to produce MIL-88A were iron (III) chloride hexahydrate and fumaric acid. The influence of adding acetic acid or sodium hydroxide was also studied. The use of alcohols as solvents decreased the reaction kinetics, due to competitive reactions (formation of fumaric acid ester), using a solvothermal approach [18]. Nevertheless, when pH was up to 2.7 by addition of sodium hydroxide, MIL-88A was obtained in methanol. Larger particles were

obtained when methanol or water is used as a solvent (probably due to the lower solubility of fumaric acid in these solvents, when compared with DMF). When water is used as solvent, it was observed that the particles size increased over time while the yield remained constant (which may be an indication of aggregation or ripening). Using methanol or DMF, both the particles size and yield increased with time (Figure 13).

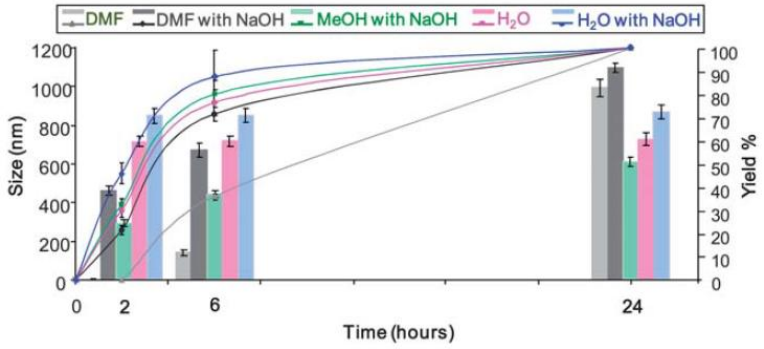

Figure 13. Particle size (curves) and yield (bars) as a function of time using different solvents [18].

It was also observed that the particles size increased with temperature (Figure 14), as well as the yields, meaning that higher temperatures promote the nucleation and growth of the particles. It was also observed that acetic acid worked as an inhibitor, while the addition of sodium hydroxide increased the reaction kinetics, which may indicate a significant influence of the pH over the crystallization phenomena of MIL-88A.

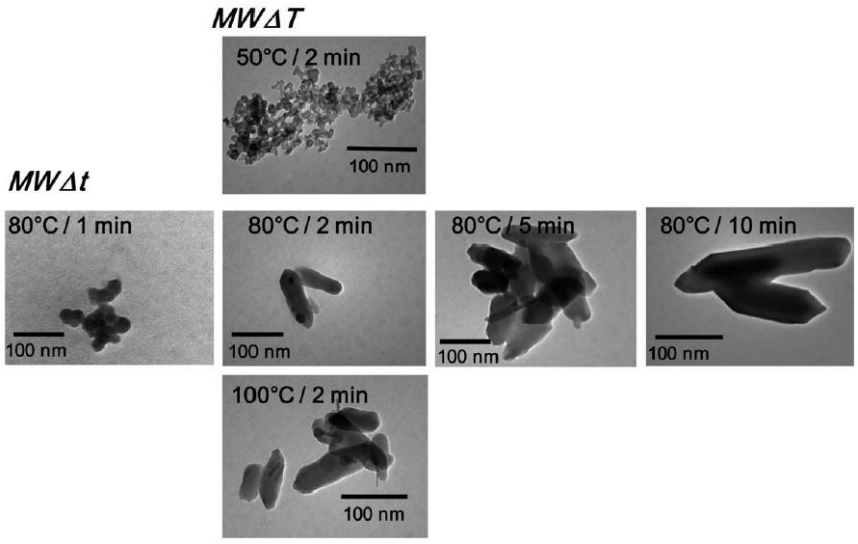

Figure 14. TEM images obtained from hydrothermal microwave synthesis of MIL-88A at various temperatures and synthesis times [18].

The microwave method presented very promising results. As can be observed in Figure 14, the rod-shaped MIL-88A is only obtained after a while (10 minutes at 80 ºC). The obtained yields were always above 40 % using the microwave assisted synthesis.

MIL-88A was chosen to test the properties of the existing NETmix® due to its synthesis simplicity (simply by mixing a fumarate source and an iron (III) source). This metal-organic framework can be synthesized in nonsolvothermal conditions (temperatures under 80 ºC) and at ambient pressure, enabling the production in the existing NETmix® reactor.

2.4 NETmix® Reactor

The main purpose of this work is the production of nanoparticles of MIL-88A at low temperatures and without recurring to high pressures, using the NETmix® technology.

NETmix® is a patented [10] new type of static mixer/reactor where mixing can be controlled effectively and efficiently making it particularly suited for complex and fast kinetics reactions. It consists of a network structure that combines two different types of elements (chambers and channels), organized in a 2D network [11, 12]. Networks are generated by the repetition of unit cells where each unit cell consists of one chamber and two inlet and two outlet channels oriented at a 45º angle from the main flow direction (Figure 15a) and can either be constructed from cylindrical chambers and rectangular cross section area channels (2D unit cell, Figure 15b) or from spherical chambers and cylindrical channels (3D unit cell, Figure 15c).

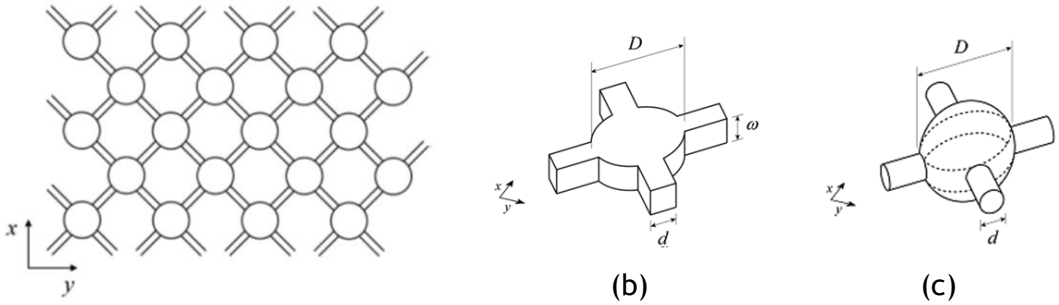

(a) (b) (c)

Figure 15. (a) Schematic representation of a network of chambers and channels; (b) 2D unit cell; (c) 3D unit cell [12].

To date, three prototypes were built for different purposes. The NETmix® 3D was the first prototype ever built and was constructed from two acrylic slabs where half chambers and channels were imprinted and then glued together (Figure 16a).

The Lab-scale NETmix® 2D was built for lab-scale projects with lower throughputs and was the reactor used along this work for the production of MIL-88A (Figure 16b). When larger throughputs are needed, the Multi-Inlet NETmix® 2D is used (Figure 16c). This prototype incorporates multi-inlet injection points along the reactor.

The transition to the 2D configuration represents a considerable decrease on the construction complexity since only one of the slabs has the chambers and channels imprinted. The two

slabs are no longer glued together allowing the disassembling and cleaning of the reactor, being insulation made by mechanical aperture and o-rings.

(a) (b) (c)

Figure 16. NETmix® prototypes: (a) NETmix® 3D; (b) Lab-Scale NETmix® 2D; (c) Multi-Inlet NETmix® 2D.

Laranjeira [12] observed that above a critical channel Reynolds number, the flow inside the mixing chambers evolves to a self-sustained oscillatory flow regime inducing local strong laminar mixing.

The Reynolds number in the NETmix® channels, Re, is defined as

$$\mathrm{Re} = \frac{\rho \bar{\upsilon} D_H}{\mu} \tag{2.2}$$

where ρ is the mixture's density (kg/m^3), $\bar{\upsilon}$ is the average velocity in the channels (m/s), D_H is the hydraulic diameter of the channels (m) and μ is the viscosity (Pa·s).

Homogenization in the chamber is almost instantaneous when the mixing dynamics is higher [12] (Figure 17). For this reason, chambers can be assumed to behave as perfectly mixing zones and the channels as plug flow perfect segregation zones.

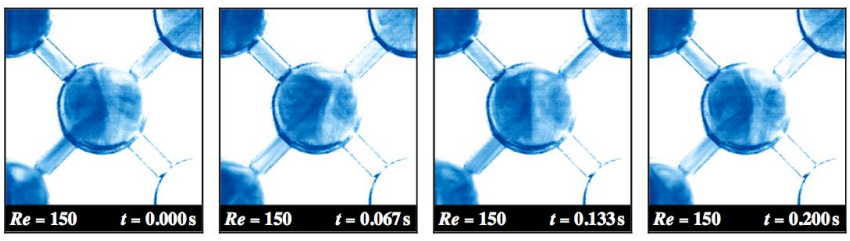

Figure 17. Tracer experiments at Re=150 [12].

Many of the existing continuous reactors used for nanoparticles production overcome the difficulty of controlling the mixing conditions by scaling down. The issue with downscaling is

the reduction of reactor throughput, and for that reason high volume production of nanoparticles is one of the major challenges for process engineers nowadays.

NETmix® links the control of mixing in the small basic units, channels and chambers, with large throughputs that are achieved by repeating the basic units as many times as necessary.

It has already been shown to be a promising industrial technology to produce nanoparticles with high reproducibility, mainly in terms of size distribution [14, 15], where the control of the stoichiometry of the reactants and micro and macromixing are key factors and was successfully used in hydroxyapatite nanoparticles production [14, 15], with high reproducibility, mainly in terms of size distribution.

In summary, the advantages of NETmix® in comparison to other static mixers are [14, 15]:

- Simple structure;
- Easy implementation of different pre-mixing reactants injection schemes;
- Ability to control residence time and to control mixing intensity and scale;
- Easy inclusion of temperature, pressure and concentration controls without modifying its dynamics;
- Large area promotes heat exchange, that can be used in temperature control;
- Scale-up is easy, since two or more NETmix® can be associated in parallel or in series.

3 Technical Description

3.1 Experimental Set-up

The main purpose of this work is to use all the capabilities of NETmix® for metal-organic frameworks productions. To do this, two different experimental set-ups were assembled: continuous flow reaction in NETmix® followed by ageing in a stirred flask and a batch reaction in a stirred flask with ageing in the same vessel.

The NETmix® reactor used in this work is a small unit, made of stainless steel and acrylic, with total volume of 22.9 mL, with 29 rows and 8 columns (more information in Appendix C).

The reactants were distributed through the inlets following a pre-mixed scheme (Figure 18).

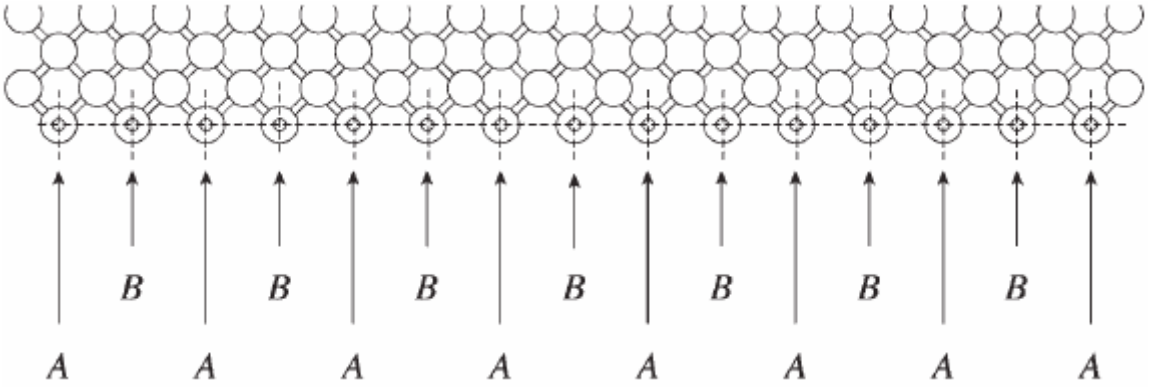

Figure 18. Pre-mixed injection scheme [12].

The reactants are fed to the NETmix® reactor by two pumps (Ismatec BVP-Z Standard). The final product is discharged to a flask under stirring where it ages for 72 hours (Figure 19).

In batch set-up (semi-batch to be more accurate), one of the reactants is placed on the stirred tank reactor (1 L), while the other is introduced in the system by a peristaltic pump (Ismatec MCP) (Figure 20). In order to ensure similar conditions, the flowrate of the peristaltic pump was chosen to take the same amount of time as the experiment in the NETmix® reactor. The reactant was injected directly above the stirrer blades. The rotational velocity of the stirrer was chosen to ensure that no visible stagnant zones occurred.

The experiments were performed at ambient pressure. The solvent that was used to prepare the reactant solutions is distilled water.

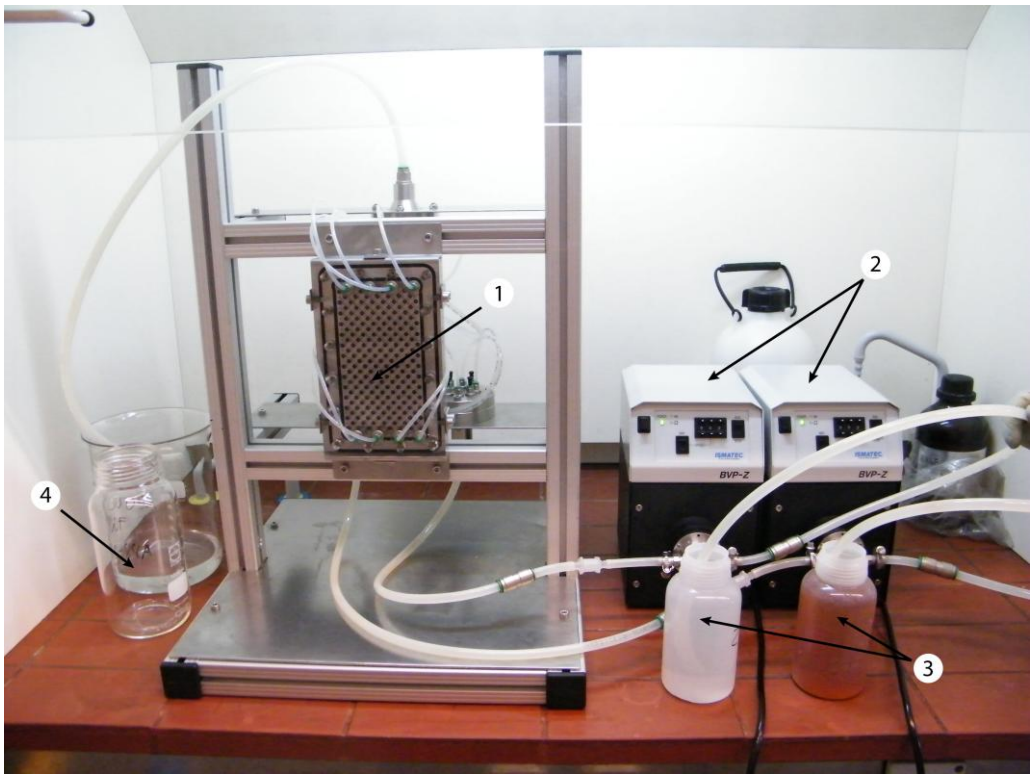

Figure 19. NETmix® reactor experimental apparatus. Legend: 1-NETmix® Reactor; 2-Feeding pumps; 3-Reactants vessels; 4-Final product flask.

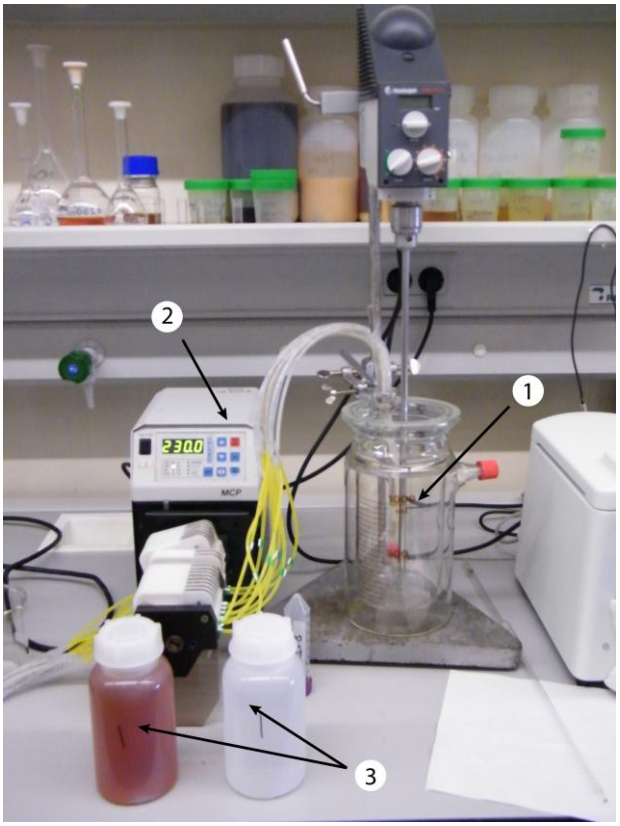

Figure 20. Batch experimental apparatus. Legend: 1-Batch reaction vessel; 2-Peristaltic pump; 3-Reactants vessel.

The iron (III) cations were provided from a solution of iron (III) chloride hexahydrate (98% purity from Sigma-Aldrich), $FeCl_3 \cdot 6H_2O$, and the source of fumarate anions is sodium fumarate dibasic (99% purity from Sigma-Aldrich), $NaO_2C\text{-}C_2H_2\text{-}CO_2Na$. Sodium fumarate was used instead of acid fumaric, because the latter has poor solubility in water. Therefore, there is no need of adding sodium hydroxide to increase the solubility of fumaric acid.

The chemical formula that represents the chemical reaction is:

$$3Fe^{3+} + 3\{C_4H_2O_4\}^{2-} + 5H_2O \rightarrow Fe_3^{III}O^{\mu_3}(H_2O)_3\{C_4H_2O_4\}_3^{+} \cdot nH_2O \cdot OH^- + 3H^+ \qquad (3.1)$$

Most of the experiments were performed at room temperature, but in order to study the effect of the temperature, a single experiment (in both reactors) was performed at 80 ºC. The reactants were heated up to 80 ºC, and the reactor temperature was set to the desired by passing hot water (in a closed circuit). Another experiment (batch) was performed to study the effect of the presence of a dispersant (see Table 2).

The following procedure was adopted. At the beginning and at the end (after 72 hours) of the ageing process, samples are collected and dried in a spray-dryer (Büchi Mini Spray Dryer B-290) to obtain a powder, that is used for SEM imaging, XRD, BET, DSC, TG, measurement of the particles size distribution, helium pycnometer method and mercury porosimetry. During the ageing process, approximately 30 mL of reaction solution was collected and centrifuged (Thermo Fisher Scientific Heraeus Multifuge X1R), for 30 minutes, at -5 ºC and a relative centrifugal force of 15000g. The solids were stored and the iron content in the supernatant was determined by atomic absorption spectroscopy.

In the performed experiments, the influence of 3 parameters in the final product was evaluated: Reynolds number in the NETmix® channels, reactants concentration and temperature.

In the first experiment N01, the Reynolds number and the reactants concentration were set to 600 and 0.4 M respectively. It was observed a strange phenomenon: blockage of some chambers of the reactor or no mixing (segregation of the flow) in the chambers. Either way, that was not the desired performance of the NETmix® reactor. To set the proper operational conditions of the NETmix®, in order to have good mixing in chambers, some rheological experiments were performed using a Paar Physica UDS 200 rheometer. The results of the rheological experiments are presented in section 3.2.1.

The series of experiments are presented in Table 2.

Table 2. Series of experiments.

Exp.	Process	$\mathrm{Re}_{\min}$	T (ºC)	C_{reac} (M)	Objective
N01	NETmix®	78	25	0.4	Study the influence of the Reynolds number in the process.
N02	NETmix®	600	25	0.4	
B02	Batch	n.a.	25	0.4	Comparison of the batch production with NETmix® final product N02.
N03	NETmix®	600	25	0.02	Study the effect of lower concentration.
N04	NETmix®	600	80	0.4	Study the effect of the temperature
B04	Batch	n.a.	80	0.4	Comparison of the batch production with NETmix® final product N04.
B05	Batch	n.a.	25	0.4	Study the effect of the addition of sodium citrate as a dispersant

3.2 Characterization

The following techniques were used to characterize the final product.

3.2.1 Rheological experiments

In order to understand the behavior of the reaction mixture, while flowing, rheological experiments were performed. The main motivation for this study is the fact that, at a Reynolds number of 600 (in the channels), blockage of the reactor or segregation of the flow was observed which might indicate that the mixtures viscosity increased to a value that makes the actual Reynolds Number below the critical value. The objective is to try to predict the viscosity increase and adjust the operational conditions of the reactor, in order to keep a good mixing quality.

The experiments were performed in a cone-and-plate rheometer. The used cone has a diameter of 75 mm and the angle between the surface of the cone and the plate is 1º.

Rotational experiments were made, keeping the shear rate constant and measuring the torque over time (during 60 seconds). The temperature was set to 25 ºC and kept constant by using a Viscotherm VT2. A few milliliters of each reactant were placed in the rheometer's plate. Both reactants were kept separated to avoid the contact between them (Figure 21) and to ensure that the reaction only occurs when the cone starts rotating and acquiring data. With these experiments, the relation between the solutions viscosity with time was obtained. This information is not only important to evaluate the increase of the viscosity, but can possibly give information about the crystallization kinetics.

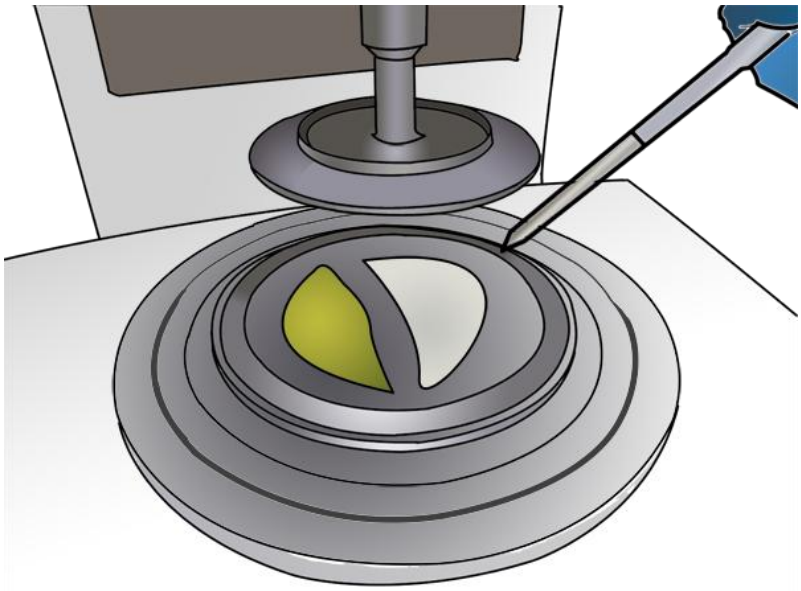

Figure 21. Schematic of the rheological experiments procedure.

The viscosity over time was measured for the following reactants concentrations: 0.08, 0.16 and 0.4 M. For each concentration, 4 different shear rates were tested: 366, 713, 1426 and 2852 s^{-1}, in a total of 12 different experiments. Each measurement was performed in triplicate to ensure reproducibility.

For every experiment, the same behavior was observed: in the first few seconds, the viscosity abruptly increases, reaching a maximum value, and then decreases, reaching a stationary value. The initial increase of the viscosity is expected due to the nucleation of particles that increase the flow resistance (see results in Appendix A).

Figure 22 shows, for each concentration, the maximum viscosity (which determines the minimum Reynolds number) as a function of the shear rate.

As can be observed in Figure 22, when the reactants concentration is 0.4 M, the viscosity can increase to up 25 times the water's viscosity (which was used to calculate the Reynolds number). It is observed that the maximum viscosity decreases with shear rate, for the same concentration. For a concentration of 0.4 M of iron chloride and sodium fumarate, the maximum viscosity decreases with shear rate according to equation 3.2, obtained by fitting the experimental data, using the method of least squares,

$$\mu_{max} = 894\dot{\gamma}^{-0.607} \tag{3.2}$$

where μ_{max} is the maximum viscosity (cP) and $\dot{\gamma}$ is the shear rate (s^{-1}).

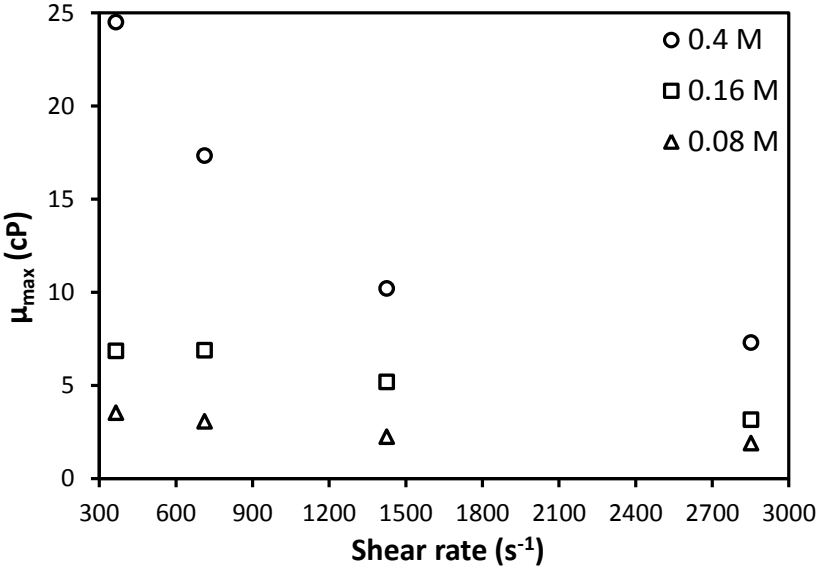

Figure 22. Maximum viscosity of the reaction mixture as a function of the shear rate at 25 ºC.

The shear rate in the channels of the NETmix® is given by (see Appendix C for more information)

$$\dot{\gamma} = \frac{6\bar{\upsilon}}{d} \tag{3.3}$$

where d is the channels depth (m).

This way, it is possible to determine the necessary flowrate for a given Reynolds number to be achieved.

3.2.2 Scanning Electron Microscopy (SEM) and Energy Dispersive Spectroscopy (EDS)

Scanning electron microscopy is a widely used technique for obtaining particles images. It scans the sample with a beam of electrons that interacts with the surface of the sample, emitting different signals that contain information about the surface's topography. Those signals are detected and converted to high-resolution images.

EDS is an analytical technique used for elemental characterization of a sample. The X-ray emitted by the sample due to the transitions of electrons from outer to inner layers is measured, and the energy spectrum can be related to the chemical element.

The used equipment for the analysis (owned by CEMUP - Centro de Materiais da Universidade do Porto) is a Jeol JSM 6301F microscope with Oxford Inca Energy 350 energy dispersive X-Ray system.

The samples were prepared by fixing the powder in a conductive carbon tape, which is fixed in a metallic holder. The samples needed to be coated with gold (for 220 seconds), due to its

low conductivity that leads to charge effect (accumulation of charges that lead to very bright images).

3.2.3 Dynamic Light Scattering (DLS)

Dynamic light scattering (also known as photon correlation spectroscopy) is a technique that measures the Brownian motion of the particles and relates with their sizes. The particles' field is illuminated with a laser and the intensity fluctuations in the scattered light is analyzed. The particles size distribution is then correlated and determined from the acquired data.

The particles size distribution was measured using a Malvern ZetaSizer Nano ZS ZEN 3600. To measure the particles size distribution, the solids were diluted in ethanol, in a concentration of 1 mg/mL, kept under agitation of a magnetic stirrer for 3 minutes and then ultrasound waves were applied to the sample (for 3 minutes) at 30% of amplitude (using Hielscher UP50H ultrasound device). It was necessary to change the definitions of the ZetaSizer software, due to the solvent change. The following ethanol properties were used: $RI = 1.360$, $\varepsilon_r = 24.3$ and $\mu = 1.04$ cP [32, 33].

3.2.4 Electrophoresis (Laser Doppler Velocimetry)

Electrophoresis is the motion of dispersed particles under the influence of a uniform electric field. The dispersed particles have an electric surface charge, on which external field exerts a Coulomb force, and they are attracted towards the electrode of opposite charge. When the equilibrium is reached, the particles move with constant velocity (called electrophoretic mobility). The electrophoretic mobility is measured using the laser doppler velocimetry (LDV) technique, which uses the Doppler shift in a laser beam to measure the velocity of the particles. The electrophoretic mobility is then used to determine the zeta potential of the particles surface.

The zeta potential is the electric potential in the interfacial double layer at the location of the slipping plane versus a point in the bulk fluid, away from the interface (Figure 23).

The zeta potential is an important value that can be related to the stability of the dispersion. It indicates the degree of repulsion between adjacent, similarly charged particles in dispersion. High values of zeta potential (above 60 mV - absolute value) indicate that the dispersion is stable, and has no tendency to flocculate. Low zeta potential means that the attraction exceeds repulsion and the particles will flocculate, creating clusters.

The equipment used to determine the zeta potential distribution is the Malvern ZetaSizer Nano ZS ZEN 3600 using the folded capillary cell (DTS1060). The samples were prepared by

diluting the solution 25 times in water to ensure that the sample's concentration is within the working range of concentrations of the device.

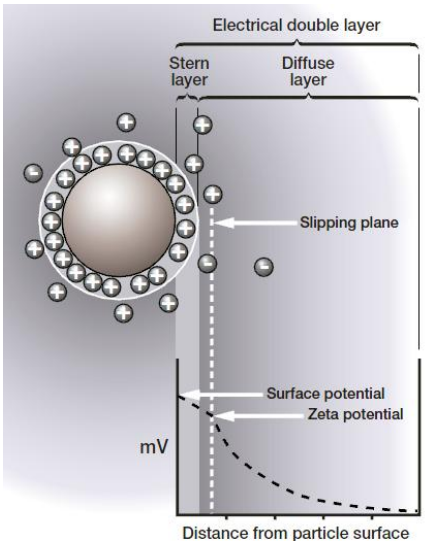

Figure 23. Electrical layers of the surface particles [34].

3.2.5 Atomic Absorption spectroscopy

Atomic absorption spectroscopy is a method that measures the absorption of radiation and can be related to the concentration of a chemical species in a solution. This technique was used to determine the concentration of iron in the supernatant, thus making possible the determination of the chemical conversion of iron in MIL-88A.

The equipment used for atomic absorption is a GBC 932 Plus. The samples needed to be diluted in water in order to the iron concentration be within the detection limit range (2-145 mg/L).

3.2.6 X-Ray Diffraction (XRD)

X-Ray diffraction is an X-ray scattering technique used to identify unknown crystallized substances. The XRD spectrum gives information about the crystalline structure of the sample and allows the identification of the structure, by comparing the spectrum with spectrums of known substances.

These measurements were performed at Institut Lavoisier. The equipment used to obtain XRD spectra is a Bruker D8, equipped with an eye-Lynx detector (with a copper source).

3.2.7 Differential Scanning Calorimetry (DSC) and Thermogravimetric (TG) analysis

Differential scanning calorimetry is a technique widely used in the field of thermal characterization of solids. It is a technique in which the sample is heated (with constant heating rate) and the difference in the amount of heat required to heat the sample and the

reference is measured. This way, information about the heat capacity of the solid, as well as phase transitions can be visualized by this technique.

Thermogravimetric analysis is very similar to DSC, but instead of determining the heat flux, it determines the weight variations with increasing temperature, in a controlled atmosphere.

DSC and TG measurements were performed by Professor Joaquim Faria, from the Laboratory of Catalysis and Materials (LCM).

3.2.8 Nitrogen Adsorption

The specific surface area, an important property in porous materials, can be measured by nitrogen adsorption. A sorption isotherm is obtained and can be used to calculate the specific surface area using the BET (Brunauer-Emmett-Teller) theory. This theory assumes that the nitrogen is absorbed in infinite multilayers and there is no interaction between the different layers, making possible to apply the Langmuir theory to each layer.

Surface area measurements through BET method were performed by Professor Joaquim Faria, from the Laboratory of Catalysis and Materials (LCM).

3.2.9 Helium Picnometer Method and Mercury Porosimetry

These two combined techniques are used to determine two characteristic values of porous solids: the true density and the apparent density. Helium picnometeter method allows the determination of the true density, measuring the volume of helium displaced by a given sample mass. As helium is a small molecule, one can assume that it penetrates all the pores of the solid, so the displaced volume corresponds only to the volume of the material.

In the opposite way, the penetration of mercury in the pores is only possible with the action of an external force. The apparent density and porosity can be determined by mercury porosimetry.

The equipment Quantachrome Poremaster 60 was used for the porosimetry experiments, with a detection range of 0.0036-950 μm.

4 Results and Discussion

Table 2 shows a list of the set of experiments and the respective parameters.

The first experiment N01 was performed using the NETmix® reactor, with iron chloride and sodium fumarate at a concentration of 0.4 M. Assuming water density and viscosity, a flowrate of 1.03 L/min was used in order to achieve the desired Reynolds number equal to 600, well above the critical Reynolds number for the onset of mixing [12]. However, as the experiment progressed, segregation of the flow inside the reactor was observed, indicating a lower Reynolds number than the one expected. Blockage of some channels was also observed.

Using the approach described in Section 3.2.1, for a concentration of 0.4 M, the fluid viscosity is at least 9 times higher than the viscosity of water (see Figure 22) resulting in a Reynolds number close to 78, well below the critical Reynolds number. After the reaction in NETmix®, the final product was aged for 72 hours. A sample of the aged solution was dried in the spray-dryer. During the ageing process, some samples of solution were removed and centrifuged. Only in this solution were performed zeta potential measurements.

Experiment N02 was done with the same parameters as experiment N01, but now with the Reynolds number calculated with the solution viscosity estimated from the approach described in Section 3.2.1, leading to a flowrate of 3.6 L/min ($Re = 600$). The experimental procedure was similar to the one in the experiment N01. However, before the ageing started, a sample was removed to be dried. The pH was monitored to detect variations. Experiment B02 was performed in a batch reactor, with the same protocol as experiment N02.

In experiment N03, the reactants concentration was set to 0.02 M, which leads to a distance between nanoparticles per length of nanoparticle of 2.12 (an important parameter to avoid aggregation - see Appendix D). The flowrate was set to 1.8 L/min ($Re = 600$).

In experiments N04 and B04, the temperature of the reaction was set to 80 ºC. In these experiments, the ageing process was not necessary. Therefore, the progress of the conversion of iron in the ageing stage was not studied. In experiment N04 the flowrate was set to 3.6 L/min, as in experiment N02.

In experiment B05, sodium citrate was added as a dispersant with a concentration 10 times higher than the theoretically necessary to coat all particles (see Appendix E). This sample was only characterized by SEM and XRD.

For experiments N02, B02 and N03, the pH was monitored during the ageing process (Figure 24). As expected, in N03 sample (with lower concentration) the pH is higher than in N02 and B02. However, the pH tends to decrease with time, to a value close to 0.88 in the formulation

with 0.4 M of iron chloride and sodium fumarate, and 2.17 for N03. This means that during the ageing process, chemical reaction may occur (nucleation).

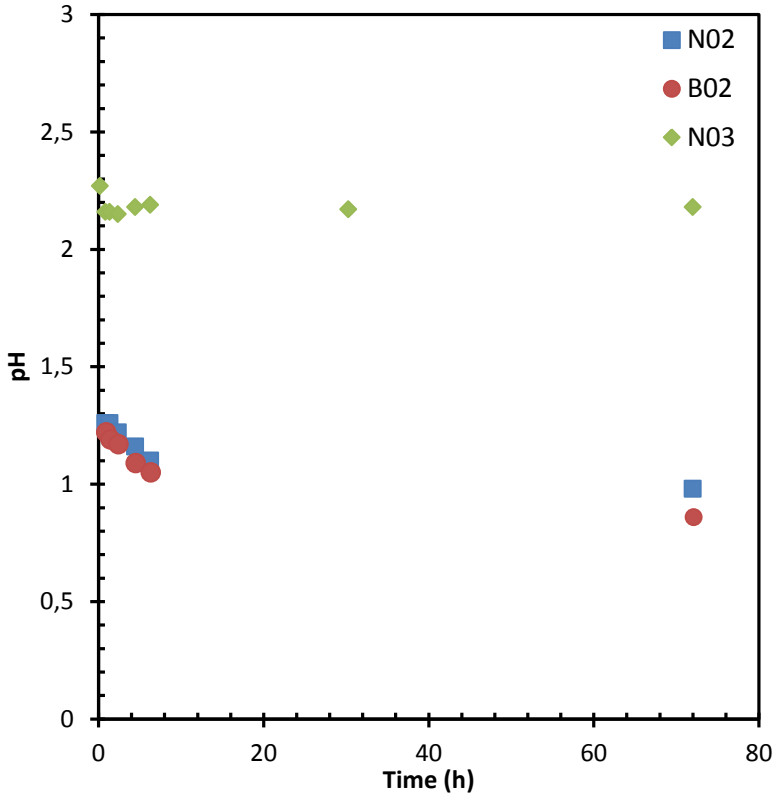

Figure 24. pH variation with time in the ageing stage.

4.1 Zeta potential

The zeta potential measurements were performed for sample N01, after several hours of maturation (72 hours). To measure the zeta potential, dilutions were necessary (due to equipment limitations). The experiments were performed with dilution factor between 25 and 200. The effect of the pH in zeta potential was tested, in order to analyze particles stability and their tendency to aggregate. Addition of sodium hydroxide or hydrochloric acid was necessary to control the pH of the dispersion.

Figure 25 shows the mean zeta potential of the MOF as a function of pH, for different dilution factors. The dashed line in Figure 25 represents only a tendency of the mean zeta potential variation with pH (does not represent any theoretical model).

It can be observed that different dilution factors lead to different initial pH (the addition of water in the dispersion varies the pH of the sample). However, it appears that the dilution factor is not a crucial parameter when compared with the pH. The initial pH of the solutions for the different dilution factors are presented in Table 3.

Dilution has an effect on the initial pH, which in turn has an effect on the value of mean zeta potential. However, the mean zeta potential variation in this region is not very significant and the suspension is moderately stable.

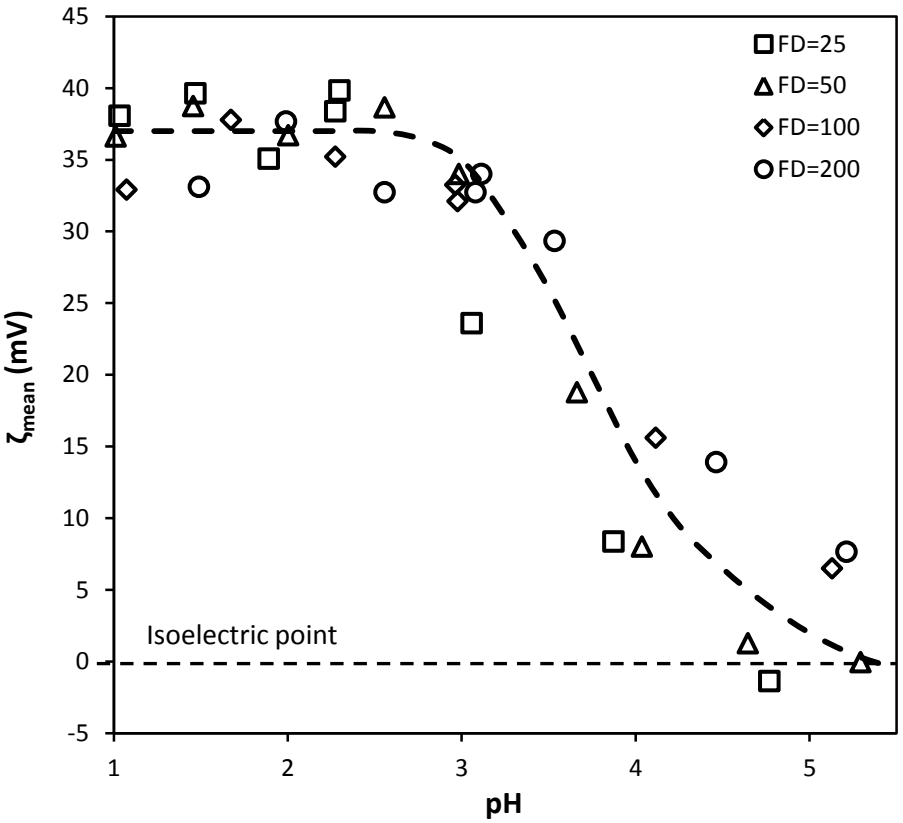

Figure 25. Zeta potential measurements: mean zeta potential as a function of pH. Isoelectric point is the point where the zeta potential is zero.

Table 3. Initial pH values and mean zeta potential for different dilution factors.

Dilution factor	Initial pH	ζ_{mean} (mV)
25	2.27	38.4
50	2.55	38.8
100	2.98	32.1
200	3.08	32.7

The presented values of zeta potential are mean values but the measurements result in a distribution as shown in Figure 26.

Therefore, there are regions with high stability and regions with low stability, meaning that the charge distribution in the double layer is not uniform. Some particles (or regions) have the tendency to aggregate, while others are stable. In fact, when the sample was diluted, flocculation was observed.

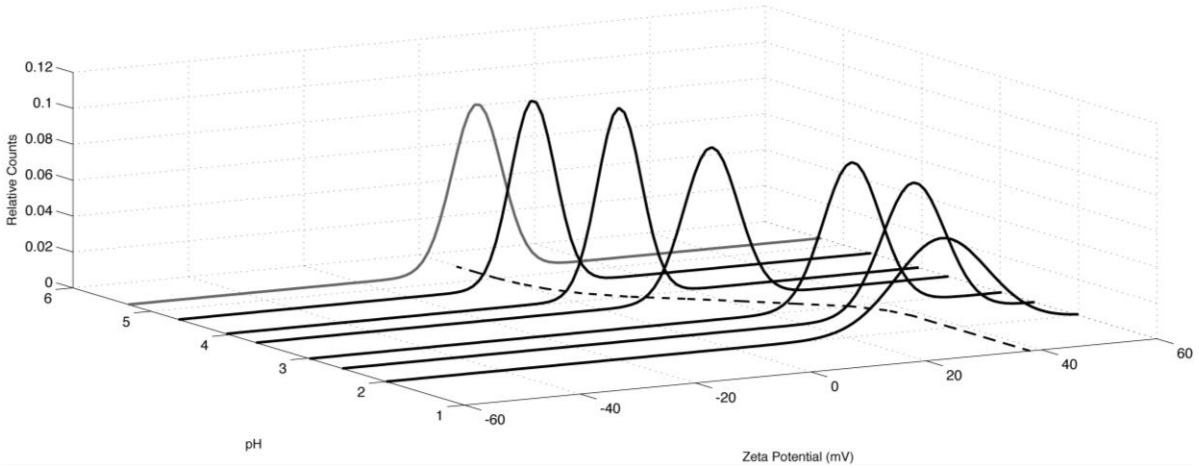

Figure 26. Zeta potential distributions for different pHs.

It was also observed a color change in the solutions when the pH is above 4. Also, in this region, the pH was not stable with time, having the tendency to decrease. This is probably due to the formation of iron oxide and/or the break of the carboxylate bonds of the fumarate chains, destroying the framework. Therefore, and also because of its low mean zeta potential, it is not advisable to work at pH over 4.

It can also be concluded that decreasing the pH does not change the zeta potential in a significant way.

The zeta potential of N01 sample with sodium citrate (10 times higher the reference concentration) was also measured. The addition of sodium citrate occurred after the ageing process. The mean zeta potential value is close to -11 mV, meaning that the suspensions stability is poor.

4.2 Iron (III) conversion

In experiments N01, N02, B02 and N03, some samples were collected and were centrifuged (after 0, 0.5, 1, 2, 4, 6, 30 and 72 hours of maturation). With the supernatant, it was possible to measure the amount iron, thus leading to a chemical conversion. Knowing the volume of the supernatant, by a simple mass balance, it is possible to determine the amount of unreacted iron in the flask. The amount of iron in the supernatant was determined by atomic adsorption spectroscopy. The results are presented in Figure 27.

The conversion of the iron ions was calculated using the following equation

$$X_{\mathrm{Fe}} = 1 - \frac{C_{\mathrm{Fe},t}}{C_{\mathrm{Fe},0}} \tag{4.1}$$

Where X_{Fe} is the iron conversion, $C_{\mathrm{Fe},t}$ is the iron concentration at instant t (M) and $C_{\mathrm{Fe},0}$ is the initial iron concentration (M).

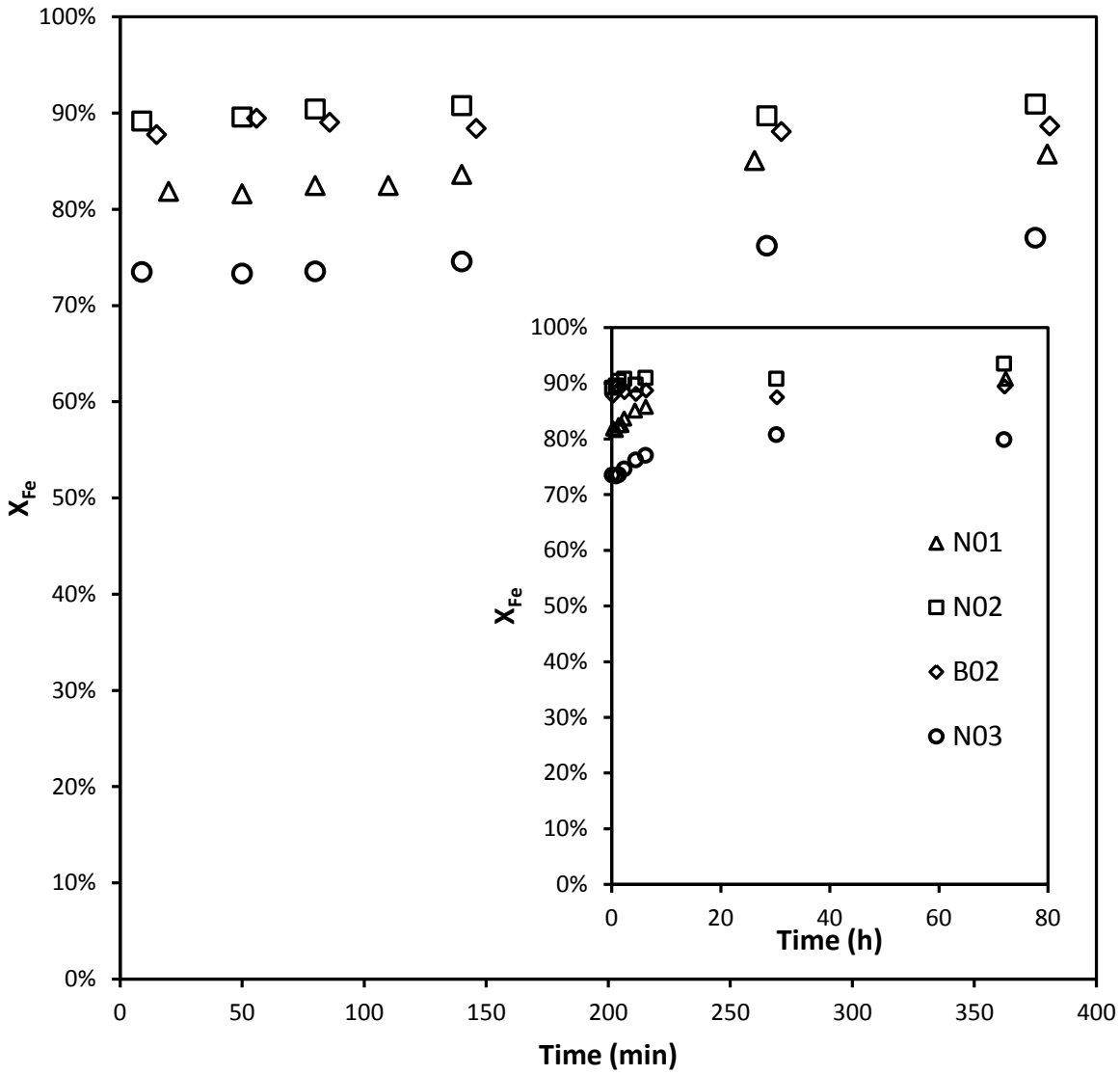

Figure 27. Iron conversion as a function of time, during the ageing stage.

It is not a surprise that experiment N03 presents a lower conversion of iron, therefore less MOF produced, since the reaction rate is favored by higher concentrations. As expected, N02 presented a slightly higher conversion than B02, but the difference is not enough to state that the mixture quality is a crucial parameter in this process. Experiment N01 presented higher conversion than N03 (due to higher concentration of reactants) but lower than N02 and/or B02. This may be explained by the lack of mixing, due to the unexpected increase of viscosity, in the chambers of the NETmix® reactor for N01 experiment that may have lead to a lower conversion at the beginning of the ageing step.

The increase of the conversion indicates that the reaction still occurs in the ageing process (as concluded by the decrease of the pH). However, the conversion does not reach 100 % even after 72 hours of maturation. This can indicate one of three things:

- the presence of iron in excess that cannot react with fumarate (the fumarate has been all consumed or possibly trapped in the framework). To test this theory it is necessary to measure the concentration of fumarate in solution;
- a chemical equilibrium has been achieved, therefore it is not possible to have higher conversions;
- the maturation time was not enough to achieve full conversion, which is likely due to the fact that the reaction kinetics decreases with time, because the reactants concentrations in solution are lower.

4.3 Particles size distributions

As mentioned previously, a determined procedure was followed for the measurement of particles size distributions. The particles (in suspension or dried) were re-suspended in ethanol, in a concentration of approximately 1 mg/mL, under magnetic stirring (for 3 minutes). Afterwards, the suspension was under the action of ultrasonic waves, with the intent to disaggregate the particle clusters (for 3 minutes). The number particle size distribution results for all the samples are shown in Figure 28 to Figure 31.

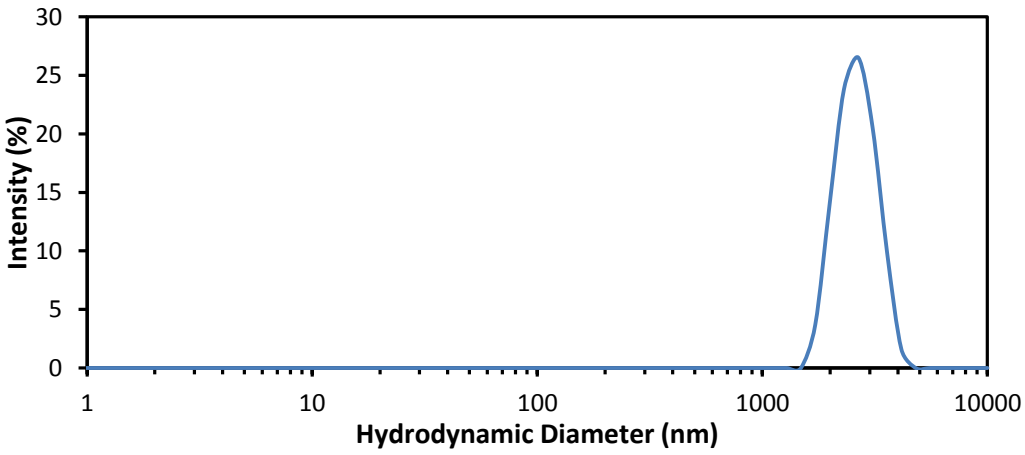

Figure 28. Particle size distribution of sample N01 after 72 hours of maturation.

The samples that presented lower mean hydrodynamic diameter were samples N02 and B02 (Figure 29). In Figure 29, the second peak in the N02 (0 h) curve is due to the spray-dryer clusters that were not disaggregated by ultrasound waves. N01 presented the larger mean diameter (Figure 28). The difference between N01 and N02 is the Reynolds number, i.e., the mixing conditions. In fact, in N01 experiment, the mixing may not be uniform in the chambers, originating regions of low supersaturation that inhibits the nucleation of the particles. Therefore, the number of particles is possibly allowing the particles to grow larger.

The N03 sample has a higher mean free path than N01 or N02. Therefore, the interactions between particles are lower. But what is observed is that the mean diameter is greater than,

for instance, the mean diameter of sample N02. As explained before, the supersaturation promotes the nucleation, therefore, in sample N03 the nucleation rate is much lower than in sample N02. If fewer particles are produced in sample N03, the more they can grow from the reactants in solution.

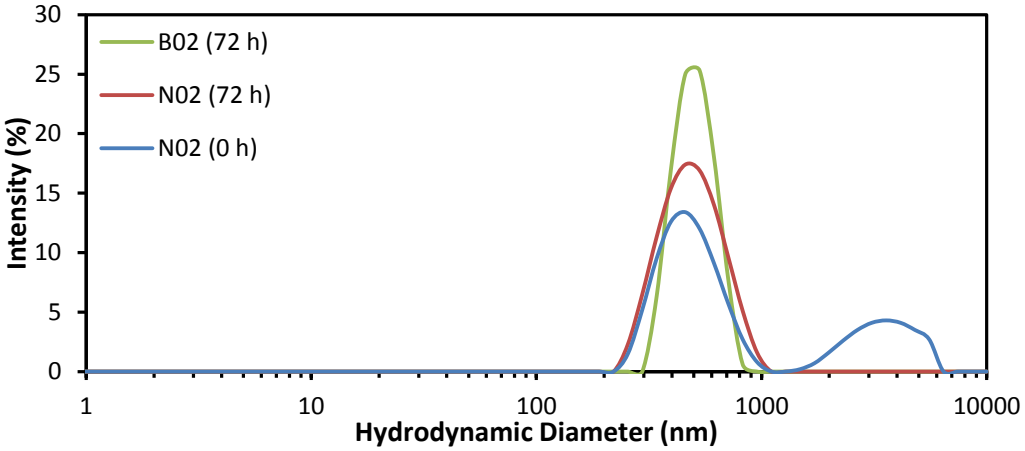

Figure 29. Particles size distribution of samples B02 (after 72 hours of maturation), N02 (after 72 hours of maturation) and N02 (dried, no maturation).

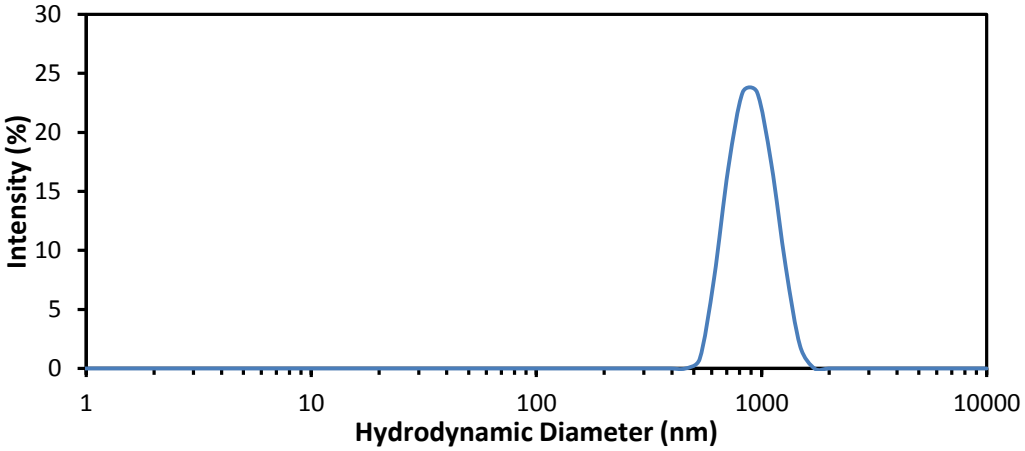

Figure 30. Particle size distribution of sample N03 after 72 hours of maturation.

Figure 31 shows the particle size distributions for experiments N04 and B04 done at 80 ºC and give the most interesting results. The particles in N04 and B04 are larger than in experiments N02 and B02 (done with at room temperature with the same flowrate), an expected result, since higher temperatures promote not only the nucleation, but also increases the growth rate of the particles. The difference between N04 and B04 can be explained by the change of the predominant mechanism (mass transfer and/or chemical reaction). In N02 and B02, at room-temperature, the process is controlled mainly by crystallization kinetics. Mixing is necessary, but its quality is not crucial. At 80 ºC, the crystallization kinetics is possibly considerably higher and the process is controlled by mass transfer, which can explain the

difference between N04 and B04 since limitations to mass transfer is lower in NETmix® reactor.

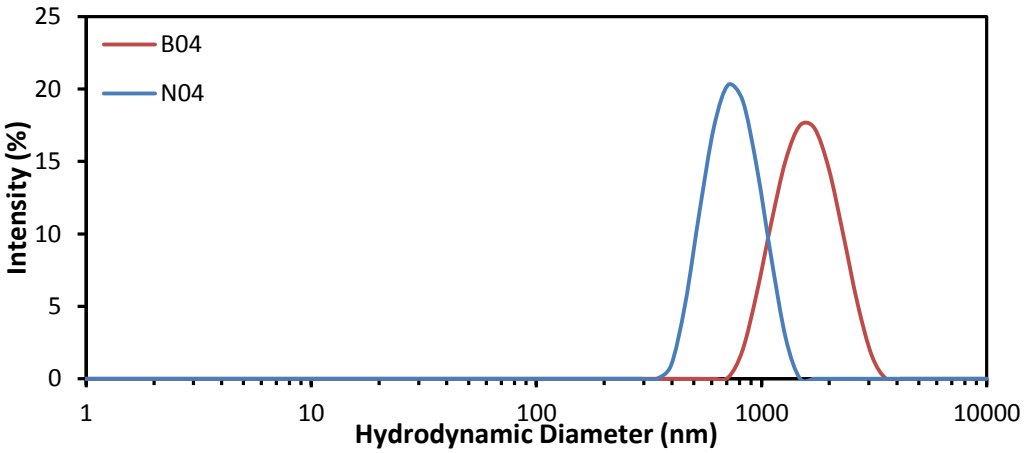

Figure 31. Particle size distribution of samples B04 and N04, both after 72 hours of maturation.

It is important to emphasize the fact that DLS measurements present the hydrodynamic diameter that is the diameter of a hard sphere that diffuses at the same rate as the real particle. Therefore, a shape factor is necessary to convert these results.

4.4 SEM and EDS analysis

With SEM analysis, it is possible to understand more about the morphology and size of the particles. The most important results are presented in this section (Figure 32 to Figure 36), however the complete series of images is presented in Appendix B.

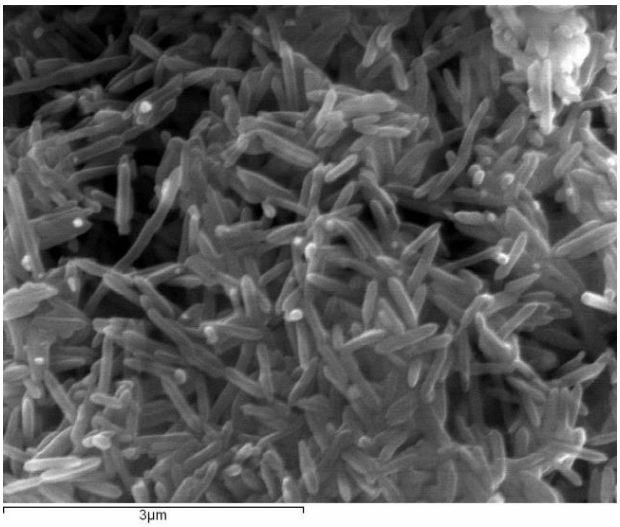

Figure 32. SEM image of sample N01 (72 hours).

As can be observed in Figure 32, Figure 33b and Figure 33d, samples N01, N02 and B02 have a crystalline structure, with rod-shaped crystals with approximately 600 × 100 nm, after 72

hours of maturation. Conversely, samples N02 and B02 that did not go through a maturation step show an amorphous structure (Figure 33a and Figure 33c). Therefore, the maturation process is an important step for obtaining MIL-88A phase at room temperature. Sample N03 presents two distinct particles: amorphous-like particles; big rod-shaped particles with an approximate size of 2500 × 500 nm (Figure 34).

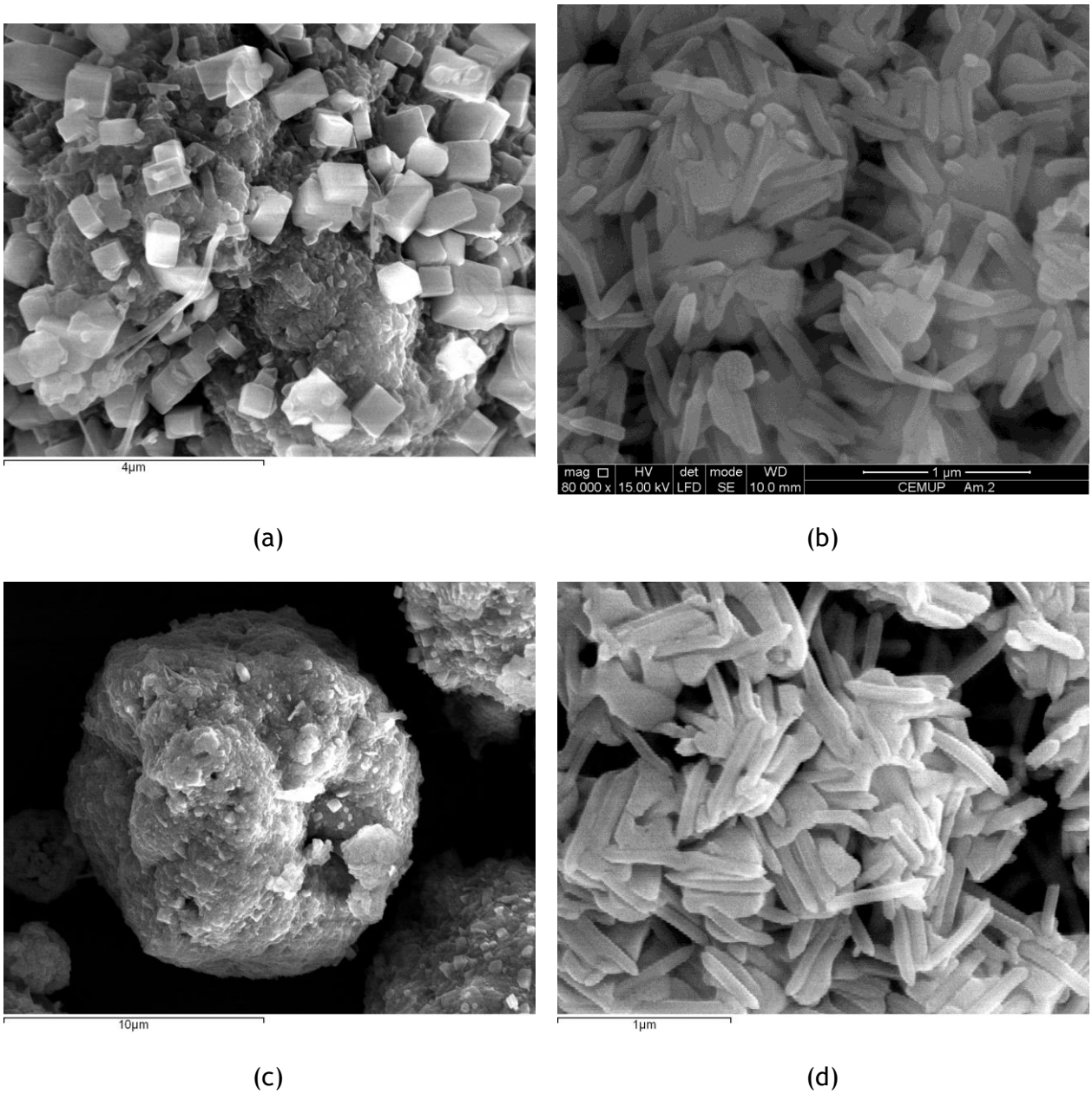

Figure 33. SEM images of samples N02 and B02: (a) N02 (0 hours); (b) N02 (72 hours); (c) B02 (0 hours); (d) B02 (72 hours).

Another important observation is that in samples N04 and B04 rod-shaped crystals are immediately formed, even without ageing. However, the crystals formed in these samples are larger, with 2000 × 300 nm, when compared to the N02 sample. Sample B05 is mostly amorphous but some crystals are already visible.

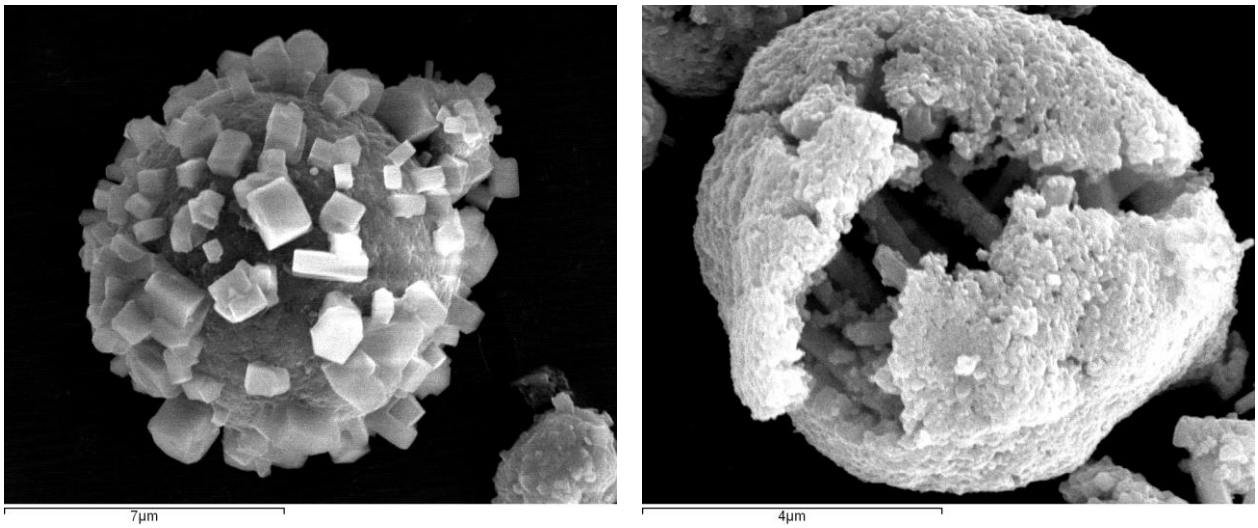

(a) (b)

Figure 34. SEM images of sample N03: (a) 0 hours; (b) 72 hours.

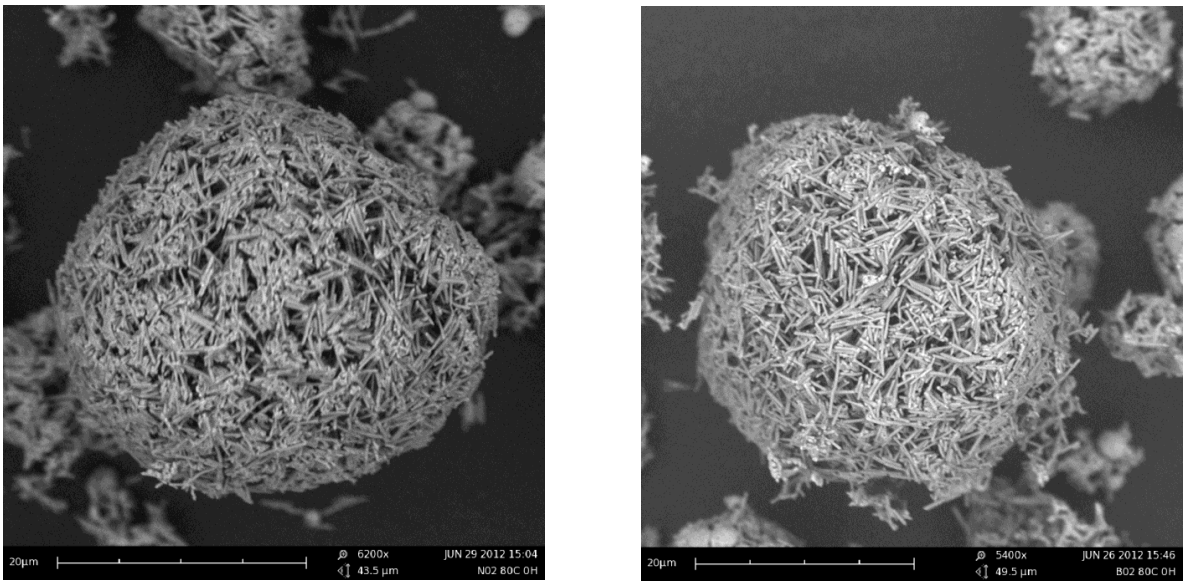

(a) (b)

Figure 35. SEM images of samples: (a) N04 (0 hours); (b) B04 (0 hours).

Several conclusions can be taken from the SEM analysis. The maturation process is very important for the crystallization of MIL-88A, at room-temperature. In fact, if the sample is not aged, the MOF is presented in some form of metastable phase that will evolve to a crystalline structure during the maturation process. However, this stage is not necessary when the reaction temperature is held at 80 ºC, probably because the energy requirements for the phase transition to occur are now satisfied. Moreover, the increase of temperature promotes the increase of the crystal growth rate, leading to bigger particles. Mixing does not seem to be a crucial parameter, because at different mixing conditions the particles seem to

have the same size and shape. Therefore, the DLS results were not validated by SEM imaging. The differences between N04 and B04 cannot be explained by the difference of the mixing conditions.

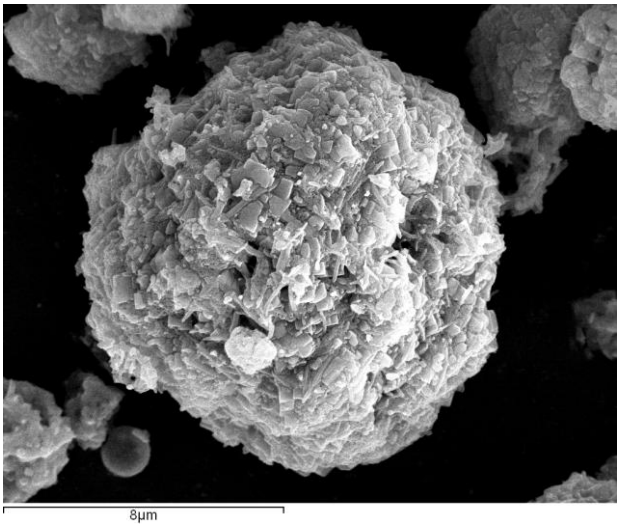

Figure 36. SEM image of sample B05 (72 hours).

The addition of a dispersant to the reactants (sample B05) delays the formation of crystals of MIL-88A. Another possibility is a competitive reaction between sodium citrate and the fumarate chains of MIL-88A.

A curious phenomenon was observed. Samples N02 and B02 and N03 that did not go through the maturation step were submitted to new analysis after several days. Rod-shaped crystals could now be observed in these samples (Figure 37). It is still doubtful if this phase transition occurred naturally, even after the particles are dried, at room-temperature, or if the samples were catalyzed by the electron beam of the SEM, giving enough energy for the phase transition.

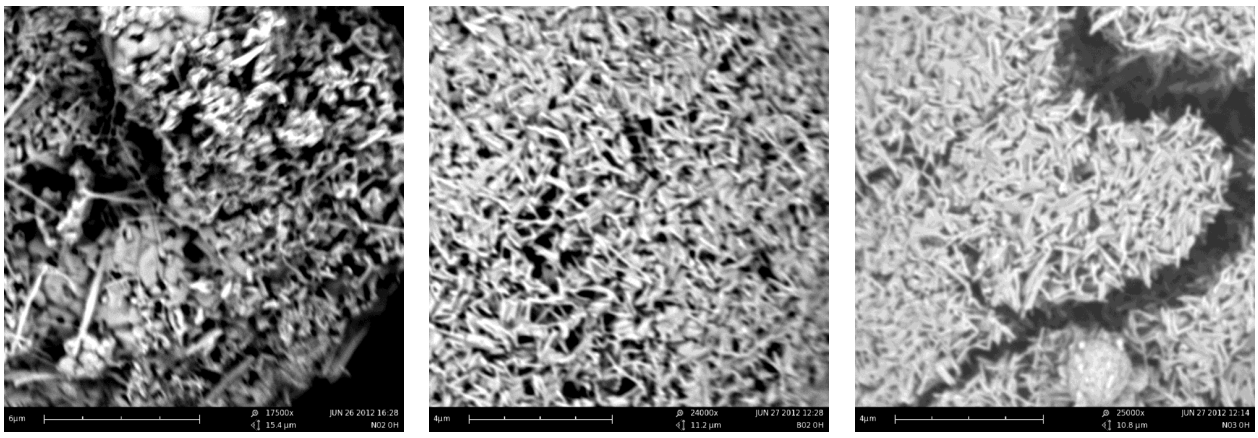

(a) (b) (c)

Figure 37. SEM images of non-mature samples after several days: (a) N02; (b) B02; (c) N03.

Some EDS analysis were performed as well, showing which chemical elements are present in the structure. Figure 38 shows the tested region and Figure 39 the corresponding EDS spectrum.

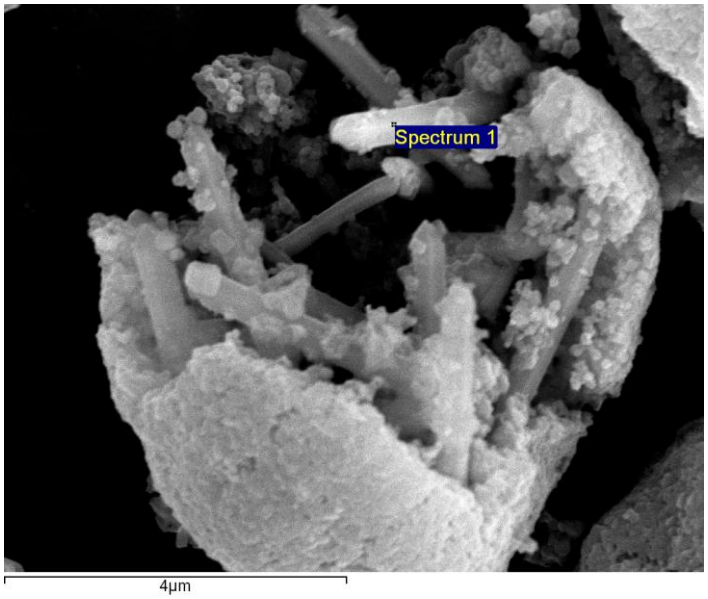

Figure 38. Sample N03 (after 72 hours of maturation) with indication of the tested region.

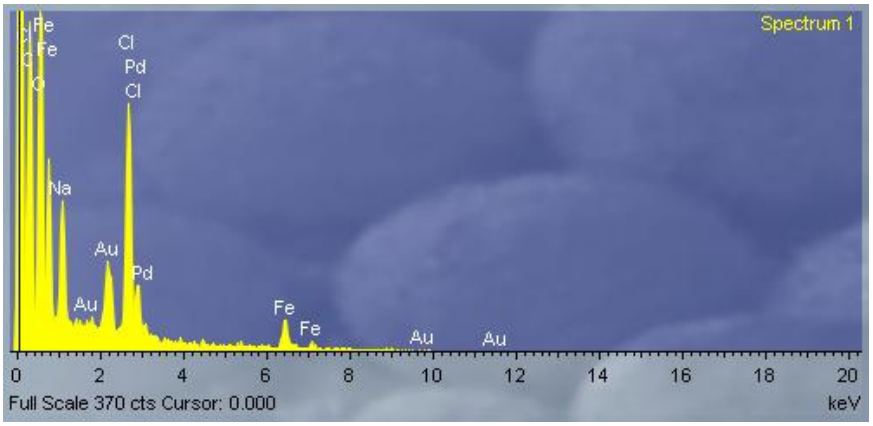

Figure 39. EDS spectrum for the region presented in Figure 38.

The presence of gold in the spectrum is due to the coating of the particles. As expected, there are traces of chlorine, iron, carbon, oxygen and sodium. The presence of sodium cations and chloride anions is due to the formation of sodium chloride crystals.

4.5 XRD Results

XRD spectra are useful to determine if the obtained structures are indeed MIL-88A. This analysis was only made to samples N02 and B02 (both at 0 hours and 72 hours of maturation), and samples B05 (after 72 hours of maturation). The XRD results are presented in Figure 40.

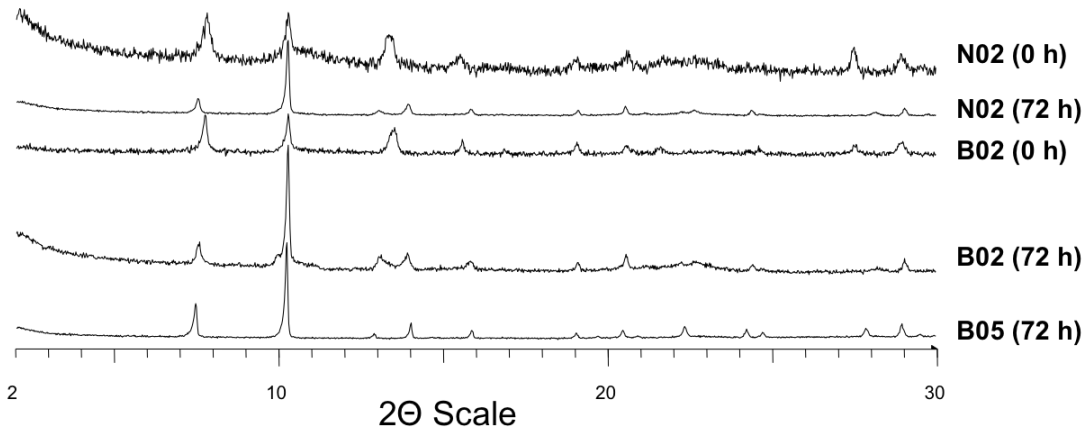

Figure 40. X-Ray diffraction spectra for N02, B02 and B05 samples.

Although some differences can be detected, all the samples show the same peaks. Slightly differences between the samples before and after the maturation step are due to different crystal structures, as observed from SEM. The main difference detected is the existence of two peaks at 2θ = 13-14 if the solution is mature, and the existence of two peaks at 2θ = 28-29 in the N02 and B02 (no maturation). The spectrum of sample B05 is very similar to the spectrum of the other matured samples.

Comparing the XRD spectra of Figure 40 with spectra from the literature (Figure 11 [30]) it is possible to conclude that the obtained structure from these experiments is MIL-88A, therefore the possibility of competitive reaction between citrate and fumarate is ruled out.

4.6 Specific surface area

The specific surface area of metal-organic framework MIL-88A was obtained by the BET method. Different degassing conditions were tested. The nitrogen adsorption isotherms are shown in Figure 41.

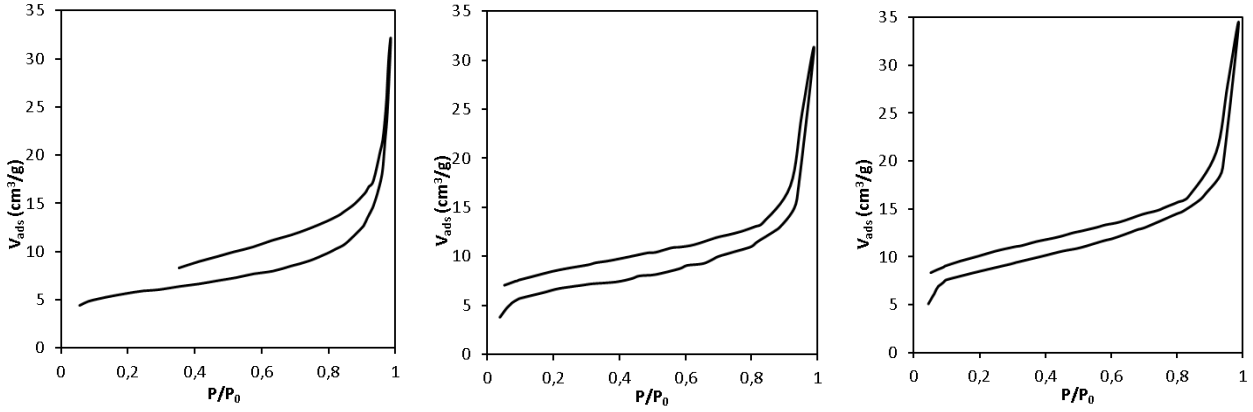

(a) (b) (c)

Figure 41. Adsorption and desorption isotherms of nitrogen for different degassing conditions: (a)) 150 ºC for 3 hours; (b) 100 ºC for 5 hours; (c) 100 ºC for 20 hours.

From Figure 41, hysteresis is observed in the adsorption-desorption isotherm. It is not possible to conclude about the existence or not of micropores in the structure. The hysteresis indicates the existence multilayer adsorption mechanisms that are different from desorption (possible due to the geometry of the mesopores).

The BET surface areas are presented in Table 4.

Table 4. BET surface area of sample N01.

Degassing conditions	S_{BET} (m^2/g)
150 ºC for 3 hours	19.6
100 ºC for 5 hours	23.7
100 ºC for 20 hours	40.8

The results of Table 4 indicate that MIL-88A has poor specific area. In fact, this values needs to be carefully analyzed. The degassing process may shrink the structure of MIL-88A, due to its natural flexibility, preventing nitrogen to penetrate the pores, leading to lower surface areas. Also, the fact that the measured specific surface area depends on the degassing tim indicates that trapped molecules in the framework are being progressively released. However, the obtained values are most likely to represent only the external surface area.

As BET analysis for sample N01 resulted in unexpected, possibly unrealistic results, the other samples were not subjected to these experiments.

4.7 Thermal analysis

To better understand the behavior of the material under high temperature conditions, DSC and TG experiments were performed in sample N01 shown in Figure 42.

DSC and TG are very useful techniques when combined. The material starts to lose mass near 100 ºC, probably due to the removal of water trapped in the framework (adsorbed at the surface). At approximately 280 ºC, the material suffers severe mass loss and a peak on the DSC curve appears. The DSC peaks usually means a phase transition, in this case, an endothermal phase transition. This is probably due to the sublimation of unreacted fumarate (fumaric acid has a sublimation point of 200 ºC [32, 33]). The greatest mass loss occurs at 400 ºC, appearing a peak in the DSC curve. This behavior is probably due to complete collapse of the structure, meaning that this material is not suitable for applications at temperatures above 400 ºC.

In order to evaluate the phase transition that was observed in SEM, extra DSC and TG analysis would be useful. Unfortunately, due to lack of time, it was not possible to perform any more tests.

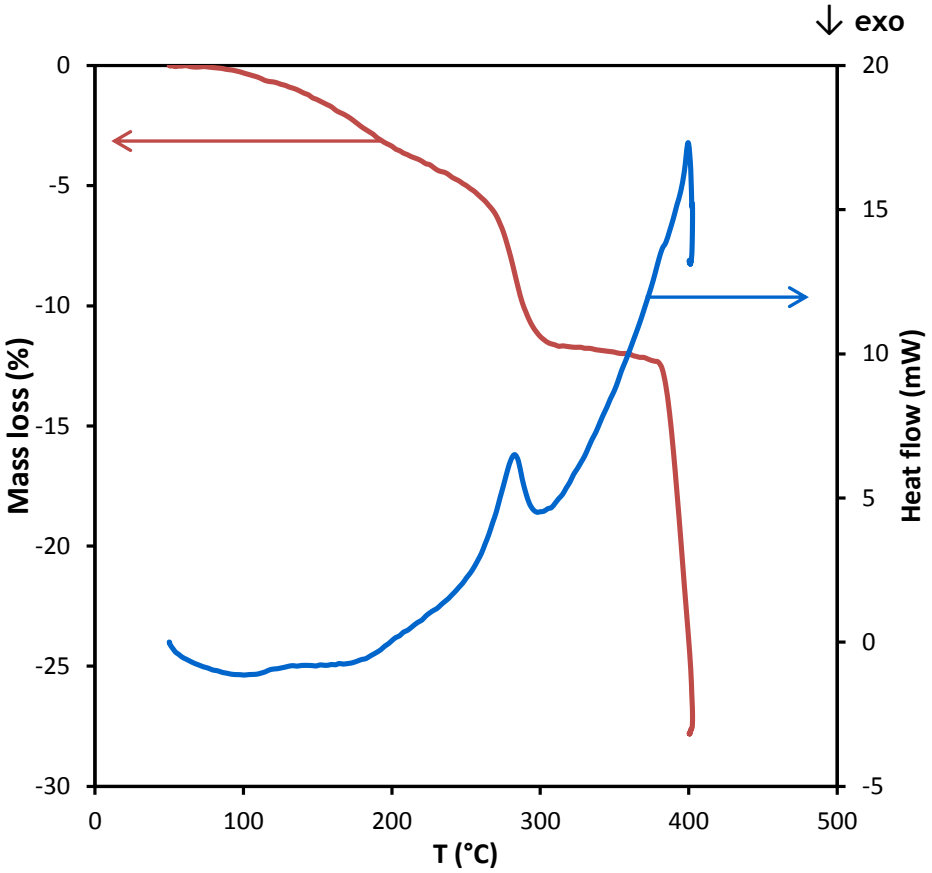

Figure 42. DSC and TG results of sample N01.

4.8 Density

The density is a very important macroscopic property of the material. Porosimetry and the pycnometer method are techniques used to determine, not only the density, but also the porosity of the sample.

Only the samples N02 and B02 (both before maturation and after 72 hours of maturation) were tested. In Table 5 the real and apparent densities, and porosities of each sample are presented.

Table 5. Densities and porosities of MIL-88A.

Sample	ρ_{real} (g/cm^3)	ρ_{ap} (g/cm^3)	ε_{theor}	ε_{exp}
N02 (0 h)	1.90	1.03	0.458	0.416
N02 (72 h)	1.88	0.570	0.697	0.415
B02 (0 h)	1.99	0.906	0.545	0.411
B02 (72 h)	1.93	0.567	0.706	0.455

The density of MIL-88A is close to 1.90 g/cm^3 (higher than the literature value of 1.55 g/cm^3 [9]). It seems that the density is independent of the crystalline structure, as the values are very similar after and before maturation. However, a small difference is detected: the density of the samples after 72 hours of maturation are slightly lower than the density of the samples that did not matured.

It is possible to determine the porosity of the sample, knowing only the real and apparent density, using

$$\varepsilon_p = 1 - \frac{\rho_{\text{ap}}}{\rho_{\text{real}}} \tag{4.2}$$

The results of the theoretical porosity (calculated from equation 4.2) and experimental porosity are presented in Table 5.

The experimental porosities presented in Table 5 were obtained by mercury intrusion in the pores. It is observed that the measured porosity is not very different for the different samples. The theoretical porosities of samples N02 and B02, without maturation, are similar between them, but lower, when compared with the matured samples. It was also observed that sample N02 has lower theoretical porosities than samples B02, which may indicate different material structures.

The difference between the theoretical and experimental results is probably due to the detection range of the equipment. Since mercury is a big molecule, it cannot penetrate the micropores of the material, therefore the equipment only detects the largest pores (mesopores). It is not clear whether the measured porosity concerns the pores of MIL-88A, or the pores of the aggregate structures created in the drying process.

5 Final Remarks

5.1 Conclusions

The main goal of this work was to study the influence of several factors that may affect the production of MIL-88A. In particular, the use of the NETmix® technology to obtain a material with controlled properties under continuous flow production.

It was observed that regarding material properties, NETmix® has a similar performance to batch. The XRD analysis has shown that the obtained product with NETmix® reactor or batch reactor is MIL-88A. However, a few differences were noticed regarding the intensity and position of the peaks that may be due to different crystallite sizes and morphology.

Temperature seems to be an important parameter. Lower temperatures require a maturation step in order to obtain the desired phase. It was observed by SEM imaging, that there are almost no rod-shaped particles when the solution does not mature. On the contrary, at higher temperatures, the desired phase is obtained sooner, but the particles are larger. The maturation is an important process when the experiment is performed at low temperatures.

The addition of a dispersing agent in the solution seems to somehow delay the phase transition. Thus sodium citrate is not the best dispersant for this system.

The typical characterization methods of porous materials were applied. BET analysis presented poor results of surface area. Probably the measured area concerns only the external area of the material. DSC and TG were useful to understand the thermal behavior of MIL-88A.

5.2 Future Work

Future work has to be done in order to better understand the chemistry of MIL-88A. Although this work was useful to improve our knowledge about this type of materials, a lot more has to be done.

NETmix® has been shown to be a reliable technology for production of MIL-88A with characteristic similar to those produced in batch, a promising asset for continuous MOFs production. Further studies on the kinetics of MIL-88 or other MOFs should improve the quality of the final product. The understanding of the phase transition is an important work that may lead to a great evolution in this area. The importance of NETmix® may be greater when higher temperatures are applied, making the crystallization kinetics much faster and making mass transfer an important subject.

The use of other dispersant agents need to be more carefully tested, in order to decrease the rate of aggregation of the particles, and improve the dispersion stability, without retard the phase transition or the reaction kinetics.

5.3 Global Appreciation

The work done throughout this thesis was very rewarding. I had the possibility to work in a very complicated subject that is crystallization of metal-organic frameworks. The knowledge about these processes is not vast, and I am grateful for the opportunity given to try to better understand the physics behind the processes.

Unfortunately, due to lack of time, it was possible to make more experiments and more material characterization that would be useful to know more about MIL-88A.

This is a subject that lays on difficult theories, and the help of all the people that I worked with is appreciated.

This work represents a small step towards the fully comprehension of the mechanisms that control this kind of processes, leading to a new application of the NETmix® reactor.

References

1. Hoskins, B.F. and R. Robson, *Infinite polymeric frameworks consisting of 3 dimensionally linked rod-like segments.* J Am Chem Soc. **111**, 5962-5964,1989
2. Xiao, B. and Q. Yuan, *Nanoporous metal organic framework materials for hydrogen storage.* Particuology. **7**, 129-140,2009
3. Kuppler, R.J., D.J. Timmons, Q.-R. Fang, J.-R. Li, T.A. Makal, M.D. Young, D. Yuan, D. Zhao, W. Zhuang, and H.-C. Zhou, *Potential applications of metal-organic frameworks.* Coordination Chemistry Reviews. **253**, 3042-3066,2009
4. Horcajada, P., R. Gref, T. Baati, P.K. Allan, G. Maurin, P. Couvreur, G. Ferey, R.E. Morris, and C. Serre, *Metal-Organic Frameworks in Biomedicine.* Chem Rev. **112**, 1232-1268,2012
5. Horcajada, P., C. Serre, M. Vallet-Regi, M. Sebban, F. Taulelle, and G. Ferey, *Metal-organic frameworks as efficient materials for drug delivery.* Angew Chem Int Ed Engl. **45**, 5974-5978,2006
6. Rowsell, J.L.C. and O.M. Yaghi, *Metal-organic frameworks: a new class of porous materials.* Microporous and Mesoporous Materials. **73**, 3-14,2004
7. Stock, N. and S. Biswas, *Synthesis of Metal-Organic Frameworks (MOFs): Routes to Various MOF Topologies, Morphologies, and Composites.* Chem Rev. **112**, 933-969,2012
8. Scherb, C., *Controlling the Surface Growth of Metal-Organic Frameworks*, in *Faculty of Chemistry and Pharmacy*, Ludwig-Maximilians-Universität München.2009
9. Serre, C., F. Millange, S. Surble, and G. Ferey, *A route to the synthesis of trivalent transition-metal porous carboxylates with trimeric secondary building units.* Angew Chem Int Ed Engl. **43**, 6285-6289,2004
10. Lopes, J.C.B., P.E.L. Laranjeira, M.M.Q. Dias, and A.A. Martins, *Network Mixer and Related Mixing Process*, in *European Patent EP172643 B1, October 2008*.2008
11. Laranjeira, P.E., A.A. Martins, J.C.B. Lopes, and M.M. Dias, *NETmix®, a new type of static mixer: Modeling, simulation, macromixing, and micromixing characterization.* AIChE Journal. **55**, 2226-2243,2009
12. Laranjeira, P.E., A.A. Martins, M.I. Nunes, J.C.B. Lopes, and M.M. Dias, *NETmix®, a new type of static mixer: Experimental characterization and model validation.* AIChE Journal. **57**, 1020-1032,2011
13. Gomes, P.J., C.M. Fonte, M.M. Dias, and J.C.B. Lopes. *The NETmix® reactor: characterization and quantification of mixing.* in *Chempor 2011- 11th International Chemical and Biological Engineering Conference*. 2011. Almada, Portugal.
14. Silva, V.M.T.M., P.A. Quadros, P.E.M.S.C. Laranjeira, M.M. Dias, and J.C.B. Lopes, *A Novel Continuous Industrial Process for Producing Hydroxyapatite Nanoparticles.* Journal of Dispersion Science and Technology. **29**, 542-547,2008
15. Gomes, P.J., V.M.T.M. Silva, P.A. Quadros, M.M. Dias, and J.C.B. Lopes, *A highly reproducible continuous process for hydroxyapatite nanoparticles synthesis.* Journal of Nanoscience and Nanotechnology. **9**, 3387-3395,2009
16. Mullin, J.W., *Crystallization* 2001: Butterworth-Heinemann.
17. Batten, S.R., N.R. Champness, X.-M. Chen, J. Garcia-Martinez, S. Kitagawa, L. Öhrström, M. O'Keeffe, M.P. Suh, and J. Reedijk, *Coordination polymers, metal-organic frameworks and the need for terminology guidelines.* CrystEngComm.2012

18. Chalati, T., P. Horcajada, R. Gref, P. Couvreur, and C. Serre, *Optimisation of the synthesis of MOF nanoparticles made of flexible porous iron fumarate MIL-88A*. Journal of Materials Chemistry. **21**, 2220-2227,2011

19. Seo, Y.-K., J.W. Yoon, J.S. Lee, U.-H. Lee, Y.K. Hwang, C.-H. Jun, P. Horcajada, C. Serre, and J.-S. Chang, *Large Scale Fluorine-Free Synthesis of Hierarchically Porous Iron(III) Trimes- ate MIL-100(Fe) with a Zeolite MTN Topology*. Microporous and Mesoporous Materials. **in press**,2012

20. Pichon, A., A. Lazuen-Garay, and S.L. James, *Solvent-free synthesis of a microporous metal-organic framework*. CrystEngComm. **8**, 211,2006

21. Bang, J.H. and K.S. Suslick, *Applications of ultrasound to the synthesis of nanostructured materials*. Adv Mater. **22**, 1039-1059,2010

22. Rosi, N.L., J. Eckert, M. Eddaoudi, D.T. Vodak, J. Kim, M. O'Keeffe, and O.M. Yaghi, *Hydrogen storage in microporous metal-organic frameworks*. Science. **300**, 1127-1129,2003

23. Ma, S., D. Sun, M. Ambrogio, J.A. Fillinger, S. Parkin, and H.-C. Zhou, *Framework-Catenation Isomerism in Metal−Organic Frameworks and Its Impact on Hydrogen Uptake*. J Am Chem Soc. **129**, 1858-1859,2007

24. Ma, S., J. Eckert, P.M. Forster, J.W. Yoon, Y.K. Hwang, J.-S. Chang, C.D. Collier, J.B. Parise, and H.-C. Zhou, *Further Investigation of the Effect of Framework Catenation on Hydrogen Uptake in Metal−Organic Frameworks*. J Am Chem Soc. **130**, 15896-15902,2008

25. Ma, S., X.-S. Wang, C.D. Collier, E.S. Manis, and H.-C. Zhou, *Ultramicroporous Metal−Organic Framework Based on 9,10-Anthracenedicarboxylate for Selective Gas Adsorption*. Inorganic Chemistry. **46**, 8499-8501,2007

26. Kalambur, V.S., B. Han, B.E. Hammer, T.W. Shield, and J.C. Bischof, *In vitro characterization of movement, heating and visualization of magnetic nanoparticles for biomedical applications*. Nanotechnology. **16**, 1221-1233,2005

27. Pankhurst, Q.A., J. Connolly, S.K. Jones, and J. Dobson, *Applications of magnetic nanoparticles in biomedicine*. Journal of Physics D: Applied Physics. **36**, R167,2003

28. Surble, S., C. Serre, C. Mellot-Draznieks, F. Millange, and G. Ferey, *A new isoreticular class of metal-organic-frameworks with the MIL-88 topology*. Chem Commun (Camb). 284-286,2006

29. Fateeva, A., P. Horcajada, T. Devic, C. Serre, J. Marrot, J.M. Greneche, M. Morcrette, J.M. Tarascon, G. Maurin, and G. Ferey, *Synthesis, Structure, Characterization, and Redox Properties of the Porous MIL-68(Fe) Solid*. European Journal of Inorganic Chemistry. 3789-3794,2010

30. Mellot-Draznieks, C., C. Serre, S. Surblé, N. Audebrand, and G. Férey, *Very Large Swelling in Hybrid Frameworks: A Combined Computational and Powder Diffraction Study*. J Am Chem Soc. **127**, 16273-16278,2005

31. Serre, C., C. Mellot-Draznieks, S. Surble, N. Audebrand, Y. Filinchuk, and G. Ferey, *Role of solvent-host interactions that lead to very large swelling of hybrid frameworks*. Science. **315**, 1828-1831,2007

32. Wikipedia. *Wikipedia, the free encyclopedia*. 2012 [cited 2012; Available from: http://en.wikipedia.org/.

33. Polyanskiy, M. *Refractive Index Database*. 2008 [cited 2012; Available from: http://refractiveindex.info/.

34. Instruments, M., *Zetasizer Nano Series User Manual* 2009.

Appendix A. Rheology experiments' results

As introduced in section 3, rheology experiments were necessary to evaluate the mixture rheological properties. This necessity was clear when the viscosity increase was observed in the NETmix® reactor, leading to segregation or blockage of the flow in the chambers, meaning that the mixture quality was poor.

The rheology experiments were performed for 3 different concentrations (0.4 M, 0.16 M and 0.08 M) and 4 different shear rates (365.5 s^{-1}, 713 s^{-1}, 1426 s^{-1} and 2852 s^{-1}). The shear rate in the NETmix® reactor for Reynolds number = 600 is 2140 s^{-1}, considering water properties. The tested shear rates are 6, 3, 1.5 times lower and 4/3 times higher than the shear rate for water. Each experiment was performed in triplicate, and the presented results are the average of these three tests.

As can be observed in Figure A-1 to Figure A-3, the viscosity behaved in the same way for each experiment: in the beginning the viscosity increases and after a while it decreases to what appear to be a stationary state.

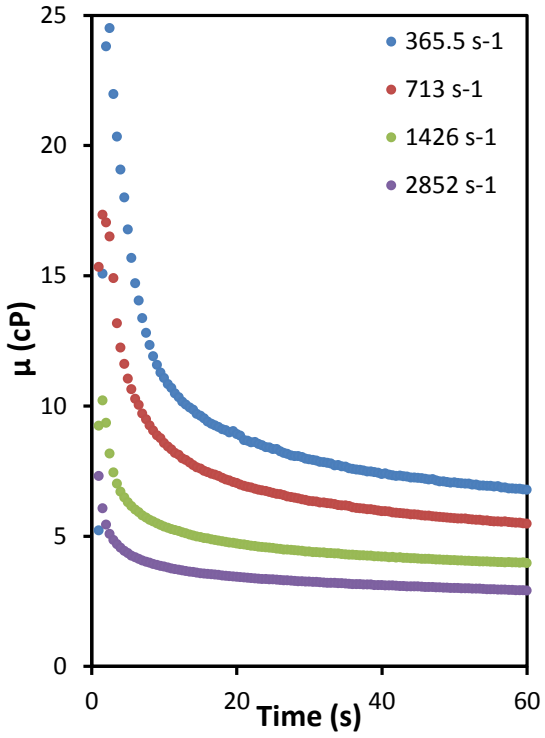

Figure A-1. Reaction mixture viscosity as a function of time for different shear rates (for reactants concentration = 0.4 M).

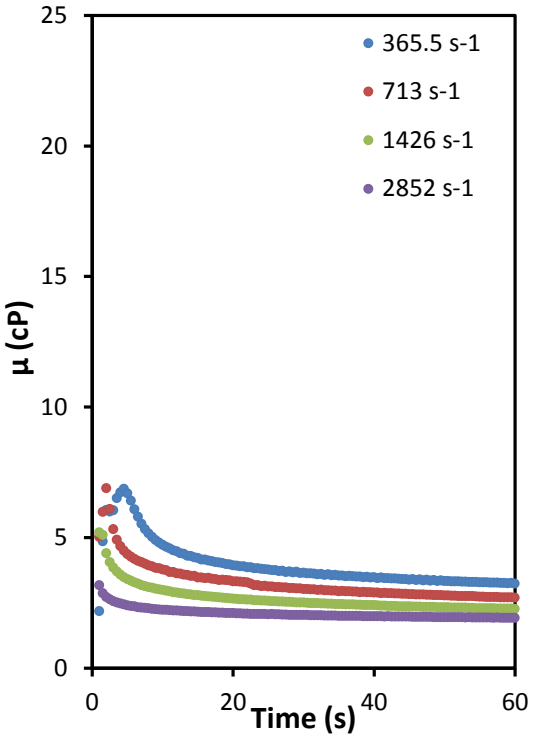

Figure A-2. Reaction mixture viscosity as a function of time for different shear rates (for reactants concentration = 0.16 M).

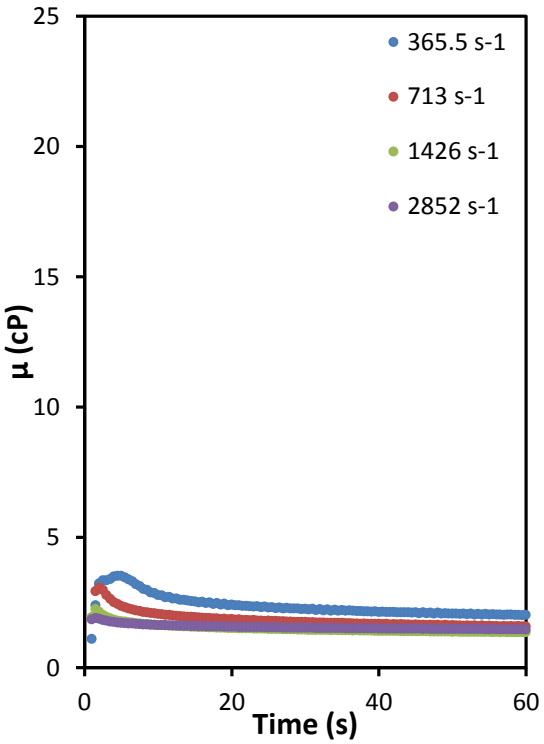

Figure A-3. Reaction mixture viscosity as a function of time for different shear rates (for reactants concentration = 0.08 M).

The fact that the behavior is different for different shear rates indicates an influence of the mixing quality. Indeed, when the mixture is slower (low shear rates) the viscosity is higher.

Mainly because the process is controlled by the crystallization kinetics and mixing, leading to slower kinetics (if compared with a process controlled only by the reaction kinetics).

If reactants concentration is higher, the viscosity is also higher. This is easily understandable, due to the presence of solid particles that represent an extra resistance to the flow. Higher concentration of solids in the mixture (due to the higher concentration of reactants) leads to higher viscosity.

The fact that the viscosity increases at the beginning could be due to the nucleation phase that is prevalent in that region.

The effect of crystallization on the viscosity is almost negligible for very dilute solutions (reactants concentration under 0.08 M).

As observed in Figure A-4, the maximum value of the viscosity increases with the reactants concentration (almost linearly) and decreases with the shear rate.

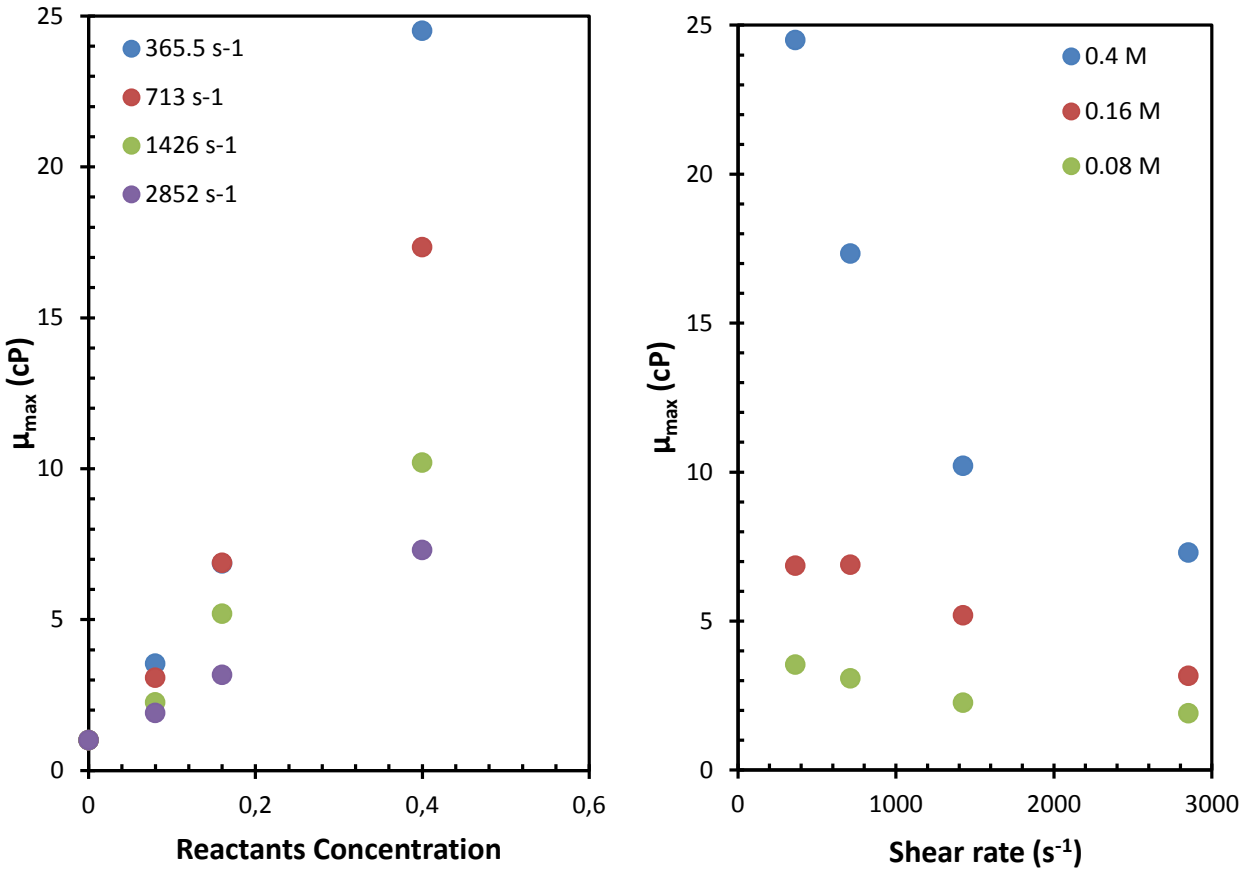

Figure A-4. Maximum viscosity as a function of: (a) reactants concentration; (b) shear rate.

The addition of dispersants such as sodium citrate and PVP (polyvnylpyrrolidone) was tested by rheological experiments. The results are presented in Figure A-5.

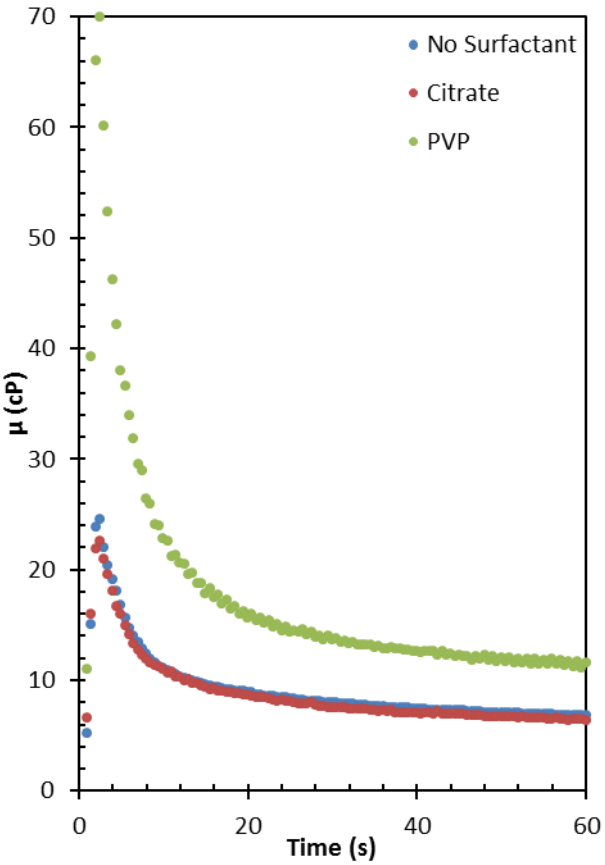

Figure A-5. Influence of the dispersant in the viscosity increase (shear rate = 356.5 s^{-1}).

The viscosity is almost 70 times bigger than water when PVP is used as a dispersant. This may be due to the fact that PVP is a macromolecule that may be tangled. The use of PVP was immediately withdrawn after these results. Using citrate does not affect significantly the rheological properties.

Appendix B. SEM images

In this section, the complete set of SEM images is presented.

Sample N01

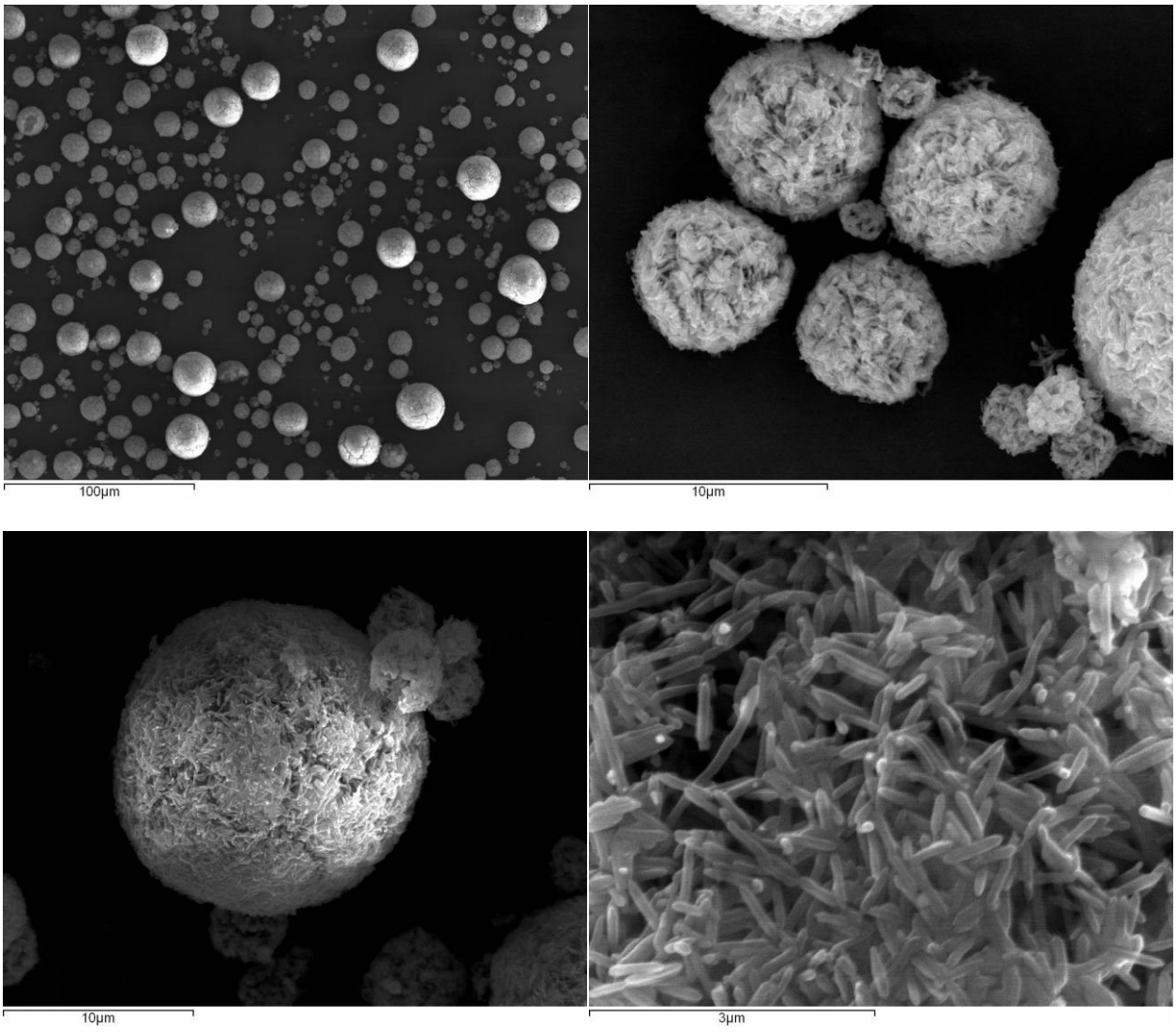

Figure B-1. SEM images of sample N01, at different scales.

Sample N02 (0 hours of maturation)

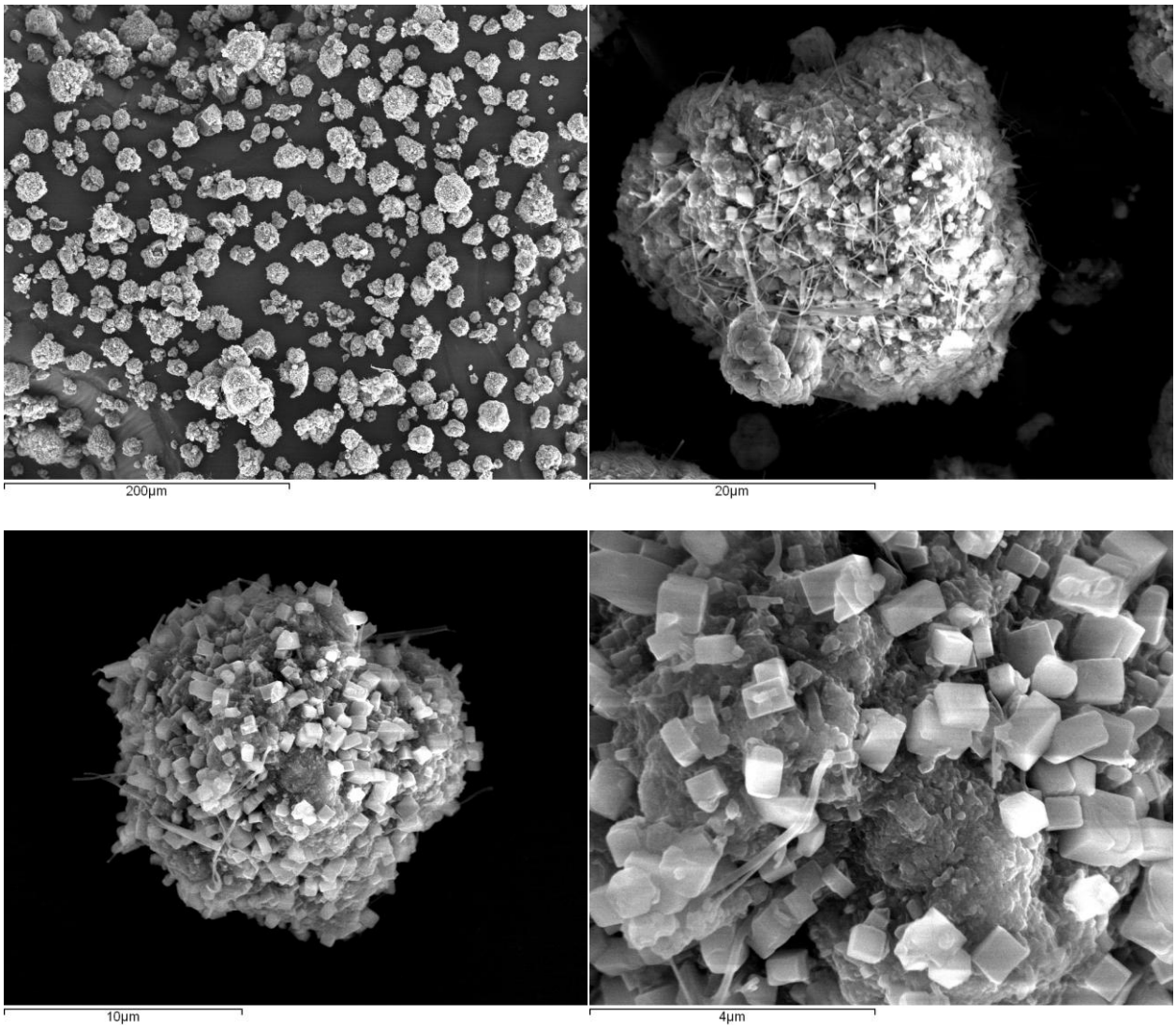

Figure B-2. SEM images of sample N02, no maturation, at different scales.

Sample N02 (0 hours of maturation), after several days (crystallization detected)

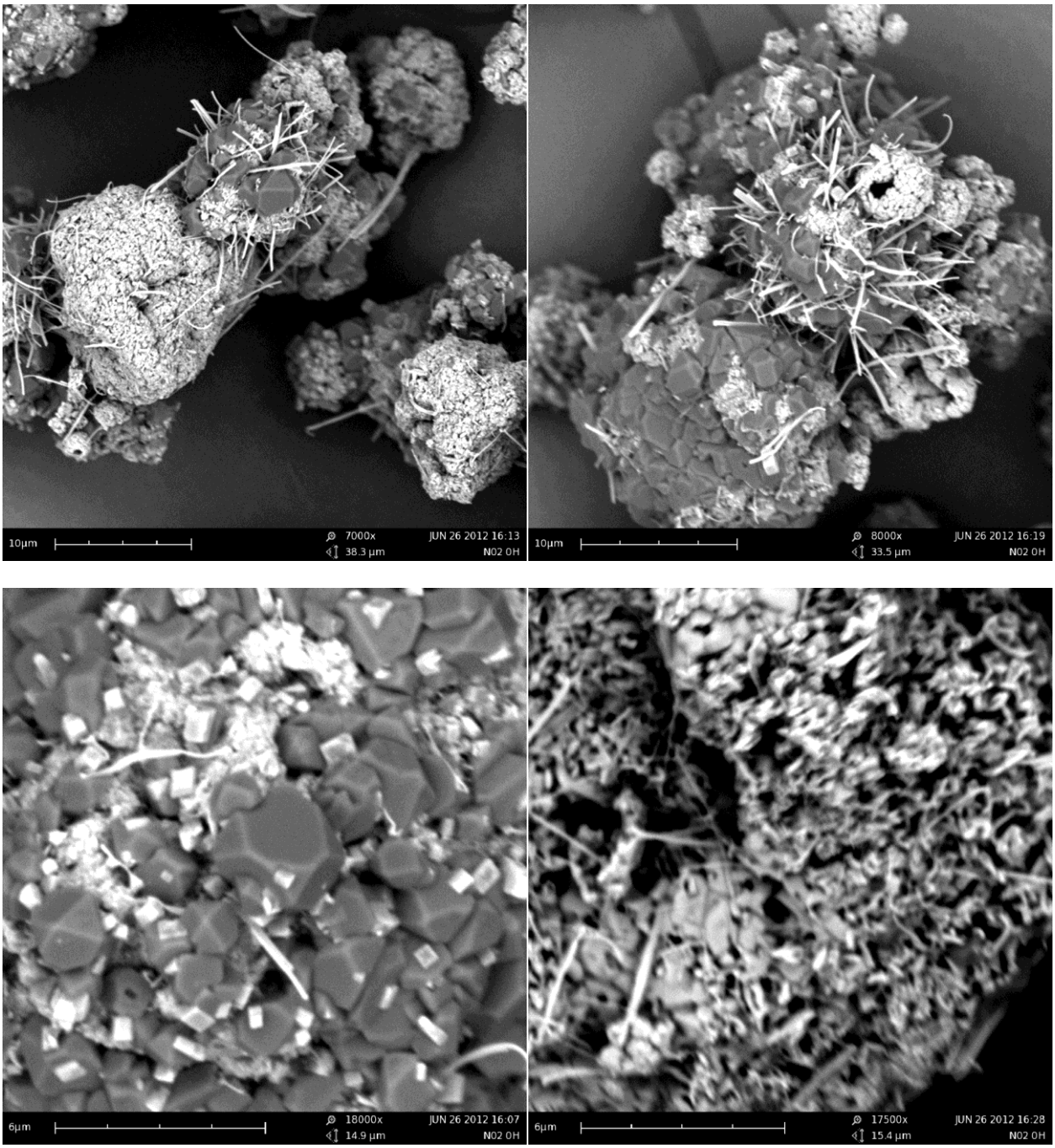

Figure B-3. SEM images of sample N02, no maturation, after several days, at different scales.

Sample N02 (72 hours of maturation)

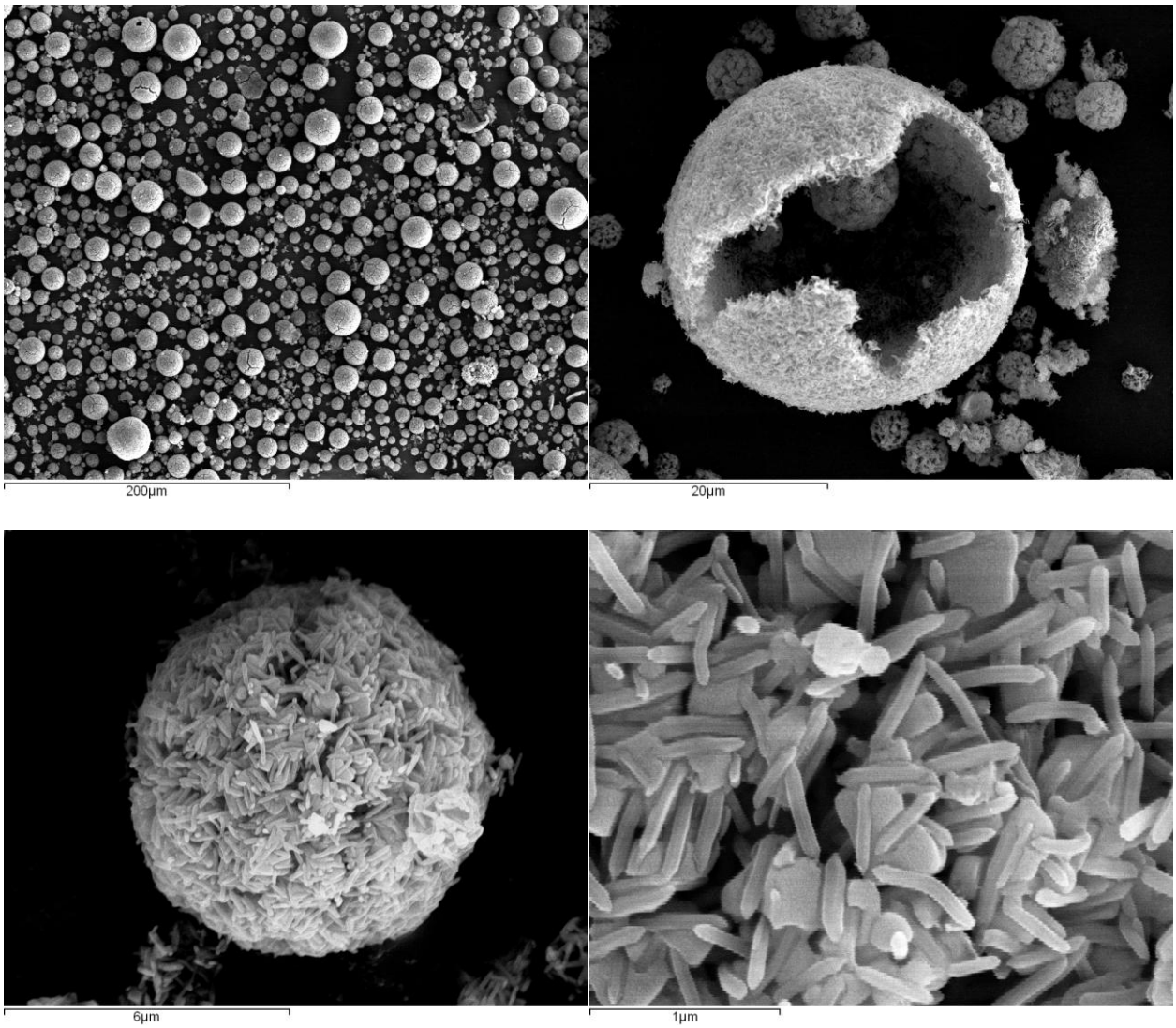

Figure B-4. SEM images of sample N02, after 72 hours of maturation, at different scales.

Sample B02 (0 hours of maturation)

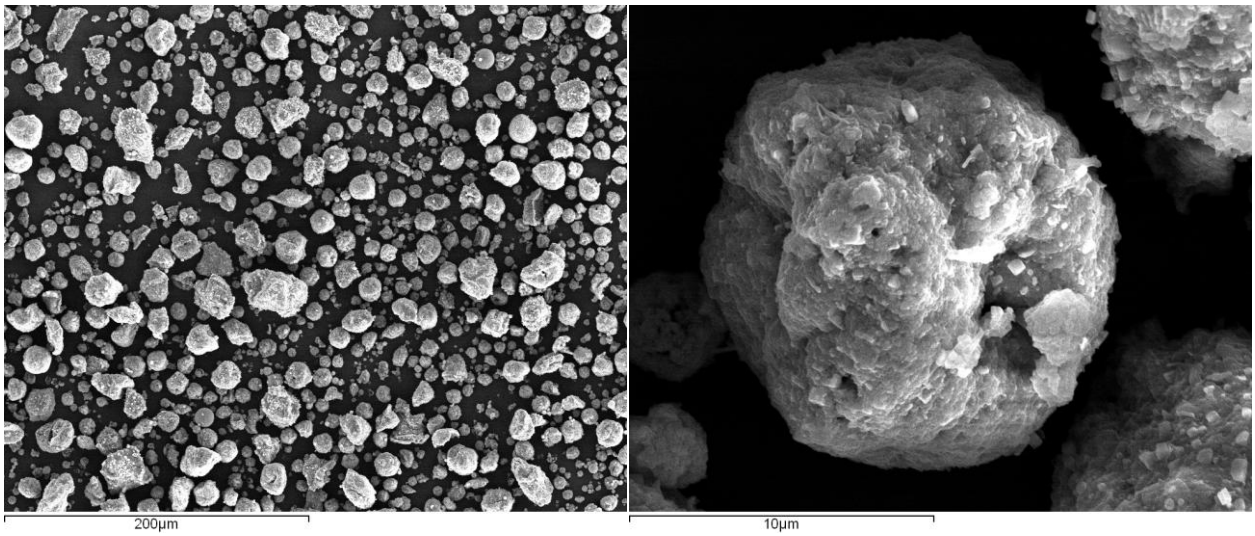

Figure B-5. SEM images of sample B02, no maturation, at different scales.

Sample B02 (0 hours of maturation), after several days (crystallization detected)

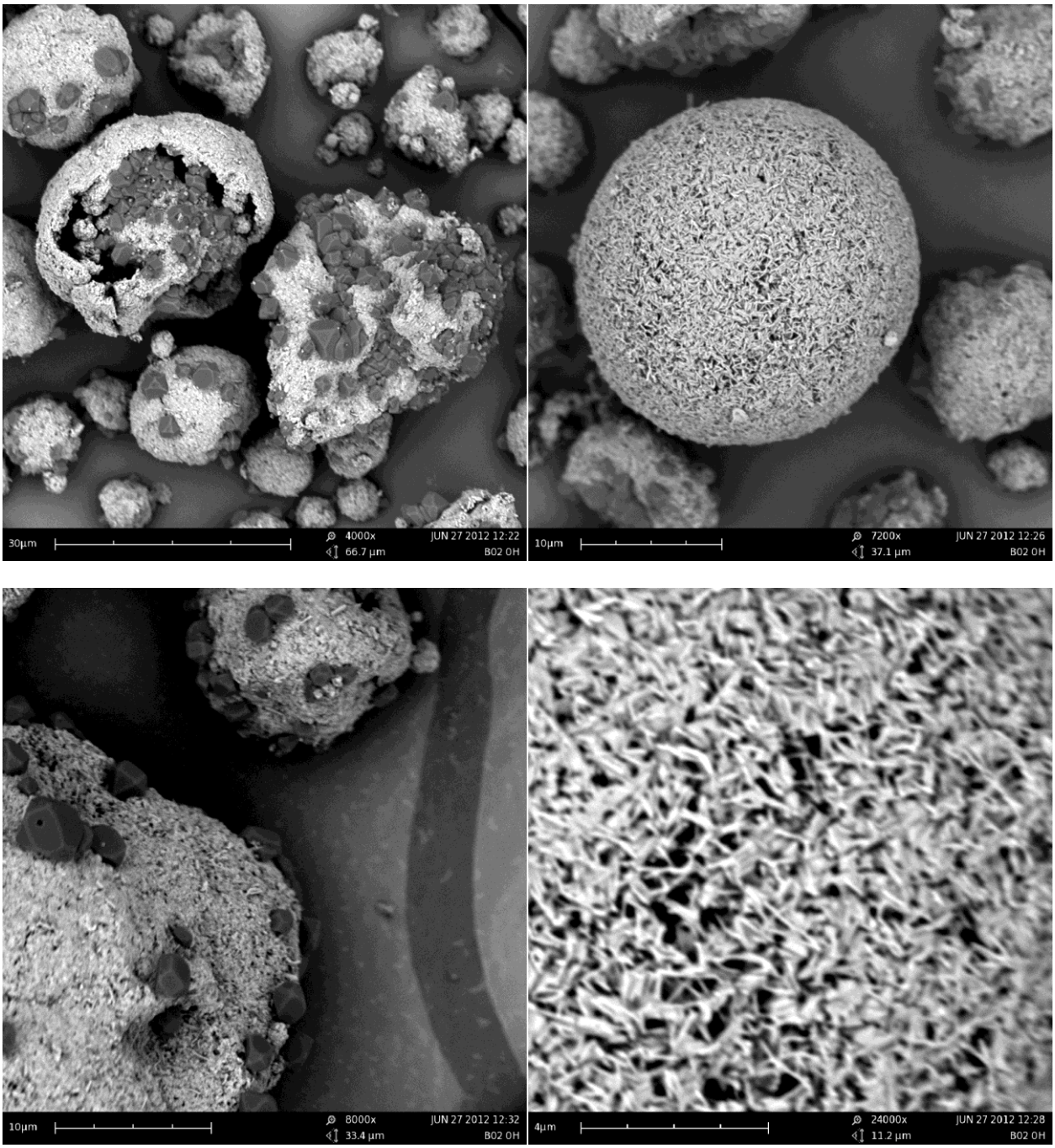

Figure B-6. SEM images of sample B02, no maturation, after several days, at different scales.

Sample B02 (72 hours of maturation)

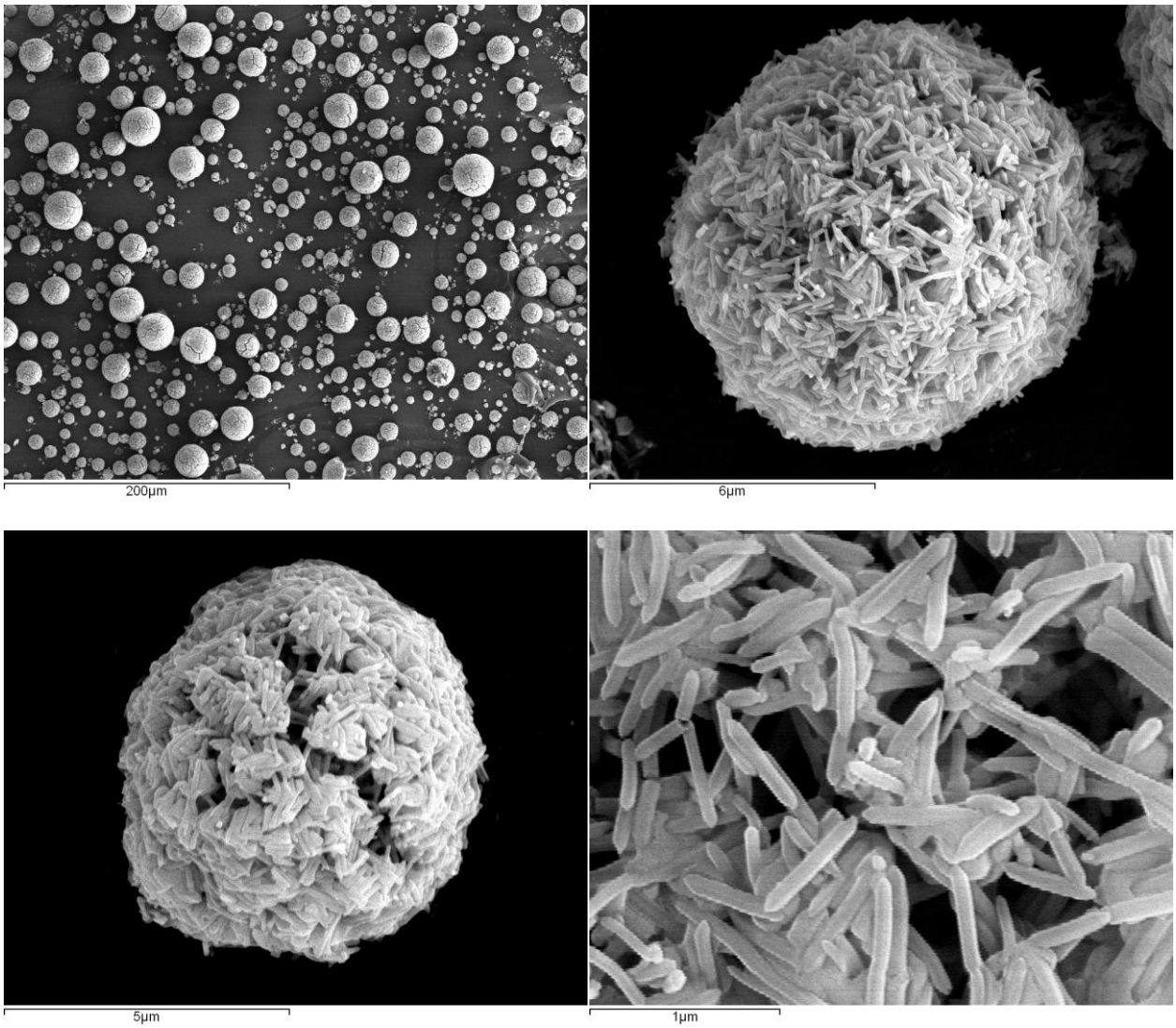

Figure B-7. SEM images of sample B02, after 72 hours of maturation, at different scales.

Sample N03 (0 hours of maturation)

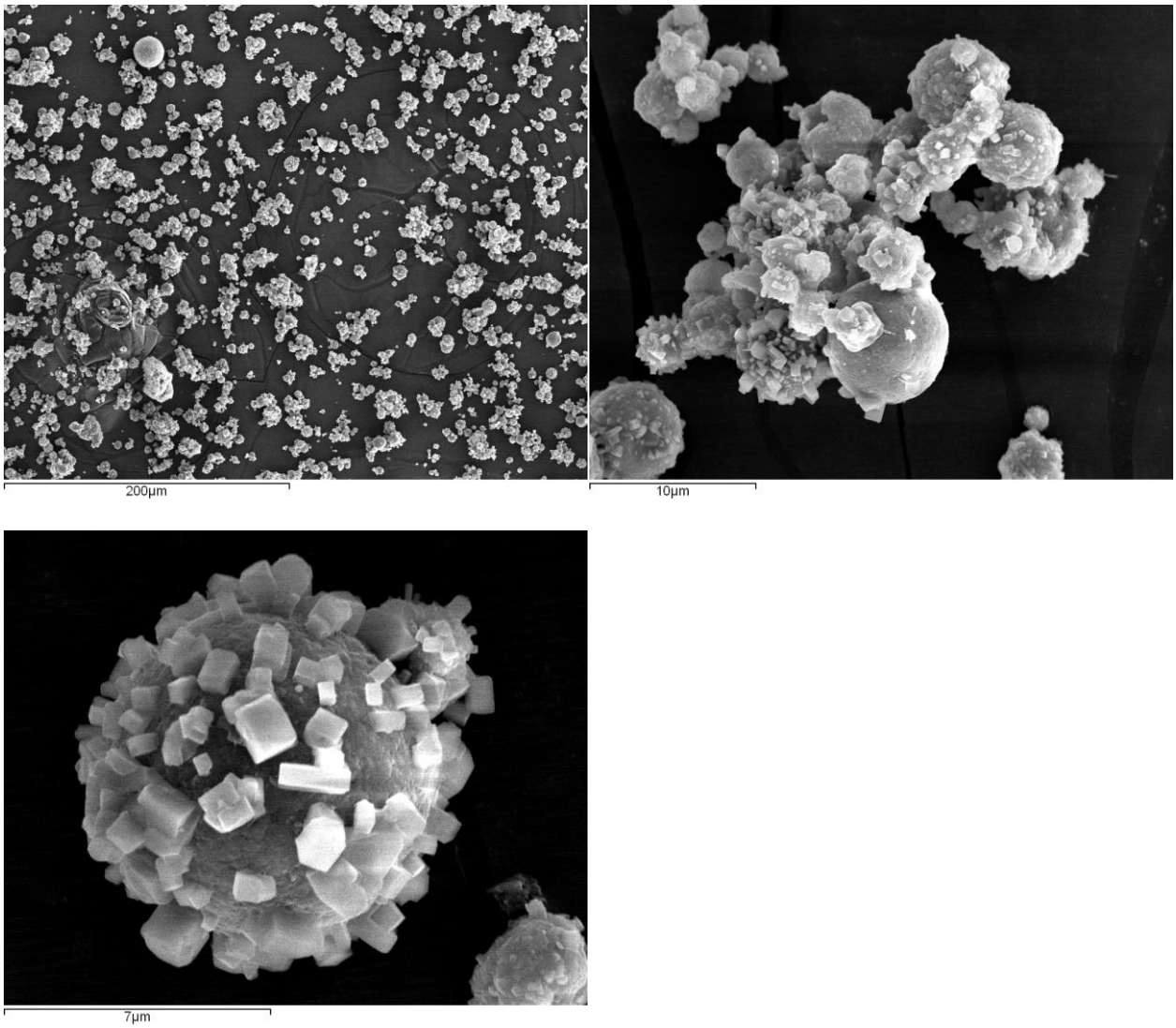

Figure B-8. SEM images of sample N03, no maturation, at different scales.

Sample N03 (0 hours of maturation), after several days (crystallization detected)

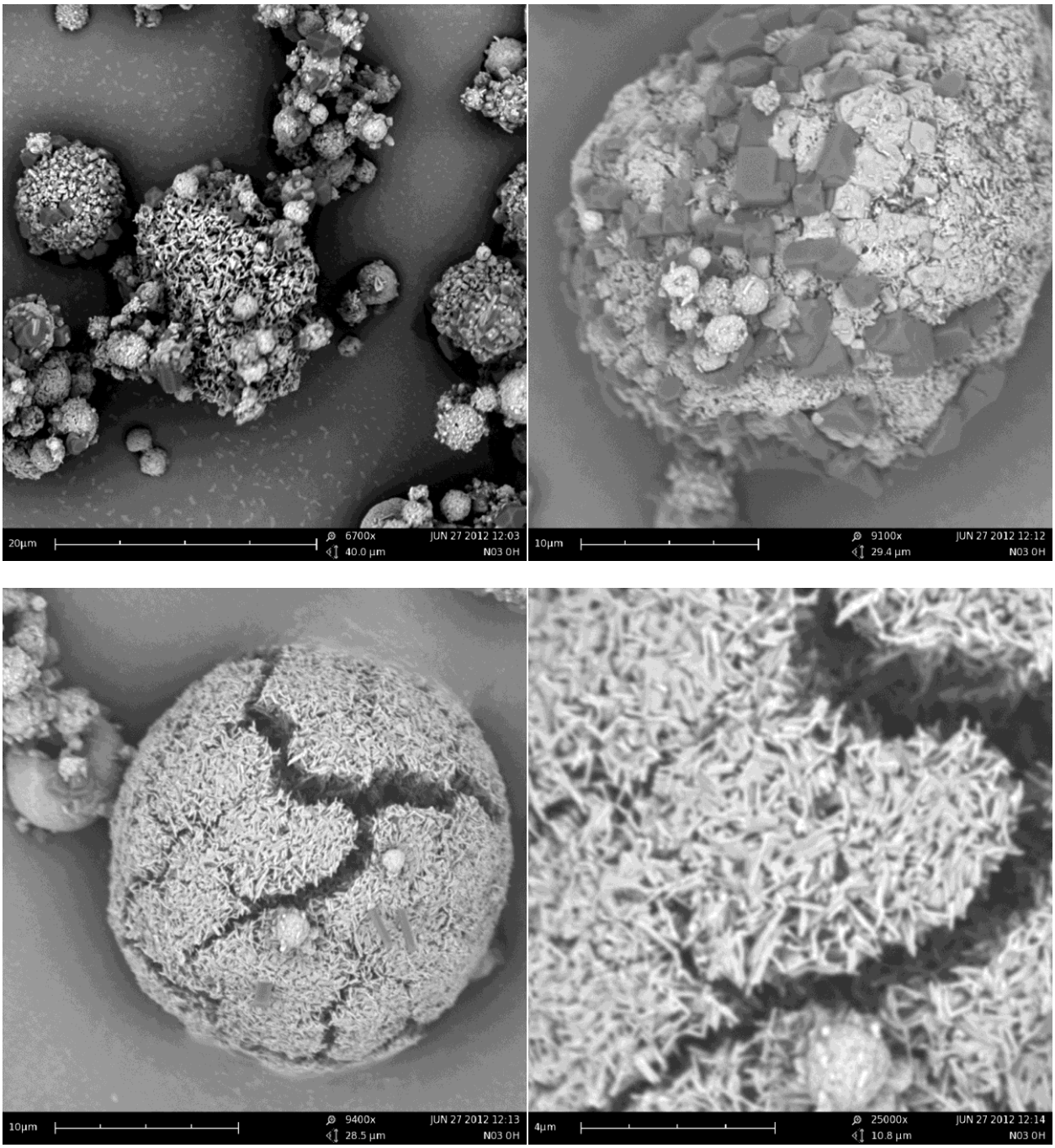

Figure B-9. SEM images of sample N03, no maturation, after several days, at different scales.

Sample N03 (72 hours of maturation)

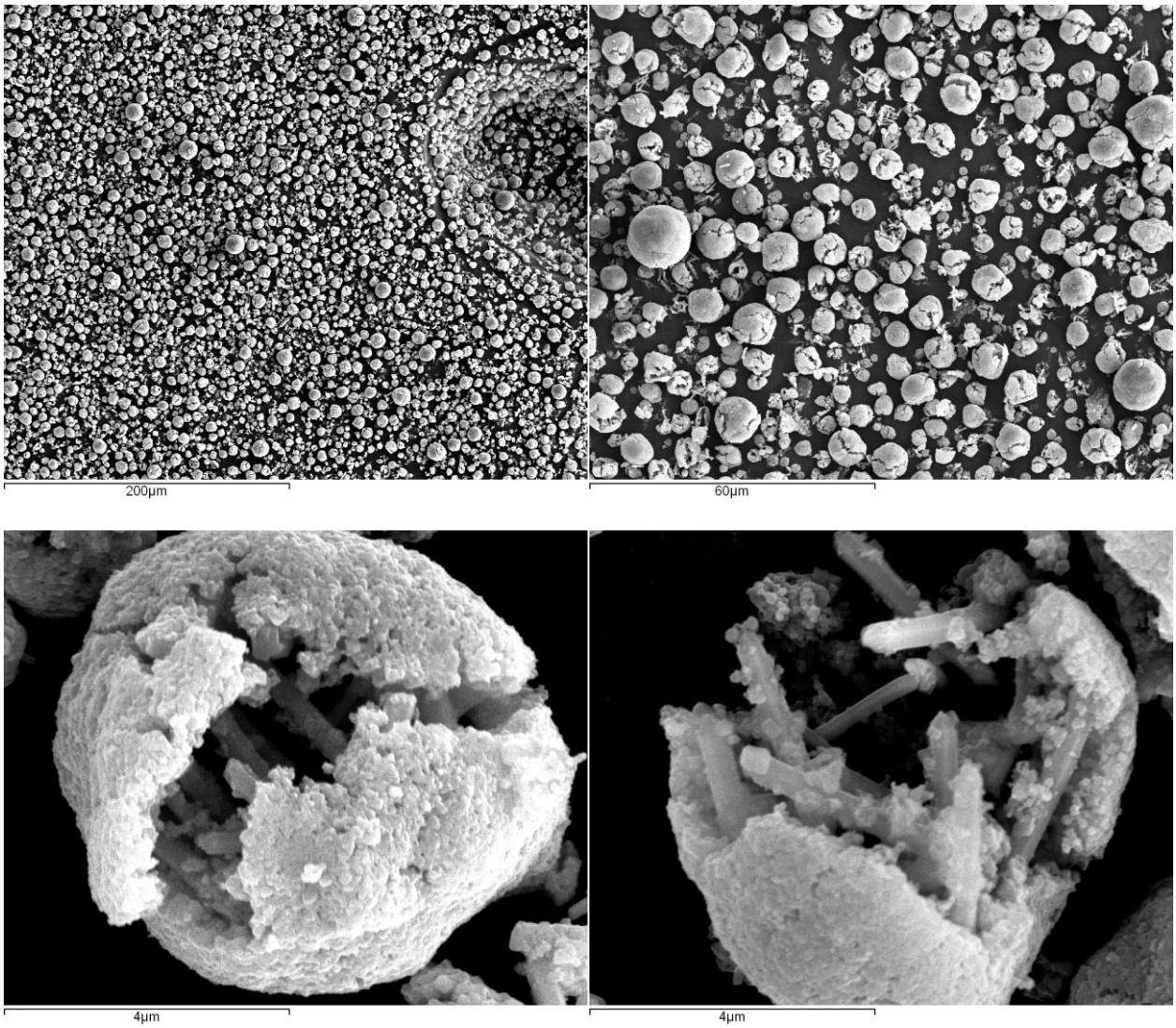

Figure B-10. SEM images of sample N03, after 72 hours of maturation, at different scales.

Sample N04 (0 hours of maturation)

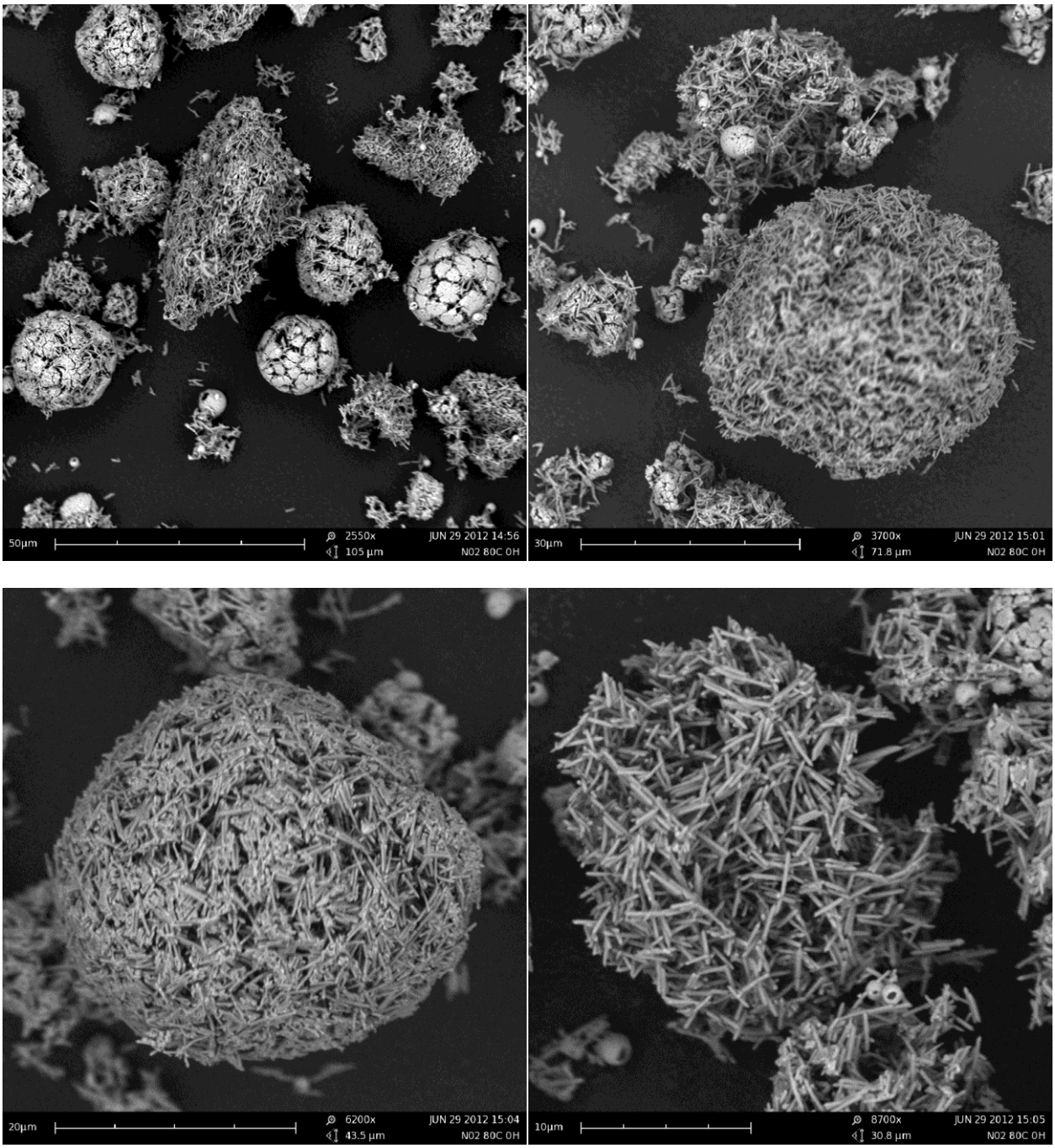

Figure B-11. SEM images of sample N04, no maturation, at different scales.

Sample B04 (0 hours of maturation)

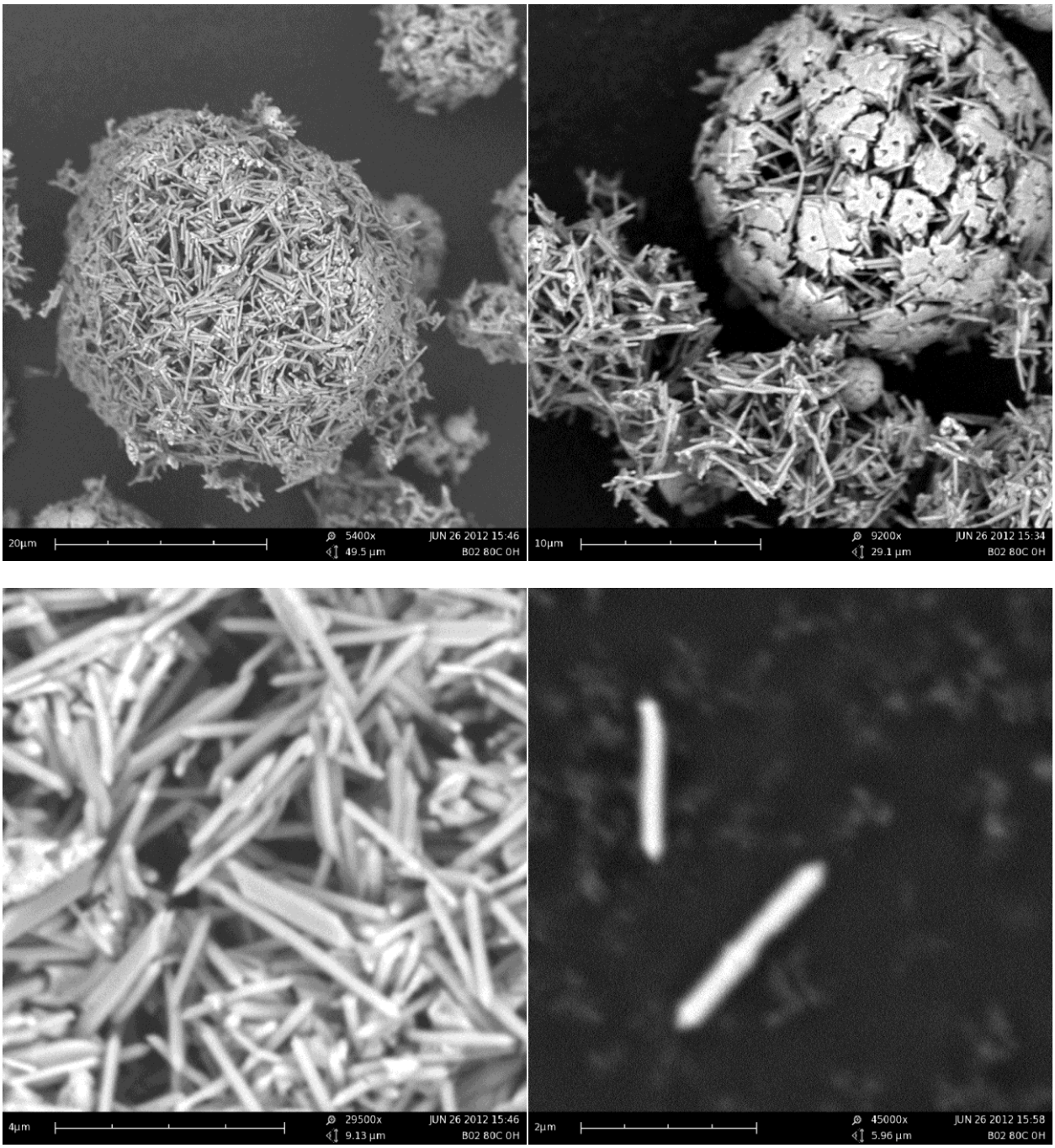

Figure B-12. SEM images of sample B04, no maturation, at different scales.

Sample B05 (72 hours of maturation)

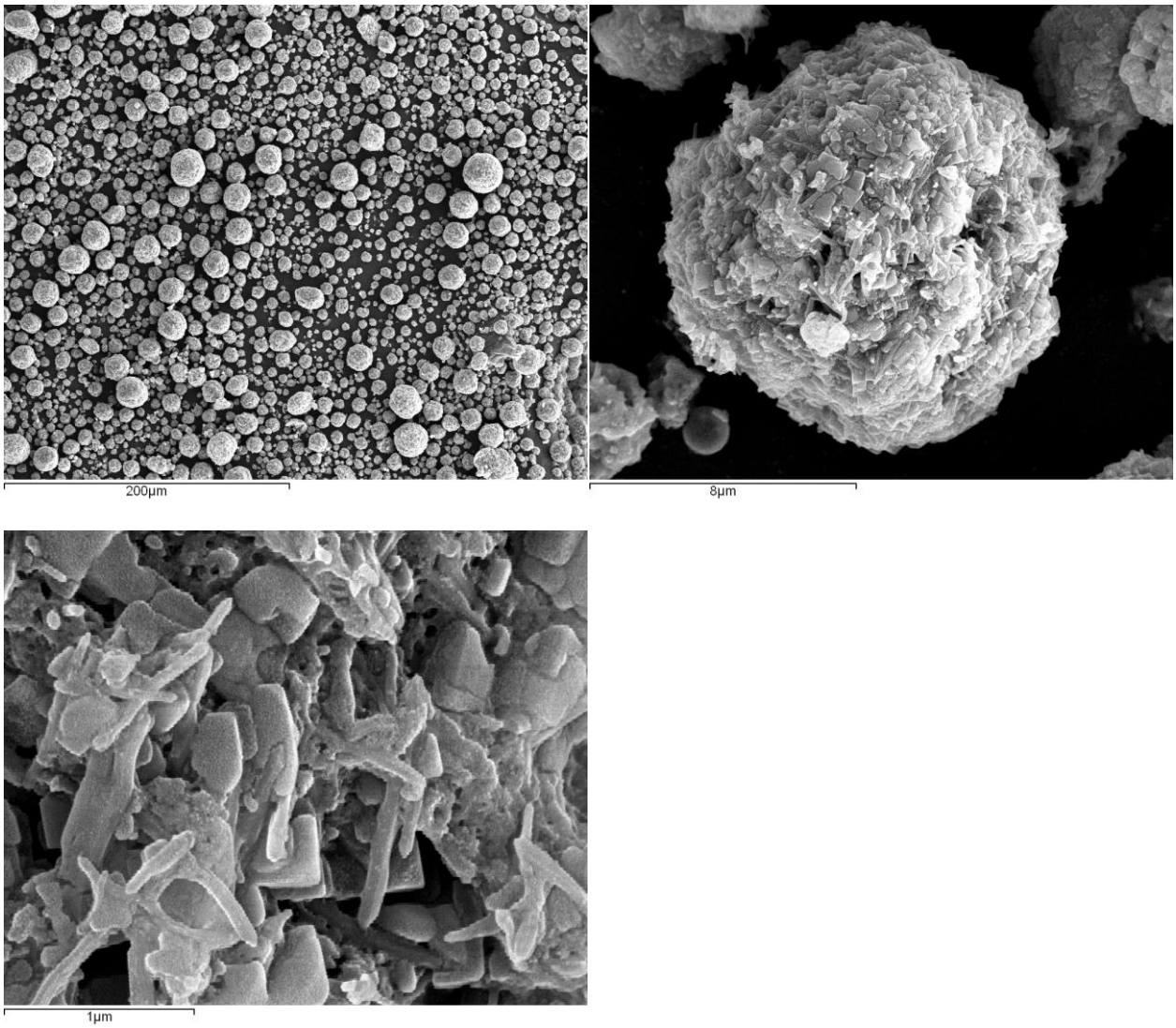

Figure B-13. SEM images of sample B05, no maturation, at different scales.

Appendix C. Shear rate and geometrical dimensions of the NETmix® reactor

In order to evaluate the increase of the viscosity in the reaction mixture, it is necessary to estimate the shear rate in the channels walls of the NETmix® reactor. But first of all, it is necessary to know the geometrical dimensions of the reactor (presented on Table C-1).

Table C-1. Geometrical dimensions of the NETmix® reactor (see Figure 15b).

N_{rows}	29
$N_{columns}$	8
D (mm)	6.5
d (mm)	1.5
ω (mm)	3
$V_{reactor}$ (mL)	23

The shear rate can be calculated assuming that the velocity profile in the channels is parabolic (Figure C-1).

Therefore the velocity profile is given by

$$\upsilon_x(y) = -\upsilon_{\max}\left[1-\left(\frac{y}{d/2}\right)^2\right] \tag{C.1}$$

Where υ_x is the velocity in position y (m/s), $\upsilon_{\max}$ is the maximum velocity of the fluid (m/s), y is the position coordinate, being zero at the center of the channels (m) and d is the width of the channel (m).

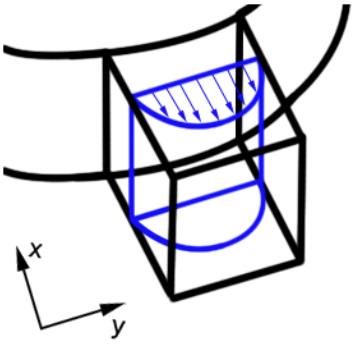

Figure C-1. Parabolic velocity profile in a NETmix® channel.

The shear rate in the channels walls is given by

$$\dot{\gamma}_{walls} = \left. \frac{d\upsilon_x}{dy} \right|_{y=d/2} \tag{C.2}$$

The maximum velocity can be calculated as a function of the mean velocity, using the mean value theorem.

$$\bar{\upsilon} = \frac{Q}{A} = \frac{\int_{-d/2}^{d/2} \upsilon_x dy}{d} = \frac{2}{3}\upsilon_{\max} \tag{C.3}$$

Where Q is the flowrate in the channel (m^3/s) and A is the is the area of the face of the channel normal to the direction of the flow (m^2).

Using the equations C.1 to C.3, it is possible to calculate de shear rate in the NETmix® channels as a function of the mean velocity.

$$\dot{\gamma}_{walls} = \frac{6\bar{\upsilon}}{d} \tag{C.4}$$

Appendix D. Nanoparticles mean free path

Producing nanoparticles requires some special cares. Formation of clusters of particles is undesirable. The objective is to produce particles as less aggregated as possible. Therefore, it is crucial to develop a model to predict the theoretical distance between nanoparticles as function of the solids concentration (and nanoparticle geometrical information).

Obviously, the model has some assumptions that simplify it. It is assumed that the nanoparticles are rod-shaped particles (with a prismatic shape), and can be represented as a parallelepiped (Figure D-1). This assumption is reasonable considering the images obtained by SEM.

The molar concentration of MOF nanoparticles in solution, C_{MOF}, is given by

$$C_{MOF} = \frac{n_{MOF}}{V_{sol}} = \frac{m_{MOF}}{M_{MOF} V_{sol}} \tag{D.1}$$

where C_{MOF} is the concentration of MOF (mol/L), n_{MOF} is the number of moles of MOF (mol), V_{sol} is the total volume of the solution (L), m_{MOF} is the mass of MOF (g) and M_{MOF} is the molecular weight of MOF (g/mol).

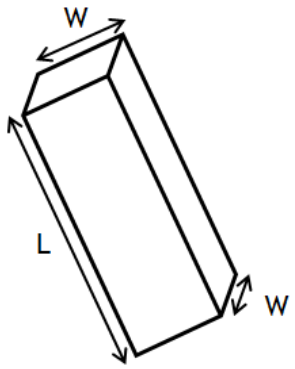

Figure D-1. Nanoparticles geometry.

One can assume that the total volume of the solution is constrained in a cubic-shaped manner (Figure D-2).

Thus, the volume of the solution is given by

$$V_{sol} = I^3 \tag{D.2}$$

Where I is the edges length (m).

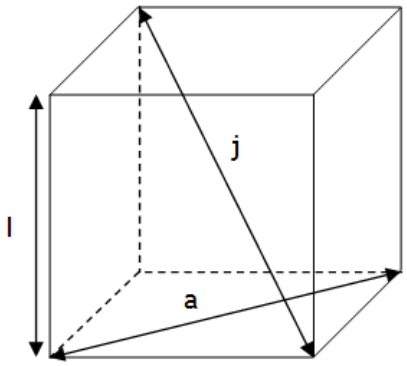

Figure D-2. Volume of the solution with nanoparticles.

The distance j is

$$j^2 = a^2 + I^2 \Rightarrow j = \sqrt{3}I \tag{D.3}$$

Where j and a are the diagonal length of the cube (m).

Assuming a uniform distribution of the nanoparticles within the control volume, the number of nanoparticles in the j direction is

$$n = \sqrt{3}\left(N_{\text{np}}\right)^{1/3} \tag{D.4}$$

Where n is the number of nanoparticles in the j direction and N_{np} is the number of nanoparticles in solution.

The number of nanoparticles in solution may be estimated using the following equation

$$N_{\text{np}} = \frac{V_{\text{MOF}}}{V_{\text{np}}} = \frac{m_{\text{MOF}}}{\rho_{\text{MOF}} W^2 L} \tag{D.5}$$

where V_{MOF} is the volume of MOF in solution (L), V_{np} is the volume of a single rod-shaped MOF nanoparticle (L), ρ_{MOF} is the density of the MOF (g/L), L is the nanoparticles length (m) and W is the nanoparticles width.

Therefore, the distance of the nanoparticles in the j direction is given by

$$\Delta x = \frac{j - nL}{n} \tag{D.6}$$

Where Δx is the distance between nanoparticles in the j direction (m).

Combining the previous equations, it is possible to estimate the distance between nanoparticles, assuming that the particles have a prismatic shape and are uniformly distributed in the volume of the solution.

$$\frac{\Delta x}{L} = \left(\frac{\rho_{MOF}}{M_{MOF} C_{MOF}} \right)^{1/3} \left(\frac{W}{L} \right)^{2/3} - 1 \qquad \text{(D.7)}$$

Appendix E. Amount of dispersant

The objective of one of the performed experiments is to study the effect of a dispersant in the process of producing MOFs. Therefore, it is necessary to develop a model that can predict the necessary amount of needed dispersant.

The theoretical amount of dispersant to be adsorbed in the nanoparticles surface can be estimated using some simple concepts. The number of nanoparticles in solution N_{np} is calculated from equation D.5.

Let's consider a dispersant molecule with a spherical shape with diameter D_{disp}. It is possible to calculate the number of minimum molecules of dispersant per particle of MOF by simply using some geometric relations, considering that is only necessary to cover the particle in a monolayer. Considering a prismatic nanoparticle, divided in square of area D_{disp}^2 (the edge has the same length as the dispersant diameter), one can calculate the amount of dispersant needed to isolate each particle (Figure E-1).

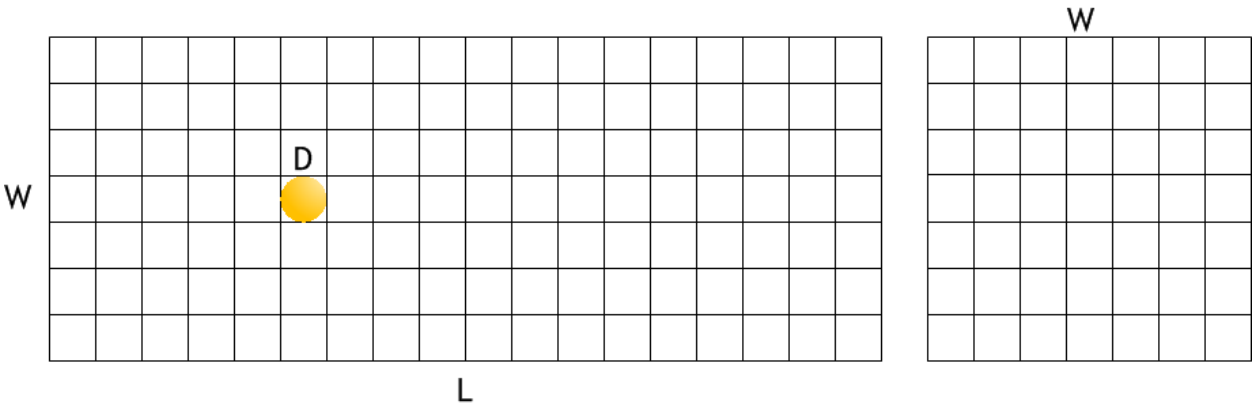

Figure E-1. Number of dispersant molecules adsorbed (monolayer) in a nanoparticle.

The total number of squares is the total amount of dispersant needed to be adsorbed in a nanoparticle.

$$N_{\text{disp/np}} = \frac{W}{D_{\text{disp}}}\frac{L}{D_{\text{disp}}} + \left(\frac{W}{D_{\text{disp}}}\right)^2 \qquad \text{(E.1)}$$

Where $N_{\text{disp/np}}$ is the number of dispersant molecules per nanoparticle.

The amount of dispersant needed is obtained by using equation E.2.

$$n_{\text{disp}} = N_{\text{disp/np}} \frac{m_{\text{MOF}}}{\rho_{\text{MOF}} W^2 L N_A} = N_{\text{disp/np}} \frac{C_{\text{MOF}} V_{sol}}{\rho_{\text{MOF}} M_{\text{MOF}} W^2 L N_A} \quad \text{(E.2)}$$